

# **Mantle upwelling at Afar triple junction shaped by overriding plate dynamics**

Emma J. Watts<sup>1,2\*</sup>, Rhiannon Rees<sup>1</sup>, Philip Jonathan<sup>3,4</sup>, Derek Keir<sup>1,5</sup>, Rex N. Taylor<sup>1</sup>, Melanie Siegburg<sup>6</sup>, Emma L. Chambers<sup>7</sup>, Carolina Pagli<sup>8</sup>, Matthew J. Cooper<sup>1</sup>, Agnes Michalik<sup>1</sup>, J. Andrew Milton<sup>1</sup>, Thea K. Hincks<sup>1</sup>, Ermias F. Gebru<sup>9,10</sup>, Atalay Ayele<sup>10</sup>, Bekele Abebe<sup>10</sup>, Thomas M. Gernon<sup>1, 11</sup>

<sup>1</sup>School of Ocean and Earth Science, University of Southampton, National Oceanography Centre, European Way, Southampton, SO14 3ZH, UK

<sup>2</sup> Now at: Geography Department, Swansea University, Singleton Park, Sketty, Swansea SA2 8PP

<sup>3</sup>Department of Mathematics and Statistics, Lancaster University, Lancaster, UK

<sup>4</sup>Shell Research Limited, London, UK

<sup>5</sup> Dipartimento di Scienze della Terra, Università degli Studi di Firenze, Firenze 50121, Italy

<sup>6</sup> GEOMAR Helmholtz Centre for Ocean Research Kiel, Kiel, Germany

<sup>7</sup> School of Cosmic Physics, Geophysics Section, Dublin Institute for Advanced Studies, Dublin, Ireland

<sup>8</sup> Dipartimento di Scienze della Terra, Università di Pisa, Pisa 56126, Italy

<sup>9</sup>Department of Geosciences, University of Fribourg, Fribourg, Switzerland

<sup>10</sup>School of Earth Sciences, Addis Ababa University, Addis Ababa, Ethiopia

<sup>11</sup>GFZ Helmholtz Centre for Geosciences, Telegrafenberg, 14473 Potsdam, Germany

\*Corresponding Author Email: [e.j.watts@swansea.ac.uk](mailto:e.j.watts@swansea.ac.uk)

**Mantle upwellings drive large-scale surface volcanism and facilitate continental breakup and ocean basin formation. However, the spatial characteristics and internal composition of these upwellings and how they are modified by plate tectonics are poorly resolved. Afar, East Africa, is a classic triple junction comprising three rifts at various stages of evolution**

thought to be underlain by a mantle upwelling or plume, allowing examination of the controls on the mantle upwelling. Here, we present geochemical data from >130 samples of “young” volcanoes spanning the triple junction to show that the underlying mantle comprises a single, asymmetric upwelling. Using statistical modelling to integrate our data with existing geochemical and geophysical constraints, we suggest that Afar is fed by a spatially and chemically heterogeneous upwelling, which controls the composition and relative abundance of melt in all three rift arms. We identify repetitive signatures in mantle compositions in rift regions, whose variability is a longer wavelength in faster-extending rift arms. This suggests more rapid channelised mantle flow occurs where rifting rates are higher and the plate is thinner, aiding flow of the upwelling towards the faster spreading Red Sea Rift. Our findings demonstrate how the evolution of mantle upwellings are influenced by the dynamics of overriding plates.

The role of mantle upwellings, sometimes interpreted as mantle plumes, in driving volcanism during continental breakup has long been debated (e.g. [1-4]). Moreover, our understanding of rift-plume interactions remains incomplete because only a small fraction of Earth’s upwellings are situated under continents [5] and there are a limited number of upwellings associated with ongoing continental rifting [6]. The Afar triple junction—where the Arabian, Nubian, and Somalian tectonic plates intersect—is a “classic” example of magma-assisted continental rifting. Here, rifting occurred diachronously with the onset of the Gulf of Aden Rift (GoA) at ~35 Ma [7], the Red Sea Rift (RSR) at ~23 Ma [8] and the Main Ethiopian Rift (MER) at ~11 Ma [9]. Both intraplate stresses tied to the slab pull effect of Neo-Tethys subduction [10], and thermal weakening by a mantle upwelling, are thought to have driven rifting [11]. The diachronous onset has led to each rift (GoA, RSR and MER) being in a different phase of maturity (that is, ocean formation, proto-oceanic formation, and mature continental rifting, respectively), and all three rifts are currently volcanically and tectonically active [12], making

it an ideal location to study the interactions between mantle upwelling and rifting, and how these coevolve.

The driver of melt production in Afar is debated, with some models suggesting decompression melting with minimal plume involvement [13], whereas others propose the upwelling of hot, deep mantle [14-17], or indeed multiple upwellings [18, 19]. Whilst several discrete segments of the RSR have been studied in terms of magma petrogenesis (e.g., [16, 20]), a paucity of high-precision geochemical data has hampered evaluation of the spatial characteristics of upwelling across the broader region and rigorously test existing models of the links between tectonics and upwellings.

Here, we implement a comprehensive sampling strategy, targeting evolutionarily young volcanoes spanning the three rifts (Fig. 1). We analyse rocks that are Quaternary in age (i.e., less than 2.58 million years (Myr) old), and from volcanoes that have been active during the Holocene, which began 11.7 thousand years ago (ka) [21]. By targeting younger rocks, we make a direct comparison with geophysical data across the region, enabling an integrated exploration of mantle petrogenesis and dynamics. Our approach utilises statistical methods including semi-parametric regression using splines and K-means cluster analysis to integrate and analyse these geophysical and geochemical data to explore models of upwelling that can explain our data.

## **Characteristics of Mantle Upwellings**

Mantle upwellings that originate between depths of 1,000 and 2,800 km are anomalously hot zones and/or zones of an enriched composition that reduce the solidus temperature of the mantle, enabling increased partial melting [22]. Mantle upwellings are widely accepted to contain a variety of domains of differing proportions (e.g., HIMU, EMI, EMII, C and FOZO [e.g., 5, 22-25]). Such domains typically exhibit an isotopically distinct and enriched

composition (that is, generally low  $^{87}\text{Sr}/^{86}\text{Sr}$ , high  $^{143}\text{Nd}/^{144}\text{Nd}$ , and high  $^{206}\text{Pb}/^{204}\text{Pb}$  [24]) relative to those of bulk silicate Earth (BSE [5]). Trace element ratios such as Ce/Pb and  $\Delta\text{Nb}$  have previously been used to indicate enriched upwellings ( $> 30$  [26],  $>0$  [27] respectively), and La/Sm to suggest the melt fraction relative to the study region with a lower-than-average value suggesting an elevated melt fraction [19]. Mantle upwellings are also commonly associated with reduced (i.e., lower) seismic velocities (i.e., S waves [ $V_s$ ] and P waves [ $V_p$ ]) [28, 29] that are caused by elevated temperatures and/or the presence of fluids and partial melt [30].

Crustal assimilation, where crust components are incorporated into the magma, can obscure these geochemical indicators of a deep mantle plume. However, within the Afar region, crustal contamination has played a relatively minor role in recent magmatism [14] compared to earlier stages of rifting [14, 26], due to the thinning of the present-day crust and that it has been extensively intruded by mafic melts along the length of the rift axes. Seismicity analysis indicates that recent magmatic activity beneath the rift axes in Afar is transient [31] and, in turn, that magmas are unlikely to reside in crustal reservoirs for long enough to extensively assimilate crustal lithologies.

### **Probing the Presence of Mantle Upwelling(s) in Afar**

Our study includes over 130 rock samples, with many from previously unstudied volcanoes, roughly doubling the number of high-quality analyses from the area (Fig. 1). The Afar samples included in our study were carefully selected from a repository covering the broader Afar region (see Methods for details). These were supplemented by 52 additional samples collected during fieldwork in the MER. To examine spatial trends in the geochemistry of surface volcanism, we analysed all samples for major and trace elements alongside radiogenic isotopes (Sr, Nd, Pb; see Methods). We also integrated data for 93 rock samples from the open-



source GEOROC data repository (<https://georoc.eu/> (ref.[32])); see Methods for selection criteria), as well as the classic GoA catalogue from ref.[19]. Additionally, we leverage recent spatial compilations of geophysical variables, such as the depth of the Mohorovičić Discontinuity (Moho) [31] (see Methods) and shear-wave velocities at regularly spaced depths (i.e., 40, 60, 80, 100, and 120 km [30]) across the region. These variables provide well-established proxies for the boundary between the crust and mantle, and for the presence and abundance of melt within the lithosphere and asthenosphere [30]. Collectively, this information allows us to infer details about the depth, compositional characteristics and relative abundance of partial melts distributed across all three rifts.

Based on these samples, we infer wide geochemical variability across the study region (Fig. 1). Delta Niobium ranges from -0.26 to 0.94 and La/Sm ratio ranges from 0.4 to 4.6. The radiogenic isotopes  $^{206}\text{Pb}/^{204}\text{Pb}$ ,  $^{207}\text{Pb}/^{204}\text{Pb}$ ,  $^{208}\text{Pb}/^{204}\text{Pb}$ ,  $^{87}\text{Sr}/^{86}\text{Sr}$  and  $^{143}\text{Nd}/^{144}\text{Nd}$  also display a large range (Fig. 2, Extended Data Table 1), with enrichments relative to BSE occurring in all three rifts. Local variability in these radiogenic isotopes is observed within some volcanoes, e.g., Boset Bericha; however, this variability is smaller than the regional range determined for Afar (Fig. 1).

Across the study region, the depth of the Moho varies, being shallowest in the RSR (~16 km) and deepest in the MER (31 km). Like the geochemical data, the shear-wave velocities ( $V_s$ ) at 40, 60, 80, 100 and 120 km depths show regional variability: 3.81-4.05, 4.06-4.17, 4.00-4.15, 3.97-4.10, 4.02-4.10, respectively (Extended Data Fig. 1). All rifts show zones of high and low  $V_s$  (relative to ref.[30]) in the mantle which vary laterally and in depth.

To evaluate the potential influence of crustal assimilation—considered minor in the Afar region [14]—on mantle composition and upwelling, we assess the correlation between key geochemical and geophysical indicators (Fig. 4a) and the depth to the Moho. The Moho, the

boundary between the crust and mantle, serves as a proxy for crustal thickness, which is widely thought to influence the degree of assimilation [26] (Methods). We found that most indicators, including Pb isotopes—a reliable indicator of crustal assimilation [34]—exhibit only a weak, but statistically significant, correlation with Moho depth (Fig. 4a). Further, Ce/Pb exhibits a strong negative correlation (i.e., Pearson correlation coefficient of -0.7), indicating that where the crust is thin, the Ce/Pb values are high, and vice versa. This trend can be attributed to minimal crustal assimilation across most of the Afar region, though the degree of assimilation increases as the crust thickens within the MER.

Overall, our dataset shows geochemical and geophysical variability across the study area, which are consistent with the presence of an upwelling across all three rifts. The spatial trends observed in all variables implicate an underlying complexity to the location of partial melts.

### **Models of the Afar Upwelling**

We used our data to test multiple conceptual models of mantle upwelling dynamics. The initial conceptual model we considered is a simple, homogeneous mantle upwelling at the triple junction (e.g., ref.[19]). This model expects variables (geochemical and geophysical) that indicate deep upwelling to change radially with distance from the upwelling centre (C1C – 1 centre, concentric; Fig. 3, Extended Data Table 2). Therefore, this model assumes that variables change linearly from the upwelling centre due to lateral spreading. Extending this model, we then allow the upwelling to be spatially and temporally heterogeneous, as reported for the Hawaiian [35] and Canary Island [36] volcanoes. This mechanism yields a similar pattern to the linear C1C model but accommodates compositional fluctuations over the radial distance corresponding to a chemically pulsed upwelling (Fig. 3). This model fits a single spline per parameter for all data against distance from the upwelling centre (spline C1C). The optimum spline allows for regional variations to be accounted for, whilst minimising noise (i.e., optimal

smoothing). This approach of both linear and spline fits is applied to all further models described in this section allowing for homogenous and heterogeneous upwelling(s), respectively. Note the starting composition of the upwelling is not constrained within the model parameters.

We additionally tested whether the spatial geochemical and geophysical variations observed (Fig. 1 and Extended Data Fig. 1) are best explained through the presence of three small-scale upwellings, which have been proposed based on geophysics and numerical models (e.g. ref.[37], C3C – 3 centres, concentric; Fig. 3; Extended Data Table 1). We tested this model using three upwellings: one centred on the triple junction, one in the northern RSR, and one in the southern MER, with the positions of these loci informed by previous models and observations (Methods). This model fits one linear/spline regression per variable (against distance) from the nearest upwelling centre and assumes that the upwellings are compositionally identical and from the same deep source.

It is plausible that the variable tectonic regime (e.g., extension rate, crustal thickness) between the three rifts [12] introduces further complexity to the geochemical and geophysical signals. Accordingly, we introduce three further models, C1D, C3D, and C3X (Fig. 3, Extended Data Table 2; Methods) to account for these regional differences. Models C1D (1 centre, different spreading) and C3D (3 centres, different spreading) consider one upwelling and three small-scale upwellings, respectively, while allowing for distinct distance-dependent patterns for each rift, thereby modelling the distribution of variables across each rift independently. Unlike the other models, C3X (3 independent centres, different spreading) allows each small-scale upwelling to have a distinct signature, as well as permitting an independent distribution along each rift (Methods).

### **Spatial Characteristics of Afar Mantle Upwelling**

To test these models (Fig 3, Extended Data Table 2), we identify 14 key geochemical and geophysical variables (for descriptions, see Extended Table 2) and calculate the distance, using the spherical cosine law (Methods), between the purported upwelling centre [15, 19, 38] and each observation site (Methods). We then apply two-deep cross validation (100 iterations) to find the optimum linear fit (that is, representing a homogeneous upwelling) and penalised B-spline fit (that is, representing a heterogeneous upwelling) to each of the variables, using all data points, over a radial distance of 500 km—the radial limit of samples considered within our study (Fig. 4b and Extended Data Fig. 2). The predictive performance of each fit is then assessed by calculating the mean standardised root-mean squared error of prediction (RMSEP), where a value of 1 indicates a lack of predictive capability, and 0 a perfect predictive ability (Fig. 4c).

For all models, we observe the B-spline fit (i.e., a class of polynomial function; Methods) to have the best predictive performance, compared to a linear fit (Fig. 4c). This indicates that a compositionally heterogeneous upwelling in Afar is most probable (Figs. 4b and 4c).

The analysis indicates that the overall best predictive model is the B-spline fit of model C1D, wherein a single, heterogeneous mantle upwelling is present, albeit with differing distributions of geochemical and geophysical variables between rift-arms (Fig. 3; Extended Data Table 2). This model yields a mean standardised RMSEP of 0.59 (Fig. 4c), lower than that of the other models. To further validate our results, we carried out sensitivity analysis, varying the geochemical and geophysical data about their known uncertainties (see Methods). The results confirm that model C1D remains the most accurate predictive model (Fig. 4c).

Whilst the RSR and MER have a high sample density, there is limited sample availability from the GoA due to poor access. When excluding the GoA from our analyses, the overall trend between the models remains effectively the same (Extended Data Fig. 3b). Although the Afar

rifts share a single, compositionally heterogeneous upwelling, they appear to behave independently, implying that some feature of their tectonic regime modulates the observed signals.

## **Interplay Between Upwelling and Segmentation**

Many of the optimum splines for each rift display distance-dependent sinusoidal patterns (Fig. 4b; Extended Data Fig. 2). Importantly, our analysis indicates that the variability observed for some variables within the MER exhibit greater amplitude and shorter periodicity with distance from the centre of the upwelling compared to those of the RSR (Fig. 4b; Extended Data Fig. 2). Further, the observed variation in Pb isotopes within the RSR suggests that the upwelling may be chemically heterogeneous for some elements, whereas others show a narrower range in composition (e.g.,  $^{87}\text{Sr}/^{86}\text{Sr}$  is more heterogeneous than  $^{143}\text{Nd}/^{144}\text{Nd}$ ; Fig 1; Extended Data Fig 1). Although  $\Delta\text{Nb}$  values are almost consistently positive ( $>0$ ) across the region (except around Boset-Bericha Volcano), we identify small-scale differences in La/Sm and Vs at 100 km depth, within the likely melt-rich zone of the asthenosphere [26], with distance to upwelling centre in each rift (Fig. 4b; Extended Data Fig. 2). These small-scale differences indicate locally variable degrees of melting across the study region, agreeing with previous studies that reported low velocity areas [e.g., 37, 39]. This raises the question: do the zones of locally higher melt fraction, low Vs, and variable geochemistry observed in one rift correspond, spatially and compositionally, to those observed in the other two rifts? If so, this could indicate a shared melt source.

To address the spatial heterogeneity patterns observed and investigate the potential shared melt source, we carried out principal component analysis (PCA) and K-means cluster analysis using all variables post-standardisation (Methods). Across all variables, the K-means cluster analysis algorithm seeks to group similar observations whilst minimising the within-cluster total sum

of squares for a pre-specified number of clusters. Our K-means cluster analysis shows a higher number of clusters that are smaller in geographic size for the MER (50-100 km length scale; 4 clusters) compared to the RSR (150-200 km length scale; 3 clusters) (Fig. 5; Methods). Several clusters (clusters 1-3) are found to co-exist in different rift-arms. For example, samples assigned to cluster 3 are observed in the distal section of the RSR, as well as in locations closer to the MER rift centre (Fig. 5). The three clusters (1-3) observed across the RSR match the initial ~200 km clustering sequence observed across the MER. This sequential repeated clustering may indicate that they are derived from a shared source melt. However, the sequence of these melts—as indicated by clusters—within the MER occurs over a shorter distance compared to that of the RSR.

The spatial distribution of clusters reflects spatial variations in the composition and abundance of melt, which shares some cursory similarities to the magmatic segments observed at the surface (Fig. 5). However, when inspected in detail we observe clear differences. For example, volcanic systems both within magmatic segments and the adjacent rift flanks are commonly allocated to single clusters, and the boundaries between clusters and known magmatic segments are typically mismatched (Fig. 5). In Afar, the length of the region containing clusters is longer than that of magmatic segments. We therefore infer that the compositional variability of mantle upwelling is unlikely to be related to the along-axis segmentation of crustal subvolcanic plumbing systems.

### **Tectonic Control on Flow of Upwelling**

Taken together, our data can be explained through a single upwelling model with internal heterogeneity between rifts (e.g., refs.[31, 35, 40, 41]), as shown by the spline model. Crucially, the K-means cluster analysis indicates the signatures of geochemical variability (i.e., clusters) are repeated across rifts, implicating pulses of upwelling from the same source, as inferred for

other mantle plumes (e.g., refs.[36, 40, 41]). Rifts act as natural channels for upwelling melt from deeper mantle sources [42]. Considering the high extension rate in the RSR (10.5-19.5 mm/yr; [43]) compared to that of the MER (~5.2 mm/yr; [43]), it is plausible that a mantle flow rate is impeded by the narrowing of the rift in the MER. This process would lead to a ‘bottleneck’ effect [42, 44, 45], which in turn may result in a different length scale of mantle heterogeneity (Fig. 4; Extended Data Fig. 2) between the RSR and MER (Fig. 5). Further, a contrast in crustal thickness is evident between the rifts, with the MER crust being thicker (25-33 km [46]) than that of RSR (16-25 km [47]; Extended Data Fig. 1). Assuming a correlation between crustal and overall plate thickness, this effect is expected to introduce differences in mantle flow rate along each rift in Afar. A progressive thickening of the overlying lithosphere away from the upwelling centre in the MER should reduce the volume capacity for melt, impeding mantle flow. Consequently, the heterogeneous nature of the pulsed upwelling would exhibit a more condensed spatial pattern within the MER compared to RSR, as we observe (Fig. 5).

We conclude that variations in melt composition and abundance in and around Afar is best explained by a heterogeneous pulsing mantle upwelling that is not symmetrical (Fig. 5) but is instead shaped by both variable lithospheric thinning and extension rates within each rift (Fig. 6). Whilst this model principally investigates the likelihood of a singular or three-small-scale upwelling scenario, our results demonstrate that for either option, a single heterogeneous upwelling provides the best match to observations in the region. The detected variations in melt composition and abundance between the MER and RSR imply that the length scale of heterogeneities within magma-assisted rifting environments may be controlled not only by the upwelling itself, but by the extension rate and plate thickness. If this model is correct, it demonstrates that the evolution of a mantle upwelling can be influenced and shaped by the dynamics of the overriding plates.

## Acknowledgements

E.J.W was supported by Natural Environmental Research Council UK through the SPITFIRE Doctoral Training Partnership [grant number [NE/L002531/1](#)] and Wyley Fund of the Geologists' Association. E.J.W. is currently supported as part of the UKRI FLF award held at Swansea University (MR/YO11767/1). T.G. and T.H. receive funding from the WoodNext Foundation, a component fund administered by the Greater Houston Community Foundation. We acknowledge the use of rocks from the Afar Repository of the University of Pisa, Italy (<http://repositories.dst.unipi.it/index.php/home-afar>). We appreciate all those directly or indirectly involved in the field-campaign in the 1960s and acknowledge their contributions to the growing research within the region. We thank G.L. Foster and M. Cassidy for their helpful comments on an early version of the manuscript.

## Author Contributions

E.J.W. conceived the idea, processed the data, and prepared the manuscript. T.M.G and D.K. advised on the work and assisted with sampling and interpretation. P.J. wrote the code for the statistical modelling and assisted with interpretation. T.K.H advised on the statistical analysis. E.J.W., R.R., M.S., M.J.C., A.M., J.A.M., and R.N.T analysed the samples and processed the geochemical data. E.L.C processed the geophysical data for the sample locations. E.J.W., T.M.G., and D.K. wrote the manuscript with input from all co-authors.

## Competing Interests Statement

The authors declare no competing interests.



## Figure Captions

**Fig. 1: Variation in geochemical and geophysical properties around the Afar Triangle;** (a) Map showing the Gulf of Aden Rift (GoA), Red Sea Rift (RSR) and the Main Ethiopian Rift (MER) axes (dashed lines) and associated rifting rates indicated by arrows (from refs. [43,48]). The three hypothesised [19, 37, 38] upwelling locations (yellow stars) and Holocene volcanoes (red triangles) are shown. Hexmap colours show the density of samples within the hexagons' area, with purple representing >12 and yellow showing 1-2. Location of maps shown on global inset (black rectangle). (b) Hexmap showing the  $^{206}\text{Pb}/^{204}\text{Pb}$  variations across the study region (dark blue = low  $^{206}\text{Pb}/^{204}\text{Pb}$  - minimal upwelling signature, yellow = high  $^{206}\text{Pb}/^{204}\text{Pb}$ ). (c) Hexmap showing La/Sm variations across the study region (yellow = high La/Sm – low melt fraction, dark blue = low La/Sm – high melt fraction). (d) Hexmap showing the  $^{143}\text{Nd}/^{144}\text{Nd}$  variations across the study region. Yellow indicates a high  $^{143}\text{Nd}/^{144}\text{Nd}$ . The topography shown is from the 1 arc-sec (~30 m resolution) Shuttle Radar Topography Mission (SRTM) Digital Elevation Model (DEM) [50].

**Fig. 2: Radiogenic isotope compositions of samples across Afar.** (a)  $^{206}\text{Pb}/^{204}\text{Pb}$  versus  $^{208}\text{Pb}/^{204}\text{Pb}$ ; (b)  $^{143}\text{Nd}/^{144}\text{Nd}$  versus  $^{87}\text{Sr}/^{86}\text{Sr}$ . Samples are classified by their rift position, indicated by their symbol colour and shape (RSR = blue circles, MER = green squares, GoA = yellow diamonds). Error bars show the uncertainty associated. Black error bars are the average uncertainty of the dataset, grey are the maximum uncertainty. Uncertainty for datapoints in (a) are smaller than the symbols. The global mantle endmember compositions are shown as fields behind from refs.[5, 49]. The histograms show the distribution of all data analysed in our study, including our >130 data points.

**Fig. 3: Conceptual models of mantle upwellings beneath Afar tested in this study.** Schematic diagram of the upwelling scenarios for Afar tested in this study. The diagrams (left) are labelled

with the code associated with each model (see Extended Data Table 2 and the Statistical Analysis section within Methods for further details). The location of the purported mantle upwellings are shown by the star symbol. The number of lines shown on the schematic graphs equals the number of models that must be fitted for that model variant (linear = dashed, spline = continuous), where R = Rift and U = upwelling. Note that each model variant has been illustrated with an indicator that decreases with a reduction in upwelling proportion.

**Fig. 4: Statistical analysis of rifting models for the RSR, GoA and MER.** (a) Pearson correlation coefficient of each of the selected 13 variables with Moho depth. Error bars show the 95-percentile error of the coefficient ( $n = 250$ ) with the squares representing the mean. Red squares indicate where the correlation is significant ( $p < 0.05$ ) and blue squares indicate that the correlations are not deemed significant ( $p > 0.05$ ). (b) Splines (a smooth, flexible polynomial curve) of the best overall model—that is, C1C—for selected variables. Symbols show the data within the study (locations denoted by symbols shown). 95% confidence intervals are indicated by the shaded background. The number of data observations ( $n$ ) for La/Sm,  $^{143}\text{Nd}/^{144}\text{Nd}$ ,  $^{206}\text{Pb}/^{204}\text{Pb}$  and Shear velocity at 100km depth are 269, 218, 185, and 184 respectively. Uncertainty in data values have been shown by error bars (average in black, max in grey). (c) The mean standardised root means square error of prediction (RMSEP) for each of the models tested. Individual linear model results are shown by red squares and the mean of those results are displayed by the red line. Individual spline results are shown by blue circles and the mean of those results are shown by a blue line. All models were run for 100 iterations to capture the probable uncertainty distribution, as shown by the data points. Mean (dotted line) and 95% confidence interval (shaded) of results using perturbed data (within the uncertainty of each datapoint) are also shown (300 perturbation runs each using 100 iterations).

**Fig. 5: Map of the segments and cluster assignment within the study region.** Segments are shown in blue from north to south: Erta Ale Volcanic Segment (EAVS), Tat'Ale Volcanic

Segment (TAVS), Alayta Volcanic Segment (AVS), Dabbahu Volcanic Segment (DVS), Gabillemma Volcanic Segment (GVS), Adda'do Magmatic Segment (AMS), Fentale-Dofen Magmatic Segment (FDMS), Boset Magmatic Segment (BMS), Aluto-Gedamsa Magmatic Segment (AGMS), Corbetti Magmatic Segment (CMS). Rift axis (dotted line) is shown. (b) and (c) are enlarged maps of the boxes shown in (a). (d) & (e) Principal component (PC) analysis bi-plot (PC1 vs PC2) when considering the six isotopic systems (see Extended Data Table 3) showing the samples and their component scores relative to those of the mantle endmembers. Values used for the mantle endmembers, that is, Pan-African Lithosphere (PAL), Enriched Mantle 1 & 2 (EM1, EM2, respectively), Depleted MORB Mantle (DMM) and HiMU, are shown in Extended Table 3. The topography shown is from the 1 arc-sec (~30 m resolution) Shuttle Radar Topography Mission (SRTM) Digital Elevation Model (DEM) [50].

**Fig. 6: Spatially heterogeneous nature of the mantle upwelling beneath Afar.** (a) Box diagram showing the rifts across Afar and the mantle upwelling being channelised by the rift. The lines of section X-Y-Z are those shown in panel (c). Volcanic segments are shown and labelled: Erta Ale Volcanic Segment (EAVS), Tat'Ale Volcanic Segment (TAVS), Alayta Volcanic Segment (AVS), Dabbahu Volcanic Segment (DVS), Gabillemma Volcanic Segment (GVS), Adda'do Magmatic Segment (AMS), Fentale-Dofen Magmatic Segment (FDMS). (b) Schematic of the Afar upwelling showing the dimensions of channelised flow along the three rifts (dashed lines). (c) Schematic cross sections along the Red Sea Rift (line section X-Y) and MER (Y-Z) showing the distribution of chemical heterogeneities within the upwelling and how those map to the clusters shown in Fig. 5. Note that the depths of distinct features including the Lithosphere-Asthenosphere Boundary (LAB) are not shown to scale.

## References

- [1] Cañón-Tapia, E., & Walker, G. P. (2004). Global aspects of volcanism: the perspectives of “plate tectonics” and “volcanic systems”. *Earth-Science Reviews*, 66(1-2), 163-182. <https://doi.org/10.1016/j.earscirev.2003.11.001>
- [2] White, R., & McKenzie, D. (1989). Magmatism at rift zones: the generation of volcanic continental margins and flood basalts. *Journal of Geophysical Research: Solid Earth*, 94(B6), 7685-7729. <https://doi.org/10.1029/JB094IB06P07685>
- [3] Koptev, A., Calais, E., Burov, E., Leroy, S., & Gerya, T. (2015). Dual continental rift systems generated by plume–lithosphere interaction. *Nature Geoscience*, 8(5), 388-392. <https://doi.org/10.1038/ngeo2401>
- [4] Fitton, J. G. (1983). Active versus passive continental rifting: evidence from the West African rift system. *Tectonophysics*, 94(1-4), 473-481. [https://doi.org/10.1016/0040-1951\(83\)90030-6](https://doi.org/10.1016/0040-1951(83)90030-6)
- [5] Zindler, A., & Hart, S. (1986). Chemical geodynamics. IN: *Annual review of earth and planetary sciences*. Volume 14 (A87-13190 03-46). Palo Alto, CA, Annual Reviews, Inc., 1986, p. 493-571., 14, 493-571.
- [6] Rogers, N., Macdonald, R., Fitton, J. G., George, R., Smith, M., & Barreiro, B. (2000). Two mantle plumes beneath the East African rift system: Sr, Nd and Pb isotope evidence from Kenya Rift basalts. *Earth and Planetary Science Letters*, 176(3-4), 387-400. [https://doi.org/10.1016/S0012-821X\(00\)00012-1](https://doi.org/10.1016/S0012-821X(00)00012-1)
- [7] Leroy, S., d'Acremont, E., Tiberi, C., Basuyau, C., Autin, J., Lucazeau, F., & Sloan, H. (2010). Recent off-axis volcanism in the eastern Gulf of Aden: implications for plume–ridge

- 379 interaction. *Earth and Planetary Science Letters*, 293(1-2), 140-153.  
 380 <https://doi.org/10.1016/j.epsl.2010.02.036>
- 381 [8] Szymanski, E., Stockli, D. F., Johnson, P. R., & Hager, C. (2016). Thermochronometric  
 382 evidence for diffuse extension and two-phase rifting within the Central Arabian Margin of the  
 383 Red Sea Rift. *Tectonics*, 35(12), 2863-2895. <https://doi.org/10.1002/2016TC004336>
- 384 [9] Wolfenden, E., Ebinger, C., Yirgu, G., Deino, A., & Ayalew, D. (2004). Evolution of the  
 385 northern Main Ethiopian rift: birth of a triple junction. *Earth and Planetary Science Letters*,  
 386 224(1-2), 213-228. <https://doi.org/10.1016/j.epsl.2004.04.022>
- 387 [10] Bellahsen, N., Faccenna, C., Funicello, F., Daniel, J. M., & Jolivet, L. (2003). Why did  
 388 Arabia separate from Africa? Insights from 3-D laboratory experiments. *Earth and Planetary*  
 389 *Science Letters*, 216(3), 365-381. [https://doi.org/10.1016/S0012-821X\(03\)00516-8](https://doi.org/10.1016/S0012-821X(03)00516-8)
- 390 [11] Koptev, A., Gerya, T., Calais, E., Leroy, S., & Burov, E. (2018). Afar triple junction  
 391 triggered by plume-assisted bi-directional continental break-up. *Scientific reports*, 8(1), 14742.  
 392 <https://doi.org/10.1038/s41598-018-33117-3>
- 393 [12] Zwaan, F., Corti, G., Keir, D., & Sani, F. (2020). A review of tectonic models for the rifted  
 394 margin of Afar: Implications for continental break-up and passive margin formation. *Journal*  
 395 *of African Earth Sciences*, 164, 103649. <https://doi.org/10.1016/j.jafrearsci.2019.103649>
- 396 [13] Rychert, C. A., Hammond, J. O., Harmon, N., Michael Kendall, J., Keir, D., Ebinger, C.,  
 397 ... & Stuart, G. (2012). Volcanism in the Afar Rift sustained by decompression melting with  
 398 minimal plume influence. *Nature Geoscience*, 5(6), 406-409. <https://doi.org/10.1038/ngeo1455>
- 399 [14] Rooney, T. O. (2020). The Cenozoic magmatism of East Africa: part IV—the terminal  
 400 stages of rifting preserved in the Northern East African Rift System. *Lithos*, 360, 105381.  
 401 <https://doi.org/10.1016/j.lithos.2020.105381>

- 402 [15] Schilling, J. G. (1973). Afar mantle plume: rare earth evidence. *Nature Physical Science*,  
 403 242(114), 2-5. <https://doi.org/10.1038/physci242002a0>
- 404 [16] Ferguson, D. J., MacLennan, J., Bastow, I. D., Pyle, D. M., Jones, S. M., Keir, D., ... &  
 405 Yirgu, G. (2013). Melting during late-stage rifting in Afar is hot and deep. *Nature*, 499(7456),  
 406 70-73. <https://doi.org/10.1038/nature12292>
- 407 [17] Armitage, J. J., Ferguson, D. J., Goes, S., Hammond, J. O., Calais, E., Rychert, C. A., &  
 408 Harmon, N. (2015). Upper mantle temperature and the onset of extension and break-up in Afar,  
 409 Africa. *Earth and Planetary Science Letters*, 418, 78-90.  
 410 <https://doi.org/10.1016/j.epsl.2015.02.039>
- 411 [18] Hansen, S. E., & Nyblade, A. A. (2013). The deep seismic structure of the Ethiopia/Afar  
 412 hotspot and the African superplume. *Geophysical Journal International*, 194(1), 118-124.  
 413 <https://doi.org/10.1093/gji/ggt116>
- 414 [19] Schilling, J. G., Kingsley, R. H., Hanan, B. B., & McCully, B. L. (1992). Nd-Sr-Pb  
 415 isotopic variations along the Gulf of Aden: Evidence for Afar mantle plume-continental  
 416 lithosphere interaction. *Journal of Geophysical Research: Solid Earth*, 97(B7), 10927-10966.  
 417 <https://doi.org/10.1029/92jb00415>
- 418 [20] Hagos, M., Koeberl, C., & de Vries, B. V. W. (2016). The Quaternary volcanic rocks of  
 419 the northern Afar Depression (northern Ethiopia): Perspectives on petrology, geochemistry,  
 420 and tectonics. *Journal of African Earth Sciences*, 117, 29-47.  
 421 <https://doi.org/10.1016/J.JAFREARSCI.2015.11.022>
- 422 [21] Global Volcanism Program, 2024. [Database] Volcanoes of the World (v. 5.2.5; 23 Dec  
 423 2024). Distributed by Smithsonian Institution, compiled by Venzke, E.  
 424 <https://doi.org/10.5479/si.GVP.VOTW5-2024.5.2>

- [22] Weis, D., Harpp, K. S., Harrison, L. N., Boyet, M., Chauvel, C., Farnetani, C. G., ... & Williamson, N. M. (2023). Earth's mantle composition revealed by mantle plumes. *Nature Reviews Earth & Environment*, 4(9), 604-625. <https://doi.org/10.1038/s43017-023-00467-0>
- [23] Jackson, M. G., Becker, T. W., & Steinberger, B. (2021). Spatial characteristics of recycled and primordial reservoirs in the deep mantle. *Geochemistry, Geophysics, Geosystems*, 22(3), e2020GC009525. <https://doi.org/10.1029/2020GC009525>
- [24] Hart, S. R., Hauri, E. H., Oschmann, L. A., & Whitehead, J. A. (1992). Mantle plumes and entrainment: isotopic evidence. *Science*, 256(5056), 517-520. <https://doi.org/10.1126/SCIENCE.256.5056.517>
- [25] Hanan, B. B., & Graham, D. W. (1996). Lead and helium isotope evidence from oceanic basalts for a common deep source of mantle plumes. *Science*, 272(5264), 991-995. <https://doi.org/10.1126/science.272.5264.991>
- [26] Hutchison, W., Mather, T. A., Pyle, D. M., Boyce, A. J., Gleeson, M. L., Yirgu, G., ... & Finch, A. A. (2018). The evolution of magma during continental rifting: New constraints from the isotopic and trace element signatures of silicic magmas from Ethiopian volcanoes. *Earth and Planetary Science Letters*, 489, 203-218. <https://doi.org/10.1016/j.epsl.2018.02.027>
- [27] Fitton, J. G., Saunders, A. D., Norry, M. J., Hardarson, B. S., & Taylor, R. N. (1997). Thermal and chemical structure of the Iceland plume. *Earth and Planetary Science Letters*, 153(3-4), 197-208. [https://doi.org/10.1016/S0012-821X\(97\)00170-2](https://doi.org/10.1016/S0012-821X(97)00170-2)
- [28] Benoit, M. H., Nyblade, A. A., & VanDecar, J. C. (2006). Upper mantle P-wave speed variations beneath Ethiopia and the origin of the Afar hotspot. *Geology*, 34(5), 329-332. <https://doi.org/10.1130/G22281.1>

- 447 [29] Ritsema, J., & Allen, R. M. (2003). The elusive mantle plume. *Earth and Planetary Science*  
 448 *Letters*, 207(1-4), 1-12. [https://doi.org/10.1016/S0012-821X\(02\)01093-2](https://doi.org/10.1016/S0012-821X(02)01093-2)
- 449 [30] Chambers, E. L., Harmon, N., Rychert, C. A., Gallacher, R. J., & Keir, D. (2022). Imaging  
 450 the seismic velocity structure of the crust and upper mantle in the northern East African Rift  
 451 using Rayleigh wave tomography. *Geophysical Journal International*, 230(3), 2036-2055.  
 452 <https://doi.org/10.1093/gji/ggac156>
- 453 [31] Illsley-Kemp, F., Keir, D., Bull, J. M., Gernon, T. M., Ebinger, C., Ayele, A., ... &  
 454 Belachew, M. (2018). Seismicity during continental breakup in the Red Sea rift of Northern  
 455 Afar. *Journal of Geophysical Research: Solid Earth*, 123(3), 2345-2362.  
 456 <https://doi.org/10.1002/2017JB014902>
- 457 [32] DIGIS Team: GEOROC Compilation: Rift Volcanics (2021).  
 458 <https://doi.org/10.25625/KAIVCT>
- 459 [33] Chambers, E. L., Harmon, N., Keir, D., & Rychert, C. A. (2019). Using ambient noise to  
 460 image the northern East African Rift. *Geochemistry, Geophysics, Geosystems*, 20(4), 2091-  
 461 2109. <https://doi.org/10.1029/2018GC008129>
- 462 [34] Hofmann, A. W., Jochum, K. P., Seufert, M., & White, W. M. (1986). Nb and Pb in  
 463 oceanic basalts: new constraints on mantle evolution. *Earth and Planetary science letters*, 79(1-  
 464 2), 33-45. [https://doi.org/10.1016/0012-821X\(86\)90038-5](https://doi.org/10.1016/0012-821X(86)90038-5)
- 465 [35] Abouchami, W., Hofmann, A. W., Galer, S. J. G., Frey, F. A., Eisele, J., & Feigenson, M.  
 466 (2005). Lead isotopes reveal bilateral asymmetry and vertical continuity in the Hawaiian  
 467 mantle plume. *Nature*, 434(7035), 851-856. <https://doi.org/10.1038/nature03402>



- 468 [36] Taylor, R. N., Davila-Harris, P., Branney, M. J., Farley, E. R., Gernon, T. M., & Palmer,  
469 M. R. (2020). Dynamics of a chemically pulsing mantle plume. *Earth and Planetary Science*  
470 *Letters*, 537, 116182. <https://doi.org/10.1016/j.epsl.2020.116182>
- 471 [37] Civiero, C., Armitage, J. J., Goes, S., & Hammond, J. O. (2019). The seismic signature of  
472 upper-mantle plumes: Application to the Northern East African Rift. *Geochemistry,*  
473 *Geophysics, Geosystems*, 20(12), 6106-6122. <https://doi.org/10.1029/2019GC008636>
- 474 [38] Rooney, T. O., Hanan, B. B., Graham, D. W., Furman, T., Blichert-Toft, J., & Schilling,  
475 J. G. (2012). Upper mantle pollution during Afar plume–continental rift interaction. *Journal of*  
476 *Petrology*, 53(2), 365-389. <https://doi.org/10.1093/petrology/egr065>
- 477 [39] Gallacher, R. J., Keir, D., Harmon, N., Stuart, G., Leroy, S., Hammond, J. O., ... & Ahmed,  
478 A. (2016). The initiation of segmented buoyancy-driven melting during continental breakup.  
479 *Nature Communications*, 7(1), 13110. <https://doi.org/10.1038/ncomms13110>
- 480 [40] Ito, G. (2001). Reykjanes' V'-shaped ridges originating from a pulsing and dehydrating  
481 mantle plume. *Nature*, 411(6838), 681-684. <https://doi.org/10.1038/35079561>
- 482 [41] Parkin, C. J., Lunnø, Z. C., White, R. S., Christie, P. A., & Integrated Seismic Imaging  
483 & Modelling of Margins Project (iSIMM) Team. (2007). Imaging the pulsing Iceland mantle  
484 plume through the Eocene. *Geology*, 35(1), 93-96. <https://doi.org/10.1130/G23273A.1>
- 485 [42] Ebinger, C. J., & Sleep, N. H. (1998). Cenozoic magmatism throughout east Africa  
486 resulting from impact of a single plume. *Nature*, 395(6704), 788-791.  
487 <https://doi.org/10.1038/27417>
- 488 [43] Zwaan, F., Corti, G., Sani, F., Keir, D., Muluneh, A. A., Illsley-Kemp, F., & Papini, M.  
489 (2020). Structural analysis of the Western Afar Margin, East Africa: Evidence for multiphase  
490 rotational rifting. *Tectonics*, 39(7), e2019TC006043. <https://doi.org/10.1029/2019TC006043>

- [44] Chang, S. J., & Van der Lee, S. (2011). Mantle plumes and associated flow beneath Arabia and East Africa. *Earth and Planetary Science Letters*, 302(3-4), 448-454. <https://doi.org/10.1016/j.epsl.2010.12.050>
- [45] Hansen, A. H. (2023) "Flow Through Restriction." In *Fluid Power Systems: A Lecture Note in Modelling, Analysis and Control*, pp. 43-61. Cham: Springer International Publishing. [https://doi.org/10.1007/978-3-031-15089-0\\_4](https://doi.org/10.1007/978-3-031-15089-0_4)
- [46] Maguire, P. K. H., Keller, G. R., Klemperer, S. L., Mackenzie, G. D., Keranen, K., Harder, S., O'Reilly, B., Thybo, H., Asfaw, L., Khan, M. A., & Amha, M. (2006). Crustal structure of the northern Main Ethiopian Rift from the EAGLE controlled-source survey; a snapshot of incipient lithospheric break-up. *Geological Society, London, Special Publications*, 259(1), 269-292. <https://doi.org/10.1144/GSL.SP.2006.259.01.21>
- [47] Lewi, E., Keir, D., Birhanu, Y., Blundy, J., Stuart, G., Wright, T., & Calais, E. (2016). Use of a high-precision gravity survey to understand the formation of oceanic crust and the role of melt at the southern Red Sea rift in Afar, Ethiopia. *Special Publications*, 420(1), 165-180. <https://doi.org/10.1144/SP420.13>
- [48] Gillard, M., Leroy, S., Cannat, M., & Sloan, H. (2021). Margin-to-margin seafloor spreading in the eastern Gulf of Aden: a 16 Ma-long history of deformation and magmatism from seismic reflection, gravity and magnetic data. *Frontiers in Earth Science*, 9, 707721. <https://doi.org/10.3389/feart.2021.707721>
- [49] Rollinson, H., & Pease, V. (2021). Using Radiogenic Isotope Data. In *Using Geochemical Data: To Understand Geological Processes* (pp. 178–218). chapter, Cambridge: Cambridge University Press.

513 [50] NASA JPL (2013). NASA Shuttle Radar Topography Mission Global 1 arc second [Data  
514 set]. NASA EOSDIS Land Processes DAAC. Accessed 2021-09-03  
515 from <https://doi.org/10.5067/MEaSUREs/SRTM/SRTMGL1.003>

## Methods

### *Sample Selection and Processing*

All samples and previously published data used in this study must originate from a volcano that has been active within the Holocene [21] (Fig. 1), with the age of the sample estimated to be of Quaternary age (i.e., < 2.58 Ma). An essential criterion was that all samples have a precisely known location with accurate coordinates.

### *Obtaining Previously Published Data*

Previously published geochemical data were obtained from GeoROC [19, 32]. Once downloaded the data-files were filtered to only include data within Ethiopia (including the Main Ethiopian Rift and Afar). These data were further filtered using the following criteria:

1. The values for the sample must relate to whole rock geochemistry, as opposed to mineral separates.
2. The individual sample must have major element, trace element,  $^{87}\text{Sr}/^{86}\text{Sr}$ ,  $^{143}\text{Nd}/^{144}\text{Nd}$ ,  $^{206}\text{Pb}/^{204}\text{Pb}$ ,  $^{207}\text{Pb}/^{204}\text{Pb}$  and  $^{208}\text{Pb}/^{204}\text{Pb}$  isotope values available.
3. The coordinates must be specific to the individual sample's location rather than providing an average coordinate for a broader study area.

### *Sampling and Sample Preparation*

Ninety-three lavas, eleven welded tuffs and one pumice sample, from various volcanoes in Afar (Erta Ale Volcanic Segment, Ayelu, Abida, Yangudi, Dama Ali, Kerub, Ela, Didoli, Abbahu, Afdera, Tat Ali and Manda Hararo) were selected for geochemical analysis [see refs.51-53]. The samples were collected during the CNR/CNRS projects in Afar during the 1960s [54] and stored in the Afar Repository at the University of Pisa, Italy, (<http://repositories.dst.unipi.it/index.php/home-afar>). A further 52 samples from the Boset-

Bericha Volcanic Complex (BBVC) were collected during three field seasons [ref.55], in November 2012, April-May 2015 [ref.56], and February 2017 [ref.57].

Sample preparation, for major, trace and isotope analyses, was carried out at the University of Southampton. Samples were cut with a saw to remove any weathered sections, and any cut surfaces ground down to reduce any potential contamination by metals from the saw blade. Rock samples were then crushed using a fly press and placed in double-layered plastic bags prior to crushing to minimise metal contamination during the crushing process.

The crushed material was separated into three size fractions ( $>1$  mm, 0.5 mm to 1 mm,  $<0.5$  mm) using Teflon sieves, retaining the middle fraction (0.5 - 1 mm) for analysis. The selected fraction was cleaned by ultrasonication in Milli-Q water then dried overnight in an oven at  $85^{\circ}\text{C}$ . The cleaned rock chips were then hand-picked under a microscope, to remove any extraneous (non-rock) material. An aliquot of cleaned chips was used for Pb isotope analysis. For major element, trace element, and  $^{143}\text{Nd}/^{144}\text{Nd}$  and  $^{87}\text{Sr}/^{86}\text{Sr}$  isotope analysis, the remaining rock chips were ground to a fine powder using an agate mortar and pestle, again to minimise contamination with metals.

#### ***Trace Element Analysis***

Samples were prepared for whole-rock trace element analysis using 0.05 g (for BBVC samples) or 0.075 g (for all other samples) powdered sample. The powdered samples were digested in sealed Savillex Teflon vials with 15 drops concentrated  $\text{HNO}_3$  and 2 ml HF on a hotplate at  $130^{\circ}\text{C}$  for 24 hours (for all samples excluding those from the BBVC), or with 50 drops HF and 0.2 ml  $\text{HNO}_3$  on a hotplate at  $130^{\circ}\text{C}$  for 24 hours (for BBVC samples only). The  $\text{HNO}_3$ /HF was evaporated off, and the samples were refluxed in 6M HCl for another 24 hours on a hotplate at  $130^{\circ}\text{C}$ . The 6M HCl was evaporated off, and the samples were redissolved in 6M HCl. Mother solutions were prepared by adding 6M HCl and Milli-Q

water (total 30 ml) to the dissolved samples. Daughter solutions were prepared using 0.5 ml of mother solution, diluted to 5 ml with 3% HNO<sub>3</sub> (containing the internal standards 5 ppb In/ 5 ppb Re/ 20 ppb Be), resulting in an overall dilution factor of c. 4000.

Trace element analyses of the daughter samples were undertaken on the Thermo Scientific X Series 2 quadrupole inductively coupled plasma mass spectrometer (ICP-MS) at the University of Southampton. Samples and standards were spiked with internal standard elements and corrected for interferences and the blank and then calibrated using a suite of international rock standards. Accuracy was monitored using reference materials JA-2, BCR-2, JB-2 (see Supplementary Tables 1 and 2).

### ***Pb Isotopic Analysis***

For Pb isotope analysis, 0.3 g of cleaned, picked rock chips (0.5 mm to 1 mm) were weighed into Pb Savillex Teflon vials and leached on a hotplate with 4 ml 6M HCl for one hour (15 minutes for obsidian and pumice samples, to avoid full dissolution of the sample). Samples were rinsed several times in Milli-Q water, then 0.5 ml concentrated HNO<sub>3</sub>, before adding 3-4 ml of concentrated HF. Samples were digested, following the same procedure as for trace elements, and refluxed on a hotplate at 130 °C for 24 hours, before being evaporated to dryness. 0.5 ml concentrated HCl was added, and the sample evaporated to dryness. Then 0.5 ml concentrated HNO<sub>3</sub> was added and again evaporated to dryness. The final residue was reconstituted in 0.5 ml HBr and refluxed for an hour. The samples were cooled and centrifuged for 5 minutes. Pb was isolated using a single-stage HCl anion-exchange chromatographic resin separation method [58], with AGX-1x8, 200 – 400 mesh resin. Following this, the Pb isolate was dried down, redissolved in HNO<sub>3</sub>, and analysed using the double spike method of ref.[59]. The samples were subsequently analysed on a Thermo Scientific Neptune Multi-collector inductively coupled plasma mass spectrometer (MC-

ICPMS) at the University of Southampton (UK) achieving a NBS SRM 981 reproducibility of  $^{206}\text{Pb}/^{204}\text{Pb} = 16.9404 \pm 24$  (142 ppm),  $^{207}\text{Pb}/^{204}\text{Pb} = 15.4969 \pm 26$  (168 ppm),  $^{208}\text{Pb}/^{204}\text{Pb} = 36.7149 \pm 66$  (180 ppm) (2sd; n=44). Pb isotope measurements of the standard are within error of the accepted values ( $^{206}\text{Pb}/^{204}\text{Pb} = 16.9412$ ,  $^{207}\text{Pb}/^{204}\text{Pb} = 15.4988$ ,  $^{208}\text{Pb}/^{204}\text{Pb} = 36.7233$ ). Accuracy was 47 ppm for  $^{206}\text{Pb}/^{204}\text{Pb}$ , 123 ppm for  $^{207}\text{Pb}/^{204}\text{Pb}$ , and 174 ppm for  $^{208}\text{Pb}/^{204}\text{Pb}$ .

### *$^{143}\text{Nd}/^{144}\text{Nd}$ and $^{87}\text{Sr}/^{86}\text{Sr}$ Isotopic Analysis*

For Sr and Nd analysis, the remaining mother solutions from the preparation of trace element solutions (see above) were used for all samples except those of the BBVC. An aliquot of each mother solution was used, to give a volume of liquid containing at least 1  $\mu\text{g}$  Sr and 200 ng Nd and evaporated to dryness in Savillex Teflon vials on a hotplate at 130°C. Sample residues were reconstituted in 200  $\mu\text{l}$  1.75M HCl. For the BBVC samples, rock chips were leached in 4 ml 6M HCl or 30 minutes in Savillex Teflon vials (obsidian samples for only 15 minutes, to avoid full dissolution of the sample). The samples were then rinsed with Milli-Q water and  $\text{HNO}_3$ , and then the same digestion procedure as for trace element analysis (above) was followed. The final mother solutions were prepared using HCl and Milli-Q water to 30 ml for felsic samples and 20 ml for mafic samples.

All samples were then passed through ion exchange column chemistry, using a AG50-X8 200-400 mesh resin cation column to separate the Sr and Nd fractions. The sample fractions were subsequently evaporated to dryness, ready for further column chemistry.

Sr was further isolated through Sr-spec resin columns, following the methodology of ref.[60]. Samples were then evaporated to dryness, dissolved in 1.5 ml 1M HCl and loaded onto outgassed tantalum filaments with 1  $\mu\text{l}$  of Ta-activator. Sr isotopic analysis was performed on a Thermal Ionisation Mass Spectrometer (TIMS) Thermo Scientific Triton Plus at the

University of Southampton. Reference material SRM NIST987 ( $^{87}\text{Sr}/^{86}\text{Sr} = 0.710258$ ; GeoREM) was used to monitor accuracy and gave average  $^{87}\text{Sr}/^{86}\text{Sr}$  values of 0.710243. All samples were normalised to NBS SRM-987  $^{87}\text{Sr}/^{86}\text{Sr} = 0.710248$  [61], while reproducibility was  $\pm 0.000020$  (28.2 ppm, 2sd;  $n=464$ ). Accuracy was 21 ppm.

The Nd aliquot from the cation column was followed by an Ln-spec resin (50-100  $\mu\text{m}$ ) [60]. The samples were then evaporated to dryness and 3%  $\text{HNO}_3$  was added to produce a solution of 50 ppb.  $^{143}\text{Nd}/^{144}\text{Nd}$  analyses were undertaken on the ThermoScientific Neptune multi-collector inductively coupled plasma mass spectrometer (MC-ICP-MS) at the University of Southampton. Corrected Nd isotopic compositions were obtained using a method based on ref.[62] through adjustment to a  $^{146}\text{Nd}/^{144}\text{Nd}$  ratio of 0.7219 and a secondary normalisation to  $^{142}\text{Nd}/^{144}\text{Nd} = 1.141876$ . Reference material JNdi-1 was measured as an unknown ( $^{143}\text{Nd}/^{144}\text{Nd}$  of 0.512124, 2sd; [63]) achieving an average  $^{143}\text{Nd}/^{144}\text{Nd}$  of 0.512115 with an external reproducibility of  $\pm 0.000008$  (2sd, 15.2 ppm) across 6 analysis sessions over 2 years. The total column blanks (i.e., when blank acid is run through the column procedure) were negligible ( $<20$  pg) compared to the total amounts analysed (1  $\mu\text{g}$  and 200  $\mu\text{g}$ ) for Sr and Nd, respectively.

### ***Shear Velocity Mapping from Joint Inversion***

We use the shear wave velocity model of ref.[30] for inclusion in our analysis. The 3D velocity model is created through a joint inversion of Rayleigh-wave phase-velocities from ambient noise and teleseisms [30, 33]. The shear velocity model is parameterised every 5 km vertically with  $0.1^\circ \times 0.1^\circ$  pixel size for the upper 50 km. For deeper depths, an irregular spacing was used, increasing from 10 – 50 km spacings to match that of ref.[39]. For further details on the creation of the velocity model, the reader is directed to refs.[30, 33] and references therein.



For the analysis in this paper, the shear velocity model was interpolated to 1 km depth using a linear interpolation; we then extracted 1D columns of velocity with depth at the same resolution as our pixel size ( $0.1^\circ \times 0.1^\circ$ ).

### ***Moho Depths***

The gridded Moho depth map was produced from the Vs maps of ref.[33], described above. The Vs model was interpolated to a vertical grid spacing of 1 km. A velocity slice at the 3.75 km/s contour was extracted, which mapped best to previous receiver function measurements [65-69], active source experiments (e.g., ref.[70]) and previous S-wave models (e.g., ref.[71]).

### ***Statistical Models Considered***

As described in the text, five models were considered (see Extended Data Table 2), with each model being tested using a linear fit and a spline fit (Fig. 3). We note that a spline fit to itself can be linear if that is the best-fitting line.

Empirical models are estimated for the variation of each of 14 geochemical quantities (each of which is represented generically by random variable  $Y$ ) as a function of distance  $d \in [0, 1800]$  km for the five different models. Models are specified that explore the variation of  $Y$  with  $d$  in increasing complexity. The simplest model (C1C) assumes the existence of a single upwelling centre (at  $11.192^\circ\text{N}$   $41.784^\circ\text{E}$ ; see Figs. 1 & 3), with respect to which  $d$  is defined for all three rifts. The variation of  $Y$  with  $d$  is assumed common to all rifts. Model C3C assumes the existence of three upwelling centres (at  $11.192^\circ\text{N}$   $41.784^\circ\text{E}$ ,  $14.008^\circ\text{N}$   $40.458^\circ\text{E}$  &  $6.626^\circ\text{N}$   $37.948^\circ\text{E}$ ; see Fig. 1) based on ref.[37]; observations are allocated to the nearest upwelling centre, facilitating calculation of a single  $d$  for each observation. Like model C1C, the variation of  $Y$  with  $d$  is assumed common to all rifts, regardless of upwelling allocation. Model C1D assumes one upwelling centre (like C1C) for calculation of  $d$ , but now

the variation of  $Y$  with  $d$  is assumed to be different across rifts. Model C3D duplicates C3C for estimation of  $d$ , but variation of  $Y$  with  $d$  is assumed to be different across rifts. Finally, in model C3X, we consider the presence of three upwelling centres, with different variation of  $Y$  with  $d$  for each combination of upwelling and rift.

### ***Data Pre-Processing***

For models C1C and C1D, the distance between each sample and the upwelling locus centred on Lake Abhe (11.192170 °N, 41.783750 °E) is calculated. For models C3C, C3D and C3X, the distance between each sample and each of the three upwelling locations (Figs. 1 & 3) is measured, and then each sample is assigned to its nearest upwelling centre. The distance ( $d$ ) between two locations (i.e., upwelling and sample) is calculated using the spherical cosine law:

$$d = R(\cos^{-1}(\cos(a)\cos(b) + \sin(a)\sin(b)\cos(C))) \quad (\text{Eq. 5})$$

where  $a$  is the angle (in radians) from the North Pole to the sample location,  $b$  is the angle (in radians) from the North Pole to the upwelling location,  $C$  is the difference in radians between the longitude values of the sample and upwelling, and  $R$  is the radius of the earth in metres ( $6371 \times 10^3$ ).

### ***Penalised B-splines***

For each model, the variation of  $Y$  with  $d$  is described using a penalised B-spline (e.g., refs.[72-73]), the characteristics of which are selected to provide optimal predictive performance. First, for a large index set of locations equally spaced on the domain of distance, we calculate a B-spline basis matrix,  $B$  (e.g., ref.[74]) consisting of  $p$  equally spaced cubic spline basis functions. Then the value of  $Y$  on the index set is given by the vector  $B\beta$ , for spline coefficient vector  $\beta$  to be estimated. The value of  $p$  is specified to be sufficiently large to provide a good description of a highly variable  $Y$ . For a given data set, we penalise

the difference between consecutive values in  $\beta$  using a roughness penalty, such that the penalised spline exhibits optimal roughness, providing optimal predictive performance.

### *Estimating Optimal Spline Roughness and Predictive Performance*

For a sample of  $n_1$  training data, consisting of vectors of geochemical and geophysical quantities ( $y_1$ ) and distances ( $d_1$ ), we first allocate each element of  $d_1$  to its nearest neighbour in the index set, and hence construct the appropriate spline basis matrix  $B_1$  for the sample. We then assume that  $y_1 = B_1\beta + \varepsilon$ , where the elements of  $\varepsilon$  are independently and identically distributed zero-mean Gaussian random variables. We penalise the roughness of  $\beta$  using a first-difference penalty  $\lambda\beta'P\beta$ , where  $P = D'D$  and  $D$  is a first difference matrix (with elements  $D_{ij} = -1$  if  $i = j$ ;  $= 1$  if  $j = i + 1$ ; and  $= 0$  otherwise (e.g., ref.[75]). For a given choice of  $\lambda$ , we then find the optimal value of  $\beta$  by minimising lack of fit:

$$\beta^*(\lambda) = \underset{\beta}{\operatorname{argmin}} \{ (y_1 - B_1\beta)'(y_1 - B_1\beta) + \lambda\beta'P\beta \} \quad (\text{Eq. 6})$$

$$= (B_1'B_1 + \lambda P)^{-1} B_1'y_1 \quad (\text{Eq. 7})$$

We can evaluate the predictive performance of the resulting spline description using a tuning set of  $n_2$  observations (independent of the training set) represented by vectors  $y_2$  and  $d_2$ . We again start by finding the appropriate spline basis matrix  $B_2$  for this sample. Then we can calculate the predictive mean square error for the tuning sample:

$$\text{MSE}_{Tune}(\lambda) = \frac{1}{n_2} (y_2 - B_2\beta^*(\lambda))'(y_2 - B_2\beta^*(\lambda)) \quad (\text{Eq. 8})$$

for each of a set of representative choices of values for  $\lambda$ . We can then select the optimal value of  $\lambda$  using

$$\lambda^* = \underset{\lambda}{\operatorname{argmin}} \{ \text{MSE}_{Tune}(\lambda) \} \quad (\text{Eq. 9})$$

The value  $MSE_{Tune}(\lambda^*)$  is a biased estimate of predictive performance since the value of  $\lambda^*$  was tuned to minimise its value. We can obtain an unbiased estimate for the predictive performance of the spline model using a test set of  $n_3$  observations (independent of the training and tuning sets) represented by vectors  $y_3$  and  $d_3$  (and corresponding spline basis matrix  $B_3$ ). Then the predictive performance is estimated using:

$$MSE_{Test} = \frac{1}{n_3} (y_3 - B_3 \beta^*(\lambda^*))' (y_3 - B_3 \beta^*(\lambda^*)) \quad (\text{Eq. 10})$$

### ***Cross-Validation and Model Comparison***

We exploit cross-validation to evaluate  $MSE_{Test}$ , by partitioning the full sample of data into  $k > 2$  groups at random, withholding one group for tuning, another group for testing, and retaining the remaining  $k - 2$  groups for training. We then loop exhaustively over all possible combinations of choice of train, tune, and test groups, evaluating overall predictive performance on the test data over all iterations, noting that each observation occurs exactly once in the test set. For models requiring separate model fits to subsets of data (that is, C1D, C3D, C3X),  $MSE_{Test}$  is estimated using predictions from optimal predictive models for each subset. Further, we can repeat the analysis for different initial random partitioning of observations into  $k$  groups, to assess the sensitivity of overall predictive performance to this choice. We are careful to use the same cross-validation partitions to evaluate each of the five models, so that predictive performances can be compared fairly.

To quantify model performance over all 13 geochemical quantities ( $j = 1, 2, \dots, 13$ ), we define the overall standardised  $MSE_{Test}$

$$SMSE = \sum_{j=1}^{13} \frac{MSE_{Test,j}}{s_j^2} \quad (\text{Eq. 11})$$

where  $MSE_{Test,j}$  is the predictive performance for the  $j$ th geochemical indicator, and  $s_j^2$  is the sample estimate for the variance of that quantity. The estimation of the splines and the testing

of their predictive performance was repeated over 100 iterations. Results from each iteration and the mean of the SMSE is shown in Fig. 4.

### ***Linear Regression***

For comparison, we also evaluate linear regression models for the variation of  $Y$  with  $d$ . In the current notation, these can be thought of as simple models with basis matrix  $B = [1 \ d]$ , where  $1$  is a vector of appropriate length with each element  $= 1$ .  $B$  in this case is a 2-vector with elements corresponding to intercept and slope coefficients. Linear regression is approached using penalised B-spline models as the roughness coefficient  $\lambda \rightarrow \infty$ . That is, linear regression corresponds to a penalised B-spline model with very large  $\lambda$ . Therefore, a penalised B-spline model is guaranteed to perform at least as well as linear regression.

### ***Uncertainty of Model Performance***

To explore the effect of uncertainty on model performance, a perturbation analysis was undertaken. This analysis required the generation and modelling of  $n_{pert}$  new data samples. Each of these data samples corresponded to a perturbation of the original data sample. A value of  $n_{pert} = 300$  was selected to ensure that 95% uncertainty bands for predictive performance on perturbed data could be estimated with confidence.

In perturbed sample  $q$ ,  $q = 1, 2, \dots, n_{pert}$ , the value  $y_{ijq}^*$  of the  $i$ th observation for variable  $j$  was obtained by perturbing the corresponding value  $y_{ij}$  in the original data sample, using additive Gaussian noise  $e_{ijq}$ , the standard deviation  $\sigma_{ij}$  of which was informed by the known value of measurement uncertainty for that observation of the variable. Mathematically:

$$y_{ijq}^* = y_{ij} + e_{ijq} \quad (\text{Eq. 12})$$

The complete modelling procedure was then applied to each perturbed data sample in turn.

The predictive performance of different models was assessed over the  $n_{pert}$  perturbations, as

illustrated in Fig. 4, in terms of 95% uncertainty bands. The figure indicates that model C1D provides best predictive performance on perturbed data, as well as for the original unperturbed sample. Note that, since noise has been added to observations in the perturbation analysis, the overall performance of models on perturbed data is poorer than on the original sample, as expected.

### ***Testing the Influence of Crustal Assimilation***

We tested the influence of crustal assimilation further by excluding cases where Ce/Pb values fall below 20 and which could feasibly be associated with crustal assimilation [26, 34]. Using additional analysis, we confirm that excluding cases in which  $Ce/Pb < 20$  does not affect our overall results (see Extended Data Fig. 3a), suggesting that primary mantle compositional fluctuations (i.e., relative proportions of compositional mantle endmembers) exert the first-order control on eruptive compositions at the surface.

### ***Principal Component Analysis***

Principal component analysis (PCA) requires each sample or object to have the same number of values for each variable and so the dataset was reduced to 94 samples. PCA is only carried out on radiogenic isotope compositions of the samples where data are available for the mantle endmembers investigated (i.e., Afar plume, Pan-African Lithosphere, Depleted Mantle, Enriched Mantle 1, Enriched Mantle 2, HiMU; Fig. 5; Extended Data Table 3). While other purely geochemical studies on Afar (e.g., refs.[14, 38]) have included sub-crustal components such as the sub continental lithospheric mantle (SCLM), we decided not to include this endmember as it can sometimes be indistinguishable from certain mantle endmembers (i.e., EM1), especially in cases where the SCLM is metasomatized. Values used for the endmembers in our models are provided in Extended Data Table 3. Each object is standardised before being included in the PCA:

$$y_{stdj} = \frac{y_j - \bar{y}_j}{\sigma_j} \quad (\text{Eq. 13})$$

where  $\bar{y}_j$  is the mean of variable  $j$ , and  $\sigma_j$  is the standard deviation of the variable  $j$ :

$$\sigma_j = \sqrt{\frac{\sum \{(y_j - \bar{y}_j)\}^2}{N_j}} \quad (\text{Eq. 14})$$

where  $N_j$  is the number of objects within variable  $j$ .

Approximately 90.5% of the variance is explained within the plane of the first two eigenvectors, increasing to 95.5% when including the third eigenvector. The first principal component (PC-1) is most influenced by  $^{207}\text{Pb}/^{204}\text{Pb}$ ,  $^{208}\text{Pb}/^{204}\text{Pb}$ , whereas the second principal component (PC-2) is dominantly influenced by  $^{206}\text{Pb}/^{204}\text{Pb}$  and  $^{87}\text{Sr}/^{86}\text{Sr}$ . The third principal component (PC-3) is dominated by  $^{207}\text{Pb}/^{204}\text{Pb}$  and  $^{143}\text{Nd}/^{144}\text{Nd}$  (Supplementary Table 3).

#### ***K-means Cluster Analysis***

K-means cluster analysis [76] was carried out on the samples using the 13 standardised variables (Extended Data Table 1). The K-means algorithm assigns each object to a singular cluster that does not overlap with another (i.e., partitional clustering), minimising the total sum of squared error (SSE) from the centre point of each cluster, known as the centroid, to each data point.

To find the optimum number of clusters ( $k$ )—which reduces the within-cluster total sum of squares error with the lowest number of clusters—we run the K-means algorithm specifying  $k$  to be 1:20, over 1000 iterations for each  $k$  (Supplementary Fig. 1). We then select eight clusters based on  $k=8$ , reducing the within-cluster total sum of squares by 75% from  $k=1$ , and the range over the 1,000 iterations being minimised when  $k \geq 8$ . The cluster assignments for each object, out of the 1,000 iterations, are selected by finding the iteration number that is

closest to the mean within-cluster total sum of squares of that  $k$  value (shown by the blue line in Supplementary Fig. 1).

### **Data Availability**

The datasets analysed for the current project are available as Supplementary Material. Some data were obtained from GeoROC [19,32,51]; these data are clearly marked in the datafile.

The data is freely available on FigShare at <https://doi.org/10.6084/m9.figshare.28769105> (ref 83)

### **Code Availability**

The input data, code and output within this study is openly available and can be found at <https://github.com/ygraigarw/AfarPlume.git> (ref. 84)

### **Methods-only References**

[51] Watts, E. J., Gernon, T. M., Taylor, R. N., Keir, D., & Pagli, C. (2023). Magmatic evolution during proto-oceanic rifting at Alu, Dalafilla and Borale Volcanoes (Afar) determined by trace element and Sr-Nd-Pb isotope geochemistry. *Lithos*, 456, 107311. <https://doi.org/10.1016/j.lithos.2023.107311>

[52] Watts, E. J., Gernon, T. M., Taylor, R. N., Keir, D., Siegburg, M., Jarman, J., ... & Gioncada, A. (2020). Evolution of the Alu-Dalafilla and Borale volcanoes, Afar, Ethiopia. *Journal of Volcanology and Geothermal Research*, 408, 107094. <https://doi.org/10.1016/j.jvolgeores.2020.107094>

[53] Rees, R., Gernon, T. M., Keir, D., Taylor, R. N., & Pagli, C. (2023). The spatial and volcanic evolution of Ayelu, Abida and Yangudi volcanoes in the Northern Main Ethiopian Rift–Southern Afar, Ethiopia. *Journal of Volcanology and Geothermal Research*, 440, 107846. <https://doi.org/10.1016/j.jvolgeores.2023.107846>



- 819 [54] Barberi, F., & Varet, J. (1970). The Erta Ale volcanic range (Danakil depression,  
820 northern afar, ethiopia). *Bulletin Volcanologique*, 34, 848-917.  
821 <https://doi.org/10.1007/BF02596805>
- 822 [55] Siegburg, M. (2019). Evolution of faulting and magmatism during volcanic rifting in the  
823 Ethiopian Rift: A case study of the Boset-Bericha Volcanic Complex (Doctoral dissertation,  
824 University of Southampton).
- 825 [56] Siegburg, M., Gernon, T. M., Bull, J. M., Keir, D., Barfod, D. N., Taylor, R. N., ... &  
826 Ayele, A. (2018). Geological evolution of the Boset-Bericha volcanic complex, Main  
827 Ethiopian Rift:  $^{40}\text{Ar}/^{39}\text{Ar}$  evidence for episodic Pleistocene to Holocene volcanism. *Journal of*  
828 *Volcanology and Geothermal Research*, 351, 115-133.  
829 <https://doi.org/10.1016/j.jvolgeores.2017.12.014>
- 830 [57] Siegburg, M., Gernon, T. M., Keir, D., Bull, J. M., Taylor, R. N., Watts, E. J., ... &  
831 Gebru, E. F. (2023). Temporal clustering of fissural eruption across multiple segments within  
832 the Ethiopian Rift. *Frontiers in Earth Science*, 11, 1169635.  
833 <https://doi.org/10.3389/feart.2023.1169635>
- 834 [58] Kamber, B. S., & Gladu, A. H. (2009). Comparison of Pb purification by anion-  
835 exchange resin methods and assessment of long-term reproducibility of Th/U/Pb ratio  
836 measurements by quadrupole ICP-MS. *Geostandards and Geoanalytical Research*, 33(2),  
837 169-181. <https://doi.org/10.1111/J.1751-908X.2009.00911.X>
- 838 [59] Taylor, R. N., Ishizuka, O., Michalik, A., Milton, J. A., & Croudace, I. W. (2015).  
839 Evaluating the precision of Pb isotope measurement by mass spectrometry. *Journal of*  
840 *Analytical Atomic Spectrometry*, 30(1), 198-213. <https://doi.org/10.1039/c4ja00279b>
- 841 [60] Pin, C., Briot, D., Bassin, C., & Poitrasson, F. (1994). Concomitant separation of  
842 strontium and samarium-neodymium for isotopic analysis in silicate samples, based on

- specific extraction chromatography. *Analytica Chimica Acta*, 298(2), 209-217.  
[https://doi.org/10.1016/0003-2670\(94\)00274-6](https://doi.org/10.1016/0003-2670(94)00274-6)
- [61] Thirlwall, M. F. (1991). Long-term reproducibility of multicollector Sr and Nd isotope ratio analysis. *Chemical Geology: Isotope Geoscience section*, 94(2), 85-104.  
[https://doi.org/10.1016/0168-9622\(91\)90002-E](https://doi.org/10.1016/0168-9622(91)90002-E)
- [62] Pin, C., & Zalduegui, J. S. (1997). Sequential separation of light rare-earth elements, thorium, and uranium by miniaturized extraction chromatography: application to isotopic analyses of silicate rocks. *Analytica Chimica Acta*, 339(1-2), 79-89.  
[https://doi.org/10.1016/S0003-2670\(96\)00499-0](https://doi.org/10.1016/S0003-2670(96)00499-0)
- [63] Vance, D., & Thirlwall, M. (2002). An assessment of mass discrimination in MC-ICPMS using Nd isotopes. *Chemical Geology*, 185(3-4), 227-240.  
[https://doi.org/10.1016/S0009-2541\(01\)00402-8](https://doi.org/10.1016/S0009-2541(01)00402-8)
- [64] Tanaka, T., Togashi, S., Kamioka, H., Amakawa, H., Kagami, H., Hamamoto, T., ... & Dragusanu, C. (2000). JNdi-1: a neodymium isotopic reference in consistency with LaJolla neodymium. *Chemical Geology*, 168(3-4), 279-281. [https://doi.org/10.1016/S0009-2541\(00\)00198-4](https://doi.org/10.1016/S0009-2541(00)00198-4)
- [65] Hammond, J. O., Kendall, J. M., Stuart, G. W., Keir, D., Ebinger, C., Ayele, A., & Belachew, M. (2011). The nature of the crust beneath the Afar triple junction: Evidence from receiver functions. *Geochemistry, Geophysics, Geosystems*, 12(12).  
<https://doi.org/10.1029/2011GC003738>
- [66] Ayele, A., Stuart, G., & Kendall, J. M. (2004). Insights into rifting from shear wave splitting and receiver functions: An example from Ethiopia. *Geophysical Journal International*, 157(1), 354-362. <https://doi.org/10.1111/j.1365-246X.2004.02206.x>

- [67] Dugda, M. T., Nyblade, A. A., Julia, J., Langston, C. A., Ammon, C. J., & Simiyu, S. (2005). Crustal structure in Ethiopia and Kenya from receiver function analysis: Implications for rift development in eastern Africa. *Journal of Geophysical Research: Solid Earth*, 110(B1). <https://doi.org/10.1029/2004JB003065>
- [68] Ogden, C. S., Bastow, I. D., Gilligan, A., & Rondenay, S. (2019). A reappraisal of the H- $\kappa$  stacking technique: implications for global crustal structure. *Geophysical Journal International*, 219(3), 1491-1513. <https://doi.org/10.1093/gji/ggz364>
- [69] Stuart, G. W., Bastow, I. D., & Ebinger, C. J. (2006). Crustal structure of the northern Main Ethiopian Rift from receiver function studies. *Geological Society, London, Special Publications*, 259(1), 253-267. <https://doi.org/10.1144/GSL.SP.2006.259.01.20>
- [70] Maguire, P. K. H., Keller, G. R., Klemperer, S. L., Mackenzie, G. D., Keranen, K., Harder, S., ... & Amha, M. (2006). Crustal structure of the northern Main Ethiopian Rift from the EAGLE controlled-source survey; a snapshot of incipient lithospheric break-up. *Geological Society, London, Special Publications*, 259(1), 269-292. <https://doi.org/10.1144/GSL.SP.2006.259.01.21>
- [71] Keranen, K. M., Klemperer, S. L., Julia, J., Lawrence, J. F., & Nyblade, A. A. (2009). Low lower crustal velocity across Ethiopia: Is the Main Ethiopian Rift a narrow rift in a hot craton?. *Geochemistry, Geophysics, Geosystems*, 10(5). <https://doi.org/10.1029/2008GC002293>
- [72] Eilers, P. H., & Marx, B. D. (1996). Flexible smoothing with B-splines and penalties. *Statistical science*, 11(2), 89-121. <https://doi.org/10.1214/ss/1038425655>
- [73] Eilers, P. H., & Marx, B. D. (2010). *Splines, knots, and penalties*. Wiley Interdisciplinary Reviews: Computational Statistics, 2(6), 637-653. <https://doi.org/10.1002/wics.125>

- 890 [74] De Boor, C., (1978). A practical guide to splines Vol. 27 Springer-verlag. New York.  
 891 <https://doi.org/10.1007/978-1-4612-6333-3>
- 892 [75] Jones, M., Randell, D., Ewans, K., & Jonathan, P. (2016). Statistics of extreme ocean  
 893 environments: Non-stationary inference for directionality and other covariate effects. Ocean  
 894 Engineering, 119, 30-46. <https://doi.org/10.1016/j.oceaneng.2016.04.010>
- 895 [76] Arthur, D., & Vassilvitskii, S. (2007). k-means++: The advantages of careful seeding. In  
 896 Soda (Vol. 7, pp. 1027-1035).<https://doi.org/10.5555/1283383>
- 897 [77] Stracke, A., Hofmann, A. W., & Hart, S. R. (2005). FOZO, HIMU, and the rest of the  
 898 mantle zoo. Geochemistry, Geophysics, Geosystems, 6(5).  
 899 <https://doi.org/10.1029/2004GC000824>
- 900 [78] McDonough, W. F., & Sun, S. S. (1995). The composition of the Earth. Chemical  
 901 Geology, 120(3-4), 223-253. [https://doi.org/10.1016/0009-2541\(94\)00140-4](https://doi.org/10.1016/0009-2541(94)00140-4)
- 902 [79] Zindler, A., & Hart, S. (1986). Chemical geodynamics. IN: Annual review of earth and  
 903 planetary sciences. Volume 14 (A87-13190 03-46). Palo Alto, CA, Annual Reviews, Inc.,  
 904 1986, p. 493-571., 14, 493-571. <https://doi.org/10.1146/annurev.ea.14.050186.002425>
- 905 [80] Rollinson, H. R., Rollinson, H., & Pease, V. (2021). Using geochemical data: to  
 906 understand geological processes. Cambridge University Press.  
 907 <https://doi.org/10.1017/9781108777834>
- 908 [81] Jochum, K. P., Willbold, M., Raczek, I., Stoll, B., & Herwig, K. (2005). Chemical  
 909 Characterisation of the USGS Reference Glasses GSA-1G, GSC-1G, GSD-1G, GSE-1G,  
 910 BCR-2G, BHVO-2G and BIR-1G Using EPMA, ID-TIMS, ID-ICP-MS and LA-ICP-MS.  
 911 Geostandards and Geoanalytical Research, 29(3), 285-302. [https://doi.org/10.1111/j.1751-](https://doi.org/10.1111/j.1751-908X.2005.tb00901.x)  
 912 [908X.2005.tb00901.x](https://doi.org/10.1111/j.1751-908X.2005.tb00901.x)

- 913 [82] Hart, S. R. (1988). Heterogeneous mantle domains: signatures, genesis and mixing  
 914 chronologies. *Earth and Planetary Science Letters*, 90(3), 273-296.  
 915 [https://doi.org/10.1016/0012-821X\(88\)90131-8](https://doi.org/10.1016/0012-821X(88)90131-8)
- 916 [83] Watts et al.. (2025). Dataset for Mantle upwelling at Afar triple junction shaped by  
 917 overriding plate dynamics. FigShare <https://doi.org/10.6084/m9.figshare.28769105>
- 918 [84] Watts et al.. (2025). MATLAB software for Mantle upwelling at Afar triple junction  
 919 shaped by overriding plate dynamics. GitHub <https://github.com/ygraigarw/AfarPlume.git>

# **Mantle upwelling at Afar triple junction shaped by overriding plate dynamics**

Emma J. Watts<sup>1,2\*</sup>, Rhiannon Rees<sup>1</sup>, Philip Jonathan<sup>3,4</sup>, Derek Keir<sup>1,5</sup>, Rex N. Taylor<sup>1</sup>, Melanie Siegburg<sup>6</sup>, Emma L. Chambers<sup>7</sup>, Carolina Pagli<sup>8</sup>, Matthew J. Cooper<sup>1</sup>, Agnes Michalik<sup>1</sup>, J. Andrew Milton<sup>1</sup>, Thea K. Hincks<sup>1</sup>, Ermias F. Gebru<sup>9,10</sup>, Atalay Ayele<sup>10</sup>, Bekele Abebe<sup>10</sup>, Thomas M. Gernon<sup>1, 11</sup>

<sup>1</sup>School of Ocean and Earth Science, University of Southampton, National Oceanography Centre, European Way, Southampton, SO14 3ZH, UK

<sup>2</sup> Now at: Geography Department, Swansea University, Singleton Park, Sketty, Swansea SA2 8PP

<sup>3</sup>Department of Mathematics and Statistics, Lancaster University, Lancaster, UK

<sup>4</sup>Shell Research Limited, London, UK

<sup>5</sup> Dipartimento di Scienze della Terra, Università degli Studi di Firenze, Firenze 50121, Italy

<sup>6</sup> GEOMAR Helmholtz Centre for Ocean Research Kiel, Kiel, Germany

<sup>7</sup> School of Cosmic Physics, Geophysics Section, Dublin Institute for Advanced Studies, Dublin, Ireland

<sup>8</sup> Dipartimento di Scienze della Terra, Università di Pisa, Pisa 56126, Italy

<sup>9</sup>Department of Geosciences, University of Fribourg, Fribourg, Switzerland

<sup>10</sup>School of Earth Sciences, Addis Ababa University, Addis Ababa, Ethiopia

<sup>11</sup>GFZ Helmholtz Centre for Geosciences, Telegrafenberg, 14473 Potsdam, Germany

\*Corresponding Author Email: [e.j.watts@swansea.ac.uk](mailto:e.j.watts@swansea.ac.uk)

**Mantle upwellings drive large-scale surface volcanism and facilitate continental breakup and ocean basin formation. However, the spatial characteristics and internal composition of these upwellings and how they are modified by plate tectonics are poorly resolved. Afar, East Africa, is a classic triple junction comprising three rifts at various stages of evolution**

thought to be underlain by a mantle upwelling or plume, allowing examination of the controls on the mantle upwelling. Here, we present geochemical data from >130 samples of “young” volcanoes spanning the triple junction to show that the underlying mantle comprises a single, asymmetric upwelling. Using statistical modelling to integrate our data with existing geochemical and geophysical constraints, we suggest that Afar is fed by a spatially and chemically heterogeneous upwelling, which controls the composition and relative abundance of melt in all three rift arms. We identify repetitive signatures in mantle compositions in rift regions, whose variability is a longer wavelength in faster-extending rift arms. This suggests more rapid channelised mantle flow occurs where rifting rates are higher and the plate is thinner, aiding flow of the upwelling towards the faster spreading Red Sea Rift. Our findings demonstrate how the evolution of mantle upwellings are influenced by the dynamics of overriding plates.

The role of mantle upwellings, sometimes interpreted as mantle plumes, in driving volcanism during continental breakup has long been debated (e.g. [1-4]). Moreover, our understanding of rift-plume interactions remains incomplete because only a small fraction of Earth’s upwellings are situated under continents [5] and there are a limited number of upwellings associated with ongoing continental rifting [6]. The Afar triple junction—where the Arabian, Nubian, and Somalian tectonic plates intersect—is a “classic” example of magma-assisted continental rifting. Here, rifting occurred diachronously with the onset of the Gulf of Aden Rift (GoA) at ~35 Ma [7], the Red Sea Rift (RSR) at ~23 Ma [8] and the Main Ethiopian Rift (MER) at ~11 Ma [9]. Both intraplate stresses tied to the slab pull effect of Neo-Tethys subduction [10], and thermal weakening by a mantle upwelling, are thought to have driven rifting [11]. The diachronous onset has led to each rift (GoA, RSR and MER) being in a different phase of maturity (that is, ocean formation, proto-oceanic formation, and mature continental rifting, respectively), and all three rifts are currently volcanically and tectonically active [12], making

it an ideal location to study the interactions between mantle upwelling and rifting, and how these coevolve.

The driver of melt production in Afar is debated, with some models suggesting decompression melting with minimal plume involvement [13], whereas others propose the upwelling of hot, deep mantle [14-17], or indeed multiple upwellings [18, 19]. Whilst several discrete segments of the RSR have been studied in terms of magma petrogenesis (e.g., [16, 20]), a paucity of high-precision geochemical data has hampered evaluation of the spatial characteristics of upwelling across the broader region and rigorously test existing models of the links between tectonics and upwellings.

Here, we implement a comprehensive sampling strategy, targeting evolutionarily young volcanoes spanning the three rifts (Fig. 1). We analyse rocks that are Quaternary in age (i.e., less than 2.58 million years (Myr) old), and from volcanoes that have been active during the Holocene, which began 11.7 thousand years ago (ka) [21]. By targeting younger rocks, we make a direct comparison with geophysical data across the region, enabling an integrated exploration of mantle petrogenesis and dynamics. Our approach utilises statistical methods including semi-parametric regression using splines and K-means cluster analysis to integrate and analyse these geophysical and geochemical data to explore models of upwelling that can explain our data.

## **Characteristics of Mantle Upwellings**

Mantle upwellings that originate between depths of 1,000 and 2,800 km are anomalously hot zones and/or zones of an enriched composition that reduce the solidus temperature of the mantle, enabling increased partial melting [22]. Mantle upwellings are widely accepted to contain a variety of domains of differing proportions (e.g., HIMU, EMI, EMII, C and FOZO [e.g., 5, 22-25]). Such domains typically exhibit an isotopically distinct and enriched



composition (that is, generally low  $^{87}\text{Sr}/^{86}\text{Sr}$ , high  $^{143}\text{Nd}/^{144}\text{Nd}$ , and high  $^{206}\text{Pb}/^{204}\text{Pb}$  [24]) relative to those of bulk silicate Earth (BSE [5]). Trace element ratios such as Ce/Pb and  $\Delta\text{Nb}$  have previously been used to indicate enriched upwellings ( $> 30$  [26],  $>0$  [27] respectively), and La/Sm to suggest the melt fraction relative to the study region with a lower-than-average value suggesting an elevated melt fraction [19]. Mantle upwellings are also commonly associated with reduced (i.e., lower) seismic velocities (i.e., S waves [ $V_s$ ] and P waves [ $V_p$ ]) [28, 29] that are caused by elevated temperatures and/or the presence of fluids and partial melt [30].

Crustal assimilation, where crust components are incorporated into the magma, can obscure these geochemical indicators of a deep mantle plume. However, within the Afar region, crustal contamination has played a relatively minor role in recent magmatism [14] compared to earlier stages of rifting [14, 26], due to the thinning of the present-day crust and that it has been extensively intruded by mafic melts along the length of the rift axes. Seismicity analysis indicates that recent magmatic activity beneath the rift axes in Afar is transient [31] and, in turn, that magmas are unlikely to reside in crustal reservoirs for long enough to extensively assimilate crustal lithologies.

### **Probing the Presence of Mantle Upwelling(s) in Afar**

Our study includes over 130 rock samples, with many from previously unstudied volcanoes, roughly doubling the number of high-quality analyses from the area (Fig. 1). The 79 Afar samples included in our study were carefully selected from a repository covering the broader Afar region (see Methods for details). These were supplemented by 52 additional samples collected during fieldwork in the MER. To examine spatial trends in the geochemistry of surface volcanism, we analysed all samples for major and trace elements alongside radiogenic isotopes (Sr, Nd, Pb; see Methods). We also integrated data for 93 rock samples from the open-

source GEOROC data repository (<https://georoc.eu/> (ref.[32])); see Methods for selection criteria), as well as the classic GoA catalogue from ref.[19]. Additionally, we leverage recent spatial compilations of geophysical variables, such as the depth of the Mohorovičić Discontinuity (Moho) [31] (see Methods) and shear-wave velocities at regularly spaced depths (i.e., 40, 60, 80, 100, and 120 km [30]) across the region. These variables provide well-established proxies for the boundary between the crust and mantle, and for the presence and abundance of melt within the lithosphere and asthenosphere [30]. Collectively, this information allows us to infer details about the depth, compositional characteristics and relative abundance of partial melts distributed across all three rifts.

Based on these samples, we infer wide geochemical variability across the study region (Fig. 1). Delta Niobium ranges from -0.26 to 0.94 and La/Sm ratio ranges from 0.4 to 4.6. The radiogenic isotopes  $^{206}\text{Pb}/^{204}\text{Pb}$ ,  $^{207}\text{Pb}/^{204}\text{Pb}$ ,  $^{208}\text{Pb}/^{204}\text{Pb}$ ,  $^{87}\text{Sr}/^{86}\text{Sr}$  and  $^{143}\text{Nd}/^{144}\text{Nd}$  also display a large range (Fig. 2, Extended Data Table 1), with enrichments relative to BSE occurring in all three rifts. Local variability in these radiogenic isotopes is observed within some volcanoes, e.g., Boset Bericha; however, this variability is smaller than the regional range determined for Afar (Fig. 1).

Across the study region, the depth of the Moho varies, being shallowest in the RSR (~16 km) and deepest in the MER (31 km). Like the geochemical data, the shear-wave velocities ( $V_s$ ) at 40, 60, 80, 100 and 120 km depths show regional variability: 3.81-4.05, 4.06-4.17, 4.00-4.15, 3.97-4.10, 4.02-4.10, respectively (Extended Data Fig. 1). All rifts show zones of high and low  $V_s$  (relative to ref.[30]) in the mantle which vary laterally and in depth.

To evaluate the potential influence of crustal assimilation—considered minor in the Afar region [14]—on mantle composition and upwelling, we assess the correlation between key geochemical and geophysical indicators (Fig. 4a) and the depth to the Moho. The Moho, the

boundary between the crust and mantle, serves as a proxy for crustal thickness, which is widely thought to influence the degree of assimilation [26] (Methods). We found that most indicators, including Pb isotopes—a reliable indicator of crustal assimilation [34]—exhibit only a weak, but statistically significant, correlation with Moho depth (Fig. 4a). Further, Ce/Pb exhibits a strong negative correlation (i.e., Pearson correlation coefficient of -0.7), indicating that where the crust is thin, the Ce/Pb values are high, and vice versa. This trend can be attributed to minimal crustal assimilation across most of the Afar region, though the degree of assimilation increases as the crust thickens within the MER.

Overall, our dataset shows geochemical and geophysical variability across the study area, which are consistent with the presence of an upwelling across all three rifts. The spatial trends observed in all variables implicate an underlying complexity to the location of partial melts.

### **Models of the Afar Upwelling**

We used our data to test multiple conceptual models of mantle upwelling dynamics. The initial conceptual model we considered is a simple, homogeneous mantle upwelling at the triple junction (e.g., ref.[19]). This model expects variables (geochemical and geophysical) that indicate deep upwelling to change radially with distance from the upwelling centre (C1C – 1 centre, concentric; Fig. 3, Extended Data Table 2). Therefore, this model assumes that variables change linearly from the upwelling centre due to lateral spreading. Extending this model, we then allow the upwelling to be spatially and temporally heterogeneous, as reported for the Hawaiian [35] and Canary Island [36] volcanoes. This mechanism yields a similar pattern to the linear C1C model but accommodates compositional fluctuations over the radial distance corresponding to a chemically pulsed upwelling (Fig. 3). This model fits a single spline per parameter for all data against distance from the upwelling centre (spline C1C). The optimum spline allows for regional variations to be accounted for, whilst minimising noise (i.e., optimal

smoothing). This approach of both linear and spline fits is applied to all further models described in this section allowing for homogenous and heterogeneous upwelling(s), respectively. Note the starting composition of the upwelling is not constrained within the model parameters.

We additionally tested whether the spatial geochemical and geophysical variations observed (Fig. 1 and Extended Data Fig. 1) are best explained through the presence of three small-scale upwellings, which have been proposed based on geophysics and numerical models (e.g. ref.[37], C3C – 3 centres, concentric; Fig. 3; Extended Data Table 1). We tested this model using three upwellings: one centred on the triple junction, one in the northern RSR, and one in the southern MER, with the positions of these loci informed by previous models and observations (Methods). This model fits one linear/spline regression per variable (against distance) from the nearest upwelling centre and assumes that the upwellings are compositionally identical and from the same deep source.

It is plausible that the variable tectonic regime (e.g., extension rate, crustal thickness) between the three rifts [12] introduces further complexity to the geochemical and geophysical signals. Accordingly, we introduce three further models, C1D, C3D, and C3X (Fig. 3, Extended Data Table 2; Methods) to account for these regional differences. Models C1D (1 centre, different spreading) and C3D (3 centres, different spreading) consider one upwelling and three small-scale upwellings, respectively, while allowing for distinct distance-dependent patterns for each rift, thereby modelling the distribution of variables across each rift independently. Unlike the other models, C3X (3 independent centres, different spreading) allows each small-scale upwelling to have a distinct signature, as well as permitting an independent distribution along each rift (Methods).

### **Spatial Characteristics of Afar Mantle Upwelling**

To test these models (Fig 3, Extended Data Table 2), we identify 14 key geochemical and geophysical variables (for descriptions, see Extended Table 2) and calculate the distance, using the spherical cosine law (Methods), between the purported upwelling centre [15, 19, 38] and each observation site (Methods). We then apply two-deep cross validation (100 iterations) to find the optimum linear fit (that is, representing a homogeneous upwelling) and penalised B-spline fit (that is, representing a heterogeneous upwelling) to each of the variables, using all data points, over a radial distance of 500 km—the radial limit of samples considered within our study (Fig. 4b and Extended Data Fig. 2). The predictive performance of each fit is then assessed by calculating the mean standardised root-mean squared error of prediction (RMSEP), where a value of 1 indicates a lack of predictive capability, and 0 a perfect predictive ability (Fig. 4c).

For all models, we observe the B-spline fit (i.e., a class of polynomial function; Methods) to have the best predictive performance, compared to a linear fit (Fig. 4c). This indicates that a compositionally heterogeneous upwelling in Afar is most probable (Figs. 4b and 4c).

The analysis indicates that the overall best predictive model is the B-spline fit of model C1D, wherein a single, heterogeneous mantle upwelling is present, albeit with differing distributions of geochemical and geophysical variables between rift-arms (Fig. 3; Extended Data Table 2). This model yields a mean standardised RMSEP of 0.59 (Fig. 4c), lower than that of the other models. To further validate our results, we carried out sensitivity analysis, varying the geochemical and geophysical data about their known uncertainties (see Methods). The results confirm that model C1D remains the most accurate predictive model (Fig. 4c).

Whilst the RSR and MER have a high sample density, there is limited sample availability from the GoA due to poor access. When excluding the GoA from our analyses, the overall trend between the models remains effectively the same (Extended Data Fig. 3b). Although the Afar

rifts share a single, compositionally heterogeneous upwelling, they appear to behave independently, implying that some feature of their tectonic regime modulates the observed signals.

## **Interplay Between Upwelling and Segmentation**

Many of the optimum splines for each rift display distance-dependent sinusoidal patterns (Fig. 4b; Extended Data Fig. 2). Importantly, our analysis indicates that the variability observed for some variables within the MER exhibit greater amplitude and shorter periodicity with distance from the centre of the upwelling compared to those of the RSR (Fig. 4b; Extended Data Fig. 2). Further, the observed variation in Pb isotopes within the RSR suggests that the upwelling may be chemically heterogeneous for some elements, whereas others show a narrower range in composition (e.g.,  $^{87}\text{Sr}/^{86}\text{Sr}$  is more heterogeneous than  $^{143}\text{Nd}/^{144}\text{Nd}$ ; Fig 1; Extended Data Fig 1). Although  $\Delta\text{Nb}$  values are almost consistently positive ( $>0$ ) across the region (except around Boset-Bericha Volcano), we identify small-scale differences in La/Sm and Vs at 100 km depth, within the likely melt-rich zone of the asthenosphere [26], with distance to upwelling centre in each rift (Fig. 4b; Extended Data Fig. 2). These small-scale differences indicate locally variable degrees of melting across the study region, agreeing with previous studies that reported low velocity areas [e.g., 37, 39]. This raises the question: do the zones of locally higher melt fraction, low Vs, and variable geochemistry observed in one rift correspond, spatially and compositionally, to those observed in the other two rifts? If so, this could indicate a shared melt source.

To address the spatial heterogeneity patterns observed and investigate the potential shared melt source, we carried out principal component analysis (PCA) and K-means cluster analysis using all variables post-standardisation (Methods). Across all variables, the K-means cluster analysis algorithm seeks to group similar observations whilst minimising the within-cluster total sum

of squares for a pre-specified number of clusters. Our K-means cluster analysis shows a higher number of clusters that are smaller in geographic size for the MER (50-100 km length scale; 4 clusters) compared to the RSR (150-200 km length scale; 3 clusters) (Fig. 5; Methods). Several clusters (clusters 1-3) are found to co-exist in different rift-arms. For example, samples assigned to cluster 3 are observed in the distal section of the RSR, as well as in locations closer to the MER rift centre (Fig. 5). The three clusters (1-3) observed across the RSR match the initial ~200 km clustering sequence observed across the MER. This sequential repeated clustering may indicate that they are derived from a shared source melt. However, the sequence of these melts—as indicated by clusters—within the MER occurs over a shorter distance compared to that of the RSR.

The spatial distribution of clusters reflects spatial variations in the composition and abundance of melt, which shares some cursory similarities to the magmatic segments observed at the surface (Fig. 5). However, when inspected in detail we observe clear differences. For example, volcanic systems both within magmatic segments and the adjacent rift flanks are commonly allocated to single clusters, and the boundaries between clusters and known magmatic segments are typically mismatched (Fig. 5). In Afar, the length of the region containing clusters is longer than that of magmatic segments. We therefore infer that the compositional variability of mantle upwelling is unlikely to be related to the along-axis segmentation of crustal subvolcanic plumbing systems.

### **Tectonic Control on Flow of Upwelling**

Taken together, our data can be explained through a single upwelling model with internal heterogeneity between rifts (e.g., refs.[31, 35, 40, 41]), as shown by the spline model. Crucially, the K-means cluster analysis indicates the signatures of geochemical variability (i.e., clusters) are repeated across rifts, implicating pulses of upwelling from the same source, as inferred for

other mantle plumes (e.g., refs.[36, 40, 41]). Rifts act as natural channels for upwelling melt from deeper mantle sources [42]. Considering the high extension rate in the RSR (10.5-19.5 mm/yr; [43]) compared to that of the MER (~5.2 mm/yr; [43]), it is plausible that a mantle flow rate is impeded by the narrowing of the rift in the MER. This process would lead to a ‘bottleneck’ effect [42, 44, 45], which in turn may result in a different length scale of mantle heterogeneity (Fig. 4; Extended Data Fig. 2) between the RSR and MER (Fig. 5). Further, a contrast in crustal thickness is evident between the rifts, with the MER crust being thicker (25-33 km [46]) than that of RSR (16-25 km [47]; Extended Data Fig. 1). Assuming a correlation between crustal and overall plate thickness, this effect is expected to introduce differences in mantle flow rate along each rift in Afar. A progressive thickening of the overlying lithosphere away from the upwelling centre in the MER should reduce the volume capacity for melt, impeding mantle flow. Consequently, the heterogeneous nature of the pulsed upwelling would exhibit a more condensed spatial pattern within the MER compared to RSR, as we observe (Fig. 5).

We conclude that variations in melt composition and abundance in and around Afar is best explained by a heterogeneous pulsing mantle upwelling that is not symmetrical (Fig. 5) but is instead shaped by both variable lithospheric thinning and extension rates within each rift (Fig. 6). Whilst this model principally investigates the likelihood of a singular or three-small-scale upwelling scenario, our results demonstrate that for either option, a single heterogeneous upwelling provides the best match to observations in the region. The detected variations in melt composition and abundance between the MER and RSR imply that the length scale of heterogeneities within magma-assisted rifting environments may be controlled not only by the upwelling itself, but by the extension rate and plate thickness. If this model is correct, it demonstrates that the evolution of a mantle upwelling can be influenced and shaped by the dynamics of the overriding plates.



## Acknowledgements

E.J.W was supported by Natural Environmental Research Council UK through the SPITFIRE Doctoral Training Partnership [grant number [NE/L002531/1](#)] and Wyley Fund of the Geologists' Association. E.J.W. is currently supported as part of the UKRI FLF award held at Swansea University (MR/YO11767/1). T.G. and T.H. receive funding from the WoodNext Foundation, a component fund administered by the Greater Houston Community Foundation. We acknowledge the use of rocks from the Afar Repository of the University of Pisa, Italy (<http://repositories.dst.unipi.it/index.php/home-afar>). We appreciate all those directly or indirectly involved in the field-campaign in the 1960s and acknowledge their contributions to the growing research within the region. We thank G.L. Foster and M. Cassidy for their helpful comments on an early version of the manuscript.

## Author Contributions

E.J.W. conceived the idea, processed the data, and prepared the manuscript. T.M.G and D.K. advised on the work and assisted with sampling and interpretation. P.J. wrote the code for the statistical modelling and assisted with interpretation. T.K.H advised on the statistical analysis. E.J.W., R.R., M.S., M.J.C., A.M., J.A.M., and R.N.T analysed the samples and processed the geochemical data. E.L.C processed the geophysical data for the sample locations. E.J.W., T.M.G., and D.K. wrote the manuscript with input from all co-authors.

## Competing Interests Statement

The authors declare no competing interests.

## Figure Captions

**Fig. 1: Variation in geochemical and geophysical properties around the Afar Triangle;** (a) Map showing the Gulf of Aden Rift (GoA), Red Sea Rift (RSR) and the Main Ethiopian Rift (MER) axes (dashed lines) and associated rifting rates indicated by arrows (from refs. [43,48]). The three hypothesised [19, 37, 38] upwelling locations (yellow stars) and Holocene volcanoes (red triangles) are shown. Hexmap colours show the density of samples within the hexagons' area, with purple representing >12 and yellow showing 1-2. Location of maps shown on global inset (black rectangle). (b) Hexmap showing the  $^{206}\text{Pb}/^{204}\text{Pb}$  variations across the study region (dark blue = low  $^{206}\text{Pb}/^{204}\text{Pb}$  - minimal upwelling signature, yellow = high  $^{206}\text{Pb}/^{204}\text{Pb}$ ). (c) Hexmap showing La/Sm variations across the study region (yellow = high La/Sm – low melt fraction, dark blue = low La/Sm – high melt fraction). (d) Hexmap showing the  $^{143}\text{Nd}/^{144}\text{Nd}$  variations across the study region. Yellow indicates a high  $^{143}\text{Nd}/^{144}\text{Nd}$ . The topography shown is from the 1 arc-sec (~30 m resolution) Shuttle Radar Topography Mission (SRTM) Digital Elevation Model (DEM) [50].

**Fig. 2: Radiogenic isotope compositions of samples across Afar.** (a)  $^{206}\text{Pb}/^{204}\text{Pb}$  versus  $^{208}\text{Pb}/^{204}\text{Pb}$ ; (b)  $^{143}\text{Nd}/^{144}\text{Nd}$  versus  $^{87}\text{Sr}/^{86}\text{Sr}$ . Samples are classified by their rift position, indicated by their symbol colour and shape (RSR = blue circles, MER = green squares, GoA = yellow diamonds). Error bars show the uncertainty associated. Black error bars are the average uncertainty of the dataset, grey are the maximum uncertainty. Uncertainty for datapoints in (a) are smaller than the symbols. The global mantle endmember compositions are shown as fields behind from refs.[5, 49]. The histograms show the distribution of all data analysed in our study, including our >130 data points.

**Fig. 3: Conceptual models of mantle upwellings beneath Afar tested in this study.** Schematic diagram of the upwelling scenarios for Afar tested in this study. The diagrams (left) are labelled

with the code associated with each model (see Extended Data Table 2 and the Statistical Analysis section within Methods for further details). The location of the purported mantle upwellings are shown by the star symbol. The number of lines shown on the schematic graphs equals the number of models that must be fitted for that model variant (linear = dashed, spline = continuous), where R = Rift and U = upwelling. Note that each model variant has been illustrated with an indicator that decreases with a reduction in upwelling proportion.

**Fig. 4: Statistical analysis of rifting models for the RSR, GoA and MER.** (a) Pearson correlation coefficient of each of the selected 13 variables with Moho depth. Error bars show the 95-percentile error of the coefficient ( $n = 250$ ) with the squares representing the mean. Red squares indicate where the correlation is significant ( $p < 0.05$ ) and blue squares indicate that the correlations are not deemed significant ( $p > 0.05$ ). (b) Splines (a smooth, flexible polynomial curve) of the best overall model—that is, C1C—for selected variables. Symbols show the data within the study (locations denoted by symbols shown). 95% confidence intervals are indicated by the shaded background. The number of data observations ( $n$ ) for La/Sm,  $^{143}\text{Nd}/^{144}\text{Nd}$ ,  $^{206}\text{Pb}/^{204}\text{Pb}$  and Shear velocity at 100km depth are 269, 218, 185, and 184 respectively. Uncertainty in data values have been shown by error bars (average in black, max in grey). (c) The mean standardised root means square error of prediction (RMSEP) for each of the models tested. Individual linear model results are shown by red squares and the mean of those results are displayed by the red line. Individual spline results are shown by blue circles and the mean of those results are shown by a blue line. All models were run for 100 iterations to capture the probable uncertainty distribution, as shown by the data points. Mean (dotted line) and 95% confidence interval (shaded) of results using perturbed data (within the uncertainty of each datapoint) are also shown (300 perturbation runs each using 100 iterations).

**Fig. 5: Map of the segments and cluster assignment within the study region.** Segments are shown in blue from north to south: Erta Ale Volcanic Segment (EAVS), Tat'Ale Volcanic

Segment (TAVS), Alayta Volcanic Segment (AVS), Dabbahu Volcanic Segment (DVS), Gabillema Volcanic Segment (GVS), Adda'do Magmatic Segment (AMS), Fentale-Dofen Magmatic Segment (FDMS), Boset Magmatic Segment (BMS), Aluto-Gedamsa Magmatic Segment (AGMS), Corbetti Magmatic Segment (CMS). Rift axis (dotted line) is shown. (b) and (c) are enlarged maps of the boxes shown in (a). (d) & (e) Principal component (PC) analysis bi-plot (PC1 vs PC2) when considering the six isotopic systems (see Extended Data Table 3) showing the samples and their component scores relative to those of the mantle endmembers. Values used for the mantle endmembers, that is, Pan-African Lithosphere (PAL), Enriched Mantle 1 & 2 (EM1, EM2, respectively), Depleted MORB Mantle (DMM) and HiMU, are shown in Extended Table 3. The topography shown is from the 1 arc-sec (~30 m resolution) Shuttle Radar Topography Mission (SRTM) Digital Elevation Model (DEM) [50].

**Fig. 6: Spatially heterogeneous nature of the mantle upwelling beneath Afar.** (a) Box diagram showing the rifts across Afar and the mantle upwelling being channelised by the rift. The lines of section X-Y-Z are those shown in panel (c). Volcanic segments are shown and labelled: Erta Ale Volcanic Segment (EAVS), Tat'Ale Volcanic Segment (TAVS), Alayta Volcanic Segment (AVS), Dabbahu Volcanic Segment (DVS), Gabillema Volcanic Segment (GVS), Adda'do Magmatic Segment (AMS), Fentale-Dofen Magmatic Segment (FDMS). (b) Schematic of the Afar upwelling showing the dimensions of channelised flow along the three rifts (dashed lines). (c) Schematic cross sections along the Red Sea Rift (line section X-Y) and MER (Y-Z) showing the distribution of chemical heterogeneities within the upwelling and how those map to the clusters shown in Fig. 5. Note that the depths of distinct features including the Lithosphere-Asthenosphere Boundary (LAB) are not shown to scale.

## References

- [1] Cañón-Tapia, E., & Walker, G. P. (2004). Global aspects of volcanism: the perspectives of “plate tectonics” and “volcanic systems”. *Earth-Science Reviews*, 66(1-2), 163-182. <https://doi.org/10.1016/j.earscirev.2003.11.001>
- [2] White, R., & McKenzie, D. (1989). Magmatism at rift zones: the generation of volcanic continental margins and flood basalts. *Journal of Geophysical Research: Solid Earth*, 94(B6), 7685-7729. <https://doi.org/10.1029/JB094IB06P07685>
- [3] Koptev, A., Calais, E., Burov, E., Leroy, S., & Gerya, T. (2015). Dual continental rift systems generated by plume–lithosphere interaction. *Nature Geoscience*, 8(5), 388-392. <https://doi.org/10.1038/ngeo2401>
- [4] Fitton, J. G. (1983). Active versus passive continental rifting: evidence from the West African rift system. *Tectonophysics*, 94(1-4), 473-481. [https://doi.org/10.1016/0040-1951\(83\)90030-6](https://doi.org/10.1016/0040-1951(83)90030-6)
- [5] Zindler, A., & Hart, S. (1986). Chemical geodynamics. IN: *Annual review of earth and planetary sciences*. Volume 14 (A87-13190 03-46). Palo Alto, CA, Annual Reviews, Inc., 1986, p. 493-571., 14, 493-571.
- [6] Rogers, N., Macdonald, R., Fitton, J. G., George, R., Smith, M., & Barreiro, B. (2000). Two mantle plumes beneath the East African rift system: Sr, Nd and Pb isotope evidence from Kenya Rift basalts. *Earth and Planetary Science Letters*, 176(3-4), 387-400. [https://doi.org/10.1016/S0012-821X\(00\)00012-1](https://doi.org/10.1016/S0012-821X(00)00012-1)
- [7] Leroy, S., d'Acremont, E., Tiberi, C., Basuyau, C., Autin, J., Lucazeau, F., & Sloan, H. (2010). Recent off-axis volcanism in the eastern Gulf of Aden: implications for plume–ridge

- 379 interaction. *Earth and Planetary Science Letters*, 293(1-2), 140-153.  
 380 <https://doi.org/10.1016/j.epsl.2010.02.036>
- 381 [8] Szymanski, E., Stockli, D. F., Johnson, P. R., & Hager, C. (2016). Thermochronometric  
 382 evidence for diffuse extension and two-phase rifting within the Central Arabian Margin of the  
 383 Red Sea Rift. *Tectonics*, 35(12), 2863-2895. <https://doi.org/10.1002/2016TC004336>
- 384 [9] Wolfenden, E., Ebinger, C., Yirgu, G., Deino, A., & Ayalew, D. (2004). Evolution of the  
 385 northern Main Ethiopian rift: birth of a triple junction. *Earth and Planetary Science Letters*,  
 386 224(1-2), 213-228. <https://doi.org/10.1016/j.epsl.2004.04.022>
- 387 [10] Bellahsen, N., Faccenna, C., Funicello, F., Daniel, J. M., & Jolivet, L. (2003). Why did  
 388 Arabia separate from Africa? Insights from 3-D laboratory experiments. *Earth and Planetary*  
 389 *Science Letters*, 216(3), 365-381. [https://doi.org/10.1016/S0012-821X\(03\)00516-8](https://doi.org/10.1016/S0012-821X(03)00516-8)
- 390 [11] Koptev, A., Gerya, T., Calais, E., Leroy, S., & Burov, E. (2018). Afar triple junction  
 391 triggered by plume-assisted bi-directional continental break-up. *Scientific reports*, 8(1), 14742.  
 392 <https://doi.org/10.1038/s41598-018-33117-3>
- 393 [12] Zwaan, F., Corti, G., Keir, D., & Sani, F. (2020). A review of tectonic models for the rifted  
 394 margin of Afar: Implications for continental break-up and passive margin formation. *Journal*  
 395 *of African Earth Sciences*, 164, 103649. <https://doi.org/10.1016/j.jafrearsci.2019.103649>
- 396 [13] Rychert, C. A., Hammond, J. O., Harmon, N., Michael Kendall, J., Keir, D., Ebinger, C.,  
 397 ... & Stuart, G. (2012). Volcanism in the Afar Rift sustained by decompression melting with  
 398 minimal plume influence. *Nature Geoscience*, 5(6), 406-409. <https://doi.org/10.1038/ngeo1455>
- 399 [14] Rooney, T. O. (2020). The Cenozoic magmatism of East Africa: part IV—the terminal  
 400 stages of rifting preserved in the Northern East African Rift System. *Lithos*, 360, 105381.  
 401 <https://doi.org/10.1016/j.lithos.2020.105381>

- [15] Schilling, J. G. (1973). Afar mantle plume: rare earth evidence. *Nature Physical Science*, 242(114), 2-5. <https://doi.org/10.1038/physci242002a0>
- [16] Ferguson, D. J., MacLennan, J., Bastow, I. D., Pyle, D. M., Jones, S. M., Keir, D., ... & Yirgu, G. (2013). Melting during late-stage rifting in Afar is hot and deep. *Nature*, 499(7456), 70-73. <https://doi.org/10.1038/nature12292>
- [17] Armitage, J. J., Ferguson, D. J., Goes, S., Hammond, J. O., Calais, E., Rychert, C. A., & Harmon, N. (2015). Upper mantle temperature and the onset of extension and break-up in Afar, Africa. *Earth and Planetary Science Letters*, 418, 78-90. <https://doi.org/10.1016/j.epsl.2015.02.039>
- [18] Hansen, S. E., & Nyblade, A. A. (2013). The deep seismic structure of the Ethiopia/Afar hotspot and the African superplume. *Geophysical Journal International*, 194(1), 118-124. <https://doi.org/10.1093/gji/ggt116>
- [19] Schilling, J. G., Kingsley, R. H., Hanan, B. B., & McCully, B. L. (1992). Nd-Sr-Pb isotopic variations along the Gulf of Aden: Evidence for Afar mantle plume-continental lithosphere interaction. *Journal of Geophysical Research: Solid Earth*, 97(B7), 10927-10966. <https://doi.org/10.1029/92jb00415>
- [20] Hagos, M., Koeberl, C., & de Vries, B. V. W. (2016). The Quaternary volcanic rocks of the northern Afar Depression (northern Ethiopia): Perspectives on petrology, geochemistry, and tectonics. *Journal of African Earth Sciences*, 117, 29-47. <https://doi.org/10.1016/J.JAFREARSCI.2015.11.022>
- [21] Global Volcanism Program, 2024. [Database] Volcanoes of the World (v. 5.2.5; 23 Dec 2024). Distributed by Smithsonian Institution, compiled by Venzke, E. <https://doi.org/10.5479/si.GVP.VOTW5-2024.5.2>

- 425 [22] Weis, D., Harpp, K. S., Harrison, L. N., Boyet, M., Chauvel, C., Farnetani, C. G., ... &  
 426 Williamson, N. M. (2023). Earth's mantle composition revealed by mantle plumes. *Nature*  
 427 *Reviews Earth & Environment*, 4(9), 604-625. <https://doi.org/10.1038/s43017-023-00467-0>
- 428 [23] Jackson, M. G., Becker, T. W., & Steinberger, B. (2021). Spatial characteristics of  
 429 recycled and primordial reservoirs in the deep mantle. *Geochemistry, Geophysics, Geosystems*,  
 430 22(3), e2020GC009525. <https://doi.org/10.1029/2020GC009525>
- 431 [24] Hart, S. R., Hauri, E. H., Oschmann, L. A., & Whitehead, J. A. (1992). Mantle plumes and  
 432 entrainment: isotopic evidence. *Science*, 256(5056), 517-520.  
 433 <https://doi.org/10.1126/SCIENCE.256.5056.517>
- 434 [25] Hanan, B. B., & Graham, D. W. (1996). Lead and helium isotope evidence from oceanic  
 435 basalts for a common deep source of mantle plumes. *Science*, 272(5264), 991-995.  
 436 <https://doi.org/10.1126/science.272.5264.991>
- 437 [26] Hutchison, W., Mather, T. A., Pyle, D. M., Boyce, A. J., Gleeson, M. L., Yirgu, G., ... &  
 438 Finch, A. A. (2018). The evolution of magma during continental rifting: New constraints from  
 439 the isotopic and trace element signatures of silicic magmas from Ethiopian volcanoes. *Earth*  
 440 *and Planetary Science Letters*, 489, 203-218. <https://doi.org/10.1016/j.epsl.2018.02.027>
- 441 [27] Fitton, J. G., Saunders, A. D., Norry, M. J., Hardarson, B. S., & Taylor, R. N. (1997).  
 442 Thermal and chemical structure of the Iceland plume. *Earth and Planetary Science Letters*,  
 443 153(3-4), 197-208. [https://doi.org/10.1016/S0012-821X\(97\)00170-2](https://doi.org/10.1016/S0012-821X(97)00170-2)
- 444 [28] Benoit, M. H., Nyblade, A. A., & VanDecar, J. C. (2006). Upper mantle P-wave speed  
 445 variations beneath Ethiopia and the origin of the Afar hotspot. *Geology*, 34(5), 329-332.  
 446 <https://doi.org/10.1130/G22281.1>



- 447 [29] Ritsema, J., & Allen, R. M. (2003). The elusive mantle plume. *Earth and Planetary Science*  
448 *Letters*, 207(1-4), 1-12. [https://doi.org/10.1016/S0012-821X\(02\)01093-2](https://doi.org/10.1016/S0012-821X(02)01093-2)
- 449 [30] Chambers, E. L., Harmon, N., Rychert, C. A., Gallacher, R. J., & Keir, D. (2022). Imaging  
450 the seismic velocity structure of the crust and upper mantle in the northern East African Rift  
451 using Rayleigh wave tomography. *Geophysical Journal International*, 230(3), 2036-2055.  
452 <https://doi.org/10.1093/gji/ggac156>
- 453 [31] Illsley-Kemp, F., Keir, D., Bull, J. M., Gernon, T. M., Ebinger, C., Ayele, A., ... &  
454 Belachew, M. (2018). Seismicity during continental breakup in the Red Sea rift of Northern  
455 Afar. *Journal of Geophysical Research: Solid Earth*, 123(3), 2345-2362.  
456 <https://doi.org/10.1002/2017JB014902>
- 457 [32] DIGIS Team: GEOROC Compilation: Rift Volcanics (2021).  
458 <https://doi.org/10.25625/KAIVCT>
- 459 [33] Chambers, E. L., Harmon, N., Keir, D., & Rychert, C. A. (2019). Using ambient noise to  
460 image the northern East African Rift. *Geochemistry, Geophysics, Geosystems*, 20(4), 2091-  
461 2109. <https://doi.org/10.1029/2018GC008129>
- 462 [34] Hofmann, A. W., Jochum, K. P., Seufert, M., & White, W. M. (1986). Nb and Pb in  
463 oceanic basalts: new constraints on mantle evolution. *Earth and Planetary science letters*, 79(1-  
464 2), 33-45. [https://doi.org/10.1016/0012-821X\(86\)90038-5](https://doi.org/10.1016/0012-821X(86)90038-5)
- 465 [35] Abouchami, W., Hofmann, A. W., Galer, S. J. G., Frey, F. A., Eisele, J., & Feigenson, M.  
466 (2005). Lead isotopes reveal bilateral asymmetry and vertical continuity in the Hawaiian  
467 mantle plume. *Nature*, 434(7035), 851-856. <https://doi.org/10.1038/nature03402>

- 468 [36] Taylor, R. N., Davila-Harris, P., Branney, M. J., Farley, E. R., Gernon, T. M., & Palmer,  
 469 M. R. (2020). Dynamics of a chemically pulsing mantle plume. *Earth and Planetary Science*  
 470 *Letters*, 537, 116182. <https://doi.org/10.1016/j.epsl.2020.116182>
- 471 [37] Civiero, C., Armitage, J. J., Goes, S., & Hammond, J. O. (2019). The seismic signature of  
 472 upper-mantle plumes: Application to the Northern East African Rift. *Geochemistry,*  
 473 *Geophysics, Geosystems*, 20(12), 6106-6122. <https://doi.org/10.1029/2019GC008636>
- 474 [38] Rooney, T. O., Hanan, B. B., Graham, D. W., Furman, T., Blichert-Toft, J., & Schilling,  
 475 J. G. (2012). Upper mantle pollution during Afar plume–continental rift interaction. *Journal of*  
 476 *Petrology*, 53(2), 365-389. <https://doi.org/10.1093/petrology/egr065>
- 477 [39] Gallacher, R. J., Keir, D., Harmon, N., Stuart, G., Leroy, S., Hammond, J. O., ... & Ahmed,  
 478 A. (2016). The initiation of segmented buoyancy-driven melting during continental breakup.  
 479 *Nature Communications*, 7(1), 13110. <https://doi.org/10.1038/ncomms13110>
- 480 [40] Ito, G. (2001). Reykjanes' V'-shaped ridges originating from a pulsing and dehydrating  
 481 mantle plume. *Nature*, 411(6838), 681-684. <https://doi.org/10.1038/35079561>
- 482 [41] Parkin, C. J., Lunnø, Z. C., White, R. S., Christie, P. A., & Integrated Seismic Imaging  
 483 & Modelling of Margins Project (iSIMM) Team. (2007). Imaging the pulsing Iceland mantle  
 484 plume through the Eocene. *Geology*, 35(1), 93-96. <https://doi.org/10.1130/G23273A.1>
- 485 [42] Ebinger, C. J., & Sleep, N. H. (1998). Cenozoic magmatism throughout east Africa  
 486 resulting from impact of a single plume. *Nature*, 395(6704), 788-791.  
 487 <https://doi.org/10.1038/27417>
- 488 [43] Zwaan, F., Corti, G., Sani, F., Keir, D., Muluneh, A. A., Illsley-Kemp, F., & Papini, M.  
 489 (2020). Structural analysis of the Western Afar Margin, East Africa: Evidence for multiphase  
 490 rotational rifting. *Tectonics*, 39(7), e2019TC006043. <https://doi.org/10.1029/2019TC006043>

- [44] Chang, S. J., & Van der Lee, S. (2011). Mantle plumes and associated flow beneath Arabia and East Africa. *Earth and Planetary Science Letters*, 302(3-4), 448-454. <https://doi.org/10.1016/j.epsl.2010.12.050>
- [45] Hansen, A. H. (2023) "Flow Through Restriction." In *Fluid Power Systems: A Lecture Note in Modelling, Analysis and Control*, pp. 43-61. Cham: Springer International Publishing. [https://doi.org/10.1007/978-3-031-15089-0\\_4](https://doi.org/10.1007/978-3-031-15089-0_4)
- [46] Maguire, P. K. H., Keller, G. R., Klemperer, S. L., Mackenzie, G. D., Keranen, K., Harder, S., O'Reilly, B., Thybo, H., Asfaw, L., Khan, M. A., & Amha, M. (2006). Crustal structure of the northern Main Ethiopian Rift from the EAGLE controlled-source survey; a snapshot of incipient lithospheric break-up. *Geological Society, London, Special Publications*, 259(1), 269-292. <https://doi.org/10.1144/GSL.SP.2006.259.01.21>
- [47] Lewi, E., Keir, D., Birhanu, Y., Blundy, J., Stuart, G., Wright, T., & Calais, E. (2016). Use of a high-precision gravity survey to understand the formation of oceanic crust and the role of melt at the southern Red Sea rift in Afar, Ethiopia. *Special Publications*, 420(1), 165-180. <https://doi.org/10.1144/SP420.13>
- [48] Gillard, M., Leroy, S., Cannat, M., & Sloan, H. (2021). Margin-to-margin seafloor spreading in the eastern Gulf of Aden: a 16 Ma-long history of deformation and magmatism from seismic reflection, gravity and magnetic data. *Frontiers in Earth Science*, 9, 707721. <https://doi.org/10.3389/feart.2021.707721>
- [49] Rollinson, H., & Pease, V. (2021). Using Radiogenic Isotope Data. In *Using Geochemical Data: To Understand Geological Processes* (pp. 178–218). chapter, Cambridge: Cambridge University Press.

513 [50] NASA JPL (2013). NASA Shuttle Radar Topography Mission Global 1 arc second [Data  
514 set]. NASA EOSDIS Land Processes DAAC. Accessed 2021-09-03  
515 from <https://doi.org/10.5067/MEaSUREs/SRTM/SRTMGL1.003>

## Methods

### *Sample Selection and Processing*

All samples and previously published data used in this study must originate from a volcano that has been active within the Holocene [21] (Fig. 1), with the age of the sample estimated to be of Quaternary age (i.e., < 2.58 Ma). An essential criterion was that all samples have a precisely known location with accurate coordinates.

### *Obtaining Previously Published Data*

Previously published geochemical data were obtained from GeoROC [19, 32]. Once downloaded the data-files were filtered to only include data within Ethiopia (including the Main Ethiopian Rift and Afar). These data were further filtered using the following criteria:

1. The values for the sample must relate to whole rock geochemistry, as opposed to mineral separates.
2. The individual sample must have major element, trace element,  $^{87}\text{Sr}/^{86}\text{Sr}$ ,  $^{143}\text{Nd}/^{144}\text{Nd}$ ,  $^{206}\text{Pb}/^{204}\text{Pb}$ ,  $^{207}\text{Pb}/^{204}\text{Pb}$  and  $^{208}\text{Pb}/^{204}\text{Pb}$  isotope values available.
3. The coordinates must be specific to the individual sample's location rather than providing an average coordinate for a broader study area.

### *Sampling and Sample Preparation*

Ninety-three lavas, eleven welded tuffs and one pumice sample, from various volcanoes in Afar (Erta Ale Volcanic Segment, Ayelu, Abida, Yangudi, Dama Ali, Kerub, Ela, Didoli, Abbahu, Afdera, Tat Ali and Manda Hararo) were selected for geochemical analysis [see refs.51-53]. The samples were collected during the CNR/CNRS projects in Afar during the 1960s [54] and stored in the Afar Repository at the University of Pisa, Italy, (<http://repositories.dst.unipi.it/index.php/home-afar>). A further 52 samples from the Boset-

Bericha Volcanic Complex (BBVC) were collected during three field seasons [ref.55], in November 2012, April-May 2015 [ref.56], and February 2017 [ref.57].

Sample preparation, for major, trace and isotope analyses, was carried out at the University of Southampton. Samples were cut with a saw to remove any weathered sections, and any cut surfaces ground down to reduce any potential contamination by metals from the saw blade. Rock samples were then crushed using a fly press and placed in double-layered plastic bags prior to crushing to minimise metal contamination during the crushing process.

The crushed material was separated into three size fractions ( $>1$  mm, 0.5 mm to 1 mm,  $<0.5$  mm) using Teflon sieves, retaining the middle fraction (0.5 - 1 mm) for analysis. The selected fraction was cleaned by ultrasonication in Milli-Q water then dried overnight in an oven at  $85^{\circ}\text{C}$ . The cleaned rock chips were then hand-picked under a microscope, to remove any extraneous (non-rock) material. An aliquot of cleaned chips was used for Pb isotope analysis. For major element, trace element, and  $^{143}\text{Nd}/^{144}\text{Nd}$  and  $^{87}\text{Sr}/^{86}\text{Sr}$  isotope analysis, the remaining rock chips were ground to a fine powder using an agate mortar and pestle, again to minimise contamination with metals.

#### ***Trace Element Analysis***

Samples were prepared for whole-rock trace element analysis using 0.05 g (for BBVC samples) or 0.075 g (for all other samples) powdered sample. The powdered samples were digested in sealed Savillex Teflon vials with 15 drops concentrated  $\text{HNO}_3$  and 2 ml HF on a hotplate at  $130^{\circ}\text{C}$  for 24 hours (for all samples excluding those from the BBVC), or with 50 drops HF and 0.2 ml  $\text{HNO}_3$  on a hotplate at  $130^{\circ}\text{C}$  for 24 hours (for BBVC samples only). The  $\text{HNO}_3$ /HF was evaporated off, and the samples were refluxed in 6M HCl for another 24 hours on a hotplate at  $130^{\circ}\text{C}$ . The 6M HCl was evaporated off, and the samples were redissolved in 6M HCl. Mother solutions were prepared by adding 6M HCl and Milli-Q

water (total 30 ml) to the dissolved samples. Daughter solutions were prepared using 0.5 ml of mother solution, diluted to 5 ml with 3% HNO<sub>3</sub> (containing the internal standards 5 ppb In/ 5 ppb Re/ 20 ppb Be), resulting in an overall dilution factor of c. 4000.

Trace element analyses of the daughter samples were undertaken on the Thermo Scientific X Series 2 quadrupole inductively coupled plasma mass spectrometer (ICP-MS) at the University of Southampton. Samples and standards were spiked with internal standard elements and corrected for interferences and the blank and then calibrated using a suite of international rock standards. Accuracy was monitored using reference materials JA-2, BCR-2, JB-2 (see Supplementary Tables 1 and 2).

### ***Pb Isotopic Analysis***

For Pb isotope analysis, 0.3 g of cleaned, picked rock chips (0.5 mm to 1 mm) were weighed into Pb Savillex Teflon vials and leached on a hotplate with 4 ml 6M HCl for one hour (15 minutes for obsidian and pumice samples, to avoid full dissolution of the sample). Samples were rinsed several times in Milli-Q water, then 0.5 ml concentrated HNO<sub>3</sub>, before adding 3-4 ml of concentrated HF. Samples were digested, following the same procedure as for trace elements, and refluxed on a hotplate at 130 °C for 24 hours, before being evaporated to dryness. 0.5 ml concentrated HCl was added, and the sample evaporated to dryness. Then 0.5 ml concentrated HNO<sub>3</sub> was added and again evaporated to dryness. The final residue was reconstituted in 0.5 ml HBr and refluxed for an hour. The samples were cooled and centrifuged for 5 minutes. Pb was isolated using a single-stage HCl anion-exchange chromatographic resin separation method [58], with AGX-1x8, 200 – 400 mesh resin. Following this, the Pb isolate was dried down, redissolved in HNO<sub>3</sub>, and analysed using the double spike method of ref.[59]. The samples were subsequently analysed on a Thermo Scientific Neptune Multi-collector inductively coupled plasma mass spectrometer (MC-

ICPMS) at the University of Southampton (UK) achieving a NBS SRM 981 reproducibility of  $^{206}\text{Pb}/^{204}\text{Pb} = 16.9404 \pm 24$  (142 ppm),  $^{207}\text{Pb}/^{204}\text{Pb} = 15.4969 \pm 26$  (168 ppm),  $^{208}\text{Pb}/^{204}\text{Pb} = 36.7149 \pm 66$  (180 ppm) (2sd; n=44). Pb isotope measurements of the standard are within error of the accepted values ( $^{206}\text{Pb}/^{204}\text{Pb} = 16.9412$ ,  $^{207}\text{Pb}/^{204}\text{Pb} = 15.4988$ ,  $^{208}\text{Pb}/^{204}\text{Pb} = 36.7233$ ). Accuracy was 47 ppm for  $^{206}\text{Pb}/^{204}\text{Pb}$ , 123 ppm for  $^{207}\text{Pb}/^{204}\text{Pb}$ , and 174 ppm for  $^{208}\text{Pb}/^{204}\text{Pb}$ .

### *$^{143}\text{Nd}/^{144}\text{Nd}$ and $^{87}\text{Sr}/^{86}\text{Sr}$ Isotopic Analysis*

For Sr and Nd analysis, the remaining mother solutions from the preparation of trace element solutions (see above) were used for all samples except those of the BBVC. An aliquot of each mother solution was used, to give a volume of liquid containing at least 1  $\mu\text{g}$  Sr and 200 ng Nd and evaporated to dryness in Savillex Teflon vials on a hotplate at 130°C. Sample residues were reconstituted in 200  $\mu\text{l}$  1.75M HCl. For the BBVC samples, rock chips were leached in 4 ml 6M HCl or 30 minutes in Savillex Teflon vials (obsidian samples for only 15 minutes, to avoid full dissolution of the sample). The samples were then rinsed with Milli-Q water and  $\text{HNO}_3$ , and then the same digestion procedure as for trace element analysis (above) was followed. The final mother solutions were prepared using HCl and Milli-Q water to 30 ml for felsic samples and 20 ml for mafic samples.

All samples were then passed through ion exchange column chemistry, using a AG50-X8 200-400 mesh resin cation column to separate the Sr and Nd fractions. The sample fractions were subsequently evaporated to dryness, ready for further column chemistry.

Sr was further isolated through Sr-spec resin columns, following the methodology of ref.[60]. Samples were then evaporated to dryness, dissolved in 1.5 ml 1M HCl and loaded onto outgassed tantalum filaments with 1  $\mu\text{l}$  of Ta-activator. Sr isotopic analysis was performed on a Thermal Ionisation Mass Spectrometer (TIMS) Thermo Scientific Triton Plus at the



University of Southampton. Reference material SRM NIST987 ( $^{87}\text{Sr}/^{86}\text{Sr} = 0.710258$ ; GeoREM) was used to monitor accuracy and gave average  $^{87}\text{Sr}/^{86}\text{Sr}$  values of 0.710243. All samples were normalised to NBS SRM-987  $^{87}\text{Sr}/^{86}\text{Sr} = 0.710248$  [61], while reproducibility was  $\pm 0.000020$  (28.2 ppm, 2sd;  $n=464$ ). Accuracy was 21 ppm.

The Nd aliquot from the cation column was followed by an Ln-spec resin (50-100  $\mu\text{m}$ ) [60]. The samples were then evaporated to dryness and 3%  $\text{HNO}_3$  was added to produce a solution of 50 ppb.  $^{143}\text{Nd}/^{144}\text{Nd}$  analyses were undertaken on the ThermoScientific Neptune multi-collector inductively coupled plasma mass spectrometer (MC-ICP-MS) at the University of Southampton. Corrected Nd isotopic compositions were obtained using a method based on ref.[62] through adjustment to a  $^{146}\text{Nd}/^{144}\text{Nd}$  ratio of 0.7219 and a secondary normalisation to  $^{142}\text{Nd}/^{144}\text{Nd} = 1.141876$ . Reference material JNdi-1 was measured as an unknown ( $^{143}\text{Nd}/^{144}\text{Nd}$  of 0.512124, 2sd; [63]) achieving an average  $^{143}\text{Nd}/^{144}\text{Nd}$  of 0.512115 with an external reproducibility of  $\pm 0.000008$  (2sd, 15.2 ppm) across 6 analysis sessions over 2 years. The total column blanks (i.e., when blank acid is run through the column procedure) were negligible ( $<20$  pg) compared to the total amounts analysed (1  $\mu\text{g}$  and 200  $\mu\text{g}$ ) for Sr and Nd, respectively.

### ***Shear Velocity Mapping from Joint Inversion***

We use the shear wave velocity model of ref.[30] for inclusion in our analysis. The 3D velocity model is created through a joint inversion of Rayleigh-wave phase-velocities from ambient noise and teleseisms [30, 33]. The shear velocity model is parameterised every 5 km vertically with  $0.1^\circ \times 0.1^\circ$  pixel size for the upper 50 km. For deeper depths, an irregular spacing was used, increasing from 10 – 50 km spacings to match that of ref.[39]. For further details on the creation of the velocity model, the reader is directed to refs.[30, 33] and references therein.

For the analysis in this paper, the shear velocity model was interpolated to 1 km depth using a linear interpolation; we then extracted 1D columns of velocity with depth at the same resolution as our pixel size ( $0.1^\circ \times 0.1^\circ$ ).

### ***Moho Depths***

The gridded Moho depth map was produced from the Vs maps of ref.[33], described above. The Vs model was interpolated to a vertical grid spacing of 1 km. A velocity slice at the 3.75 km/s contour was extracted, which mapped best to previous receiver function measurements [65-69], active source experiments (e.g., ref.[70]) and previous S-wave models (e.g., ref.[71]).

### ***Statistical Models Considered***

As described in the text, five models were considered (see Extended Data Table 2), with each model being tested using a linear fit and a spline fit (Fig. 3). We note that a spline fit to itself can be linear if that is the best-fitting line.

Empirical models are estimated for the variation of each of 14 geochemical quantities (each of which is represented generically by random variable  $Y$ ) as a function of distance  $d \in [0, 1800]$  km for the five different models. Models are specified that explore the variation of  $Y$  with  $d$  in increasing complexity. The simplest model (C1C) assumes the existence of a single upwelling centre (at  $11.192^\circ\text{N}$   $41.784^\circ\text{E}$ ; see Figs. 1 & 3), with respect to which  $d$  is defined for all three rifts. The variation of  $Y$  with  $d$  is assumed common to all rifts. Model C3C assumes the existence of three upwelling centres (at  $11.192^\circ\text{N}$   $41.784^\circ\text{E}$ ,  $14.008^\circ\text{N}$   $40.458^\circ\text{E}$  &  $6.626^\circ\text{N}$   $37.948^\circ\text{E}$ ; see Fig. 1) based on ref.[37]; observations are allocated to the nearest upwelling centre, facilitating calculation of a single  $d$  for each observation. Like model C1C, the variation of  $Y$  with  $d$  is assumed common to all rifts, regardless of upwelling allocation. Model C1D assumes one upwelling centre (like C1C) for calculation of  $d$ , but now

the variation of  $Y$  with  $d$  is assumed to be different across rifts. Model C3D duplicates C3C for estimation of  $d$ , but variation of  $Y$  with  $d$  is assumed to be different across rifts. Finally, in model C3X, we consider the presence of three upwelling centres, with different variation of  $Y$  with  $d$  for each combination of upwelling and rift.

### ***Data Pre-Processing***

For models C1C and C1D, the distance between each sample and the upwelling locus centred on Lake Abhe (11.192170 °N, 41.783750 °E) is calculated. For models C3C, C3D and C3X, the distance between each sample and each of the three upwelling locations (Figs. 1 & 3) is measured, and then each sample is assigned to its nearest upwelling centre. The distance ( $d$ ) between two locations (i.e., upwelling and sample) is calculated using the spherical cosine law:

$$d = R(\cos^{-1}(\cos(a)\cos(b) + \sin(a)\sin(b)\cos(C))) \quad (\text{Eq. 5})$$

where  $a$  is the angle (in radians) from the North Pole to the sample location,  $b$  is the angle (in radians) from the North Pole to the upwelling location,  $C$  is the difference in radians between the longitude values of the sample and upwelling, and  $R$  is the radius of the earth in metres ( $6371 \times 10^3$ ).

### ***Penalised B-splines***

For each model, the variation of  $Y$  with  $d$  is described using a penalised B-spline (e.g., refs.[72-73]), the characteristics of which are selected to provide optimal predictive performance. First, for a large index set of locations equally spaced on the domain of distance, we calculate a B-spline basis matrix,  $B$  (e.g., ref.[74]) consisting of  $p$  equally spaced cubic spline basis functions. Then the value of  $Y$  on the index set is given by the vector  $B\beta$ , for spline coefficient vector  $\beta$  to be estimated. The value of  $p$  is specified to be sufficiently large to provide a good description of a highly variable  $Y$ . For a given data set, we penalise

the difference between consecutive values in  $\beta$  using a roughness penalty, such that the penalised spline exhibits optimal roughness, providing optimal predictive performance.

### *Estimating Optimal Spline Roughness and Predictive Performance*

For a sample of  $n_1$  training data, consisting of vectors of geochemical and geophysical quantities ( $y_1$ ) and distances ( $d_1$ ), we first allocate each element of  $d_1$  to its nearest neighbour in the index set, and hence construct the appropriate spline basis matrix  $B_1$  for the sample. We then assume that  $y_1 = B_1\beta + \varepsilon$ , where the elements of  $\varepsilon$  are independently and identically distributed zero-mean Gaussian random variables. We penalise the roughness of  $\beta$  using a first-difference penalty  $\lambda\beta'P\beta$ , where  $P = D'D$  and  $D$  is a first difference matrix (with elements  $D_{ij} = -1$  if  $i = j$ ;  $= 1$  if  $j = i + 1$ ; and  $= 0$  otherwise (e.g., ref.[75]). For a given choice of  $\lambda$ , we then find the optimal value of  $\beta$  by minimising lack of fit:

$$\beta^*(\lambda) = \underset{\beta}{\operatorname{argmin}} \{(y_1 - B_1\beta)'(y_1 - B_1\beta) + \lambda\beta'P\beta\} \quad (\text{Eq. 6})$$

$$= (B_1'B_1 + \lambda P)^{-1}B_1'y_1 \quad (\text{Eq. 7})$$

We can evaluate the predictive performance of the resulting spline description using a tuning set of  $n_2$  observations (independent of the training set) represented by vectors  $y_2$  and  $d_2$ . We again start by finding the appropriate spline basis matrix  $B_2$  for this sample. Then we can calculate the predictive mean square error for the tuning sample:

$$\text{MSE}_{\text{Tune}}(\lambda) = \frac{1}{n_2} (y_2 - B_2\beta^*(\lambda))'(y_2 - B_2\beta^*(\lambda)) \quad (\text{Eq. 8})$$

for each of a set of representative choices of values for  $\lambda$ . We can then select the optimal value of  $\lambda$  using

$$\lambda^* = \underset{\lambda}{\operatorname{argmin}} \{\text{MSE}_{\text{Tune}}(\lambda)\} \quad (\text{Eq. 9})$$

The value  $MSE_{Tune}(\lambda^*)$  is a biased estimate of predictive performance since the value of  $\lambda^*$  was tuned to minimise its value. We can obtain an unbiased estimate for the predictive performance of the spline model using a test set of  $n_3$  observations (independent of the training and tuning sets) represented by vectors  $y_3$  and  $d_3$  (and corresponding spline basis matrix  $B_3$ ). Then the predictive performance is estimated using:

$$MSE_{Test} = \frac{1}{n_3} (y_3 - B_3 \beta^*(\lambda^*))' (y_3 - B_3 \beta^*(\lambda^*)) \quad (\text{Eq. 10})$$

### ***Cross-Validation and Model Comparison***

We exploit cross-validation to evaluate  $MSE_{Test}$ , by partitioning the full sample of data into  $k > 2$  groups at random, withholding one group for tuning, another group for testing, and retaining the remaining  $k - 2$  groups for training. We then loop exhaustively over all possible combinations of choice of train, tune, and test groups, evaluating overall predictive performance on the test data over all iterations, noting that each observation occurs exactly once in the test set. For models requiring separate model fits to subsets of data (that is, C1D, C3D, C3X),  $MSE_{Test}$  is estimated using predictions from optimal predictive models for each subset. Further, we can repeat the analysis for different initial random partitioning of observations into  $k$  groups, to assess the sensitivity of overall predictive performance to this choice. We are careful to use the same cross-validation partitions to evaluate each of the five models, so that predictive performances can be compared fairly.

To quantify model performance over all 13 geochemical quantities ( $j = 1, 2, \dots, 13$ ), we define the overall standardised  $MSE_{Test}$

$$SMSE = \sum_{j=1}^{13} \frac{MSE_{Test,j}}{s_j^2} \quad (\text{Eq. 11})$$

where  $MSE_{Test,j}$  is the predictive performance for the  $j$ th geochemical indicator, and  $s_j^2$  is the sample estimate for the variance of that quantity. The estimation of the splines and the testing

of their predictive performance was repeated over 100 iterations. Results from each iteration and the mean of the SMSE is shown in Fig. 4.

### ***Linear Regression***

For comparison, we also evaluate linear regression models for the variation of  $Y$  with  $d$ . In the current notation, these can be thought of as simple models with basis matrix  $B = [1 \ d]$ , where  $1$  is a vector of appropriate length with each element  $= 1$ .  $B$  in this case is a 2-vector with elements corresponding to intercept and slope coefficients. Linear regression is approached using penalised B-spline models as the roughness coefficient  $\lambda \rightarrow \infty$ . That is, linear regression corresponds to a penalised B-spline model with very large  $\lambda$ . Therefore, a penalised B-spline model is guaranteed to perform at least as well as linear regression.

### ***Uncertainty of Model Performance***

To explore the effect of uncertainty on model performance, a perturbation analysis was undertaken. This analysis required the generation and modelling of  $n_{pert}$  new data samples. Each of these data samples corresponded to a perturbation of the original data sample. A value of  $n_{pert} = 300$  was selected to ensure that 95% uncertainty bands for predictive performance on perturbed data could be estimated with confidence.

In perturbed sample  $q$ ,  $q = 1, 2, \dots, n_{pert}$ , the value  $y_{ijq}^*$  of the  $i$ th observation for variable  $j$  was obtained by perturbing the corresponding value  $y_{ij}$  in the original data sample, using additive Gaussian noise  $e_{ijq}$ , the standard deviation  $\sigma_{ij}$  of which was informed by the known value of measurement uncertainty for that observation of the variable. Mathematically:

$$y_{ijq}^* = y_{ij} + e_{ijq} \quad (\text{Eq. 12})$$

The complete modelling procedure was then applied to each perturbed data sample in turn.

The predictive performance of different models was assessed over the  $n_{pert}$  perturbations, as

illustrated in Fig. 4, in terms of 95% uncertainty bands. The figure indicates that model C1D provides best predictive performance on perturbed data, as well as for the original unperturbed sample. Note that, since noise has been added to observations in the perturbation analysis, the overall performance of models on perturbed data is poorer than on the original sample, as expected.

### ***Testing the Influence of Crustal Assimilation***

We tested the influence of crustal assimilation further by excluding cases where Ce/Pb values fall below 20 and which could feasibly be associated with crustal assimilation [26, 34]. Using additional analysis, we confirm that excluding cases in which  $Ce/Pb < 20$  does not affect our overall results (see Extended Data Fig. 3a), suggesting that primary mantle compositional fluctuations (i.e., relative proportions of compositional mantle endmembers) exert the first-order control on eruptive compositions at the surface.

### ***Principal Component Analysis***

Principal component analysis (PCA) requires each sample or object to have the same number of values for each variable and so the dataset was reduced to 94 samples. PCA is only carried out on radiogenic isotope compositions of the samples where data are available for the mantle endmembers investigated (i.e., Afar plume, Pan-African Lithosphere, Depleted Mantle, Enriched Mantle 1, Enriched Mantle 2, HiMU; Fig. 5; Extended Data Table 3). While other purely geochemical studies on Afar (e.g., refs.[14, 38]) have included sub-crustal components such as the sub continental lithospheric mantle (SCLM), we decided not to include this endmember as it can sometimes be indistinguishable from certain mantle endmembers (i.e., EM1), especially in cases where the SCLM is metasomatized. Values used for the endmembers in our models are provided in Extended Data Table 3. Each object is standardised before being included in the PCA:

$$y_{stdj} = \frac{y_j - \bar{y}_j}{\sigma_j} \quad (\text{Eq. 13})$$

where  $\bar{y}_j$  is the mean of variable  $j$ , and  $\sigma_j$  is the standard deviation of the variable  $j$ :

$$\sigma_j = \sqrt{\frac{\sum \{(y_j - \bar{y}_j)\}^2}{N_j}} \quad (\text{Eq. 14})$$

where  $N_j$  is the number of objects within variable  $j$ .

Approximately 90.5% of the variance is explained within the plane of the first two eigenvectors, increasing to 95.5% when including the third eigenvector. The first principal component (PC-1) is most influenced by  $^{207}\text{Pb}/^{204}\text{Pb}$ ,  $^{208}\text{Pb}/^{204}\text{Pb}$ , whereas the second principal component (PC-2) is dominantly influenced by  $^{206}\text{Pb}/^{204}\text{Pb}$  and  $^{87}\text{Sr}/^{86}\text{Sr}$ . The third principal component (PC-3) is dominated by  $^{207}\text{Pb}/^{204}\text{Pb}$  and  $^{143}\text{Nd}/^{144}\text{Nd}$  (Supplementary Table 3).

#### ***K-means Cluster Analysis***

K-means cluster analysis [76] was carried out on the samples using the 13 standardised variables (Extended Data Table 1). The K-means algorithm assigns each object to a singular cluster that does not overlap with another (i.e., partitional clustering), minimising the total sum of squared error (SSE) from the centre point of each cluster, known as the centroid, to each data point.

To find the optimum number of clusters ( $k$ )—which reduces the within-cluster total sum of squares error with the lowest number of clusters—we run the K-means algorithm specifying  $k$  to be 1:20, over 1000 iterations for each  $k$  (Supplementary Fig. 1). We then select eight clusters based on  $k=8$ , reducing the within-cluster total sum of squares by 75% from  $k=1$ , and the range over the 1,000 iterations being minimised when  $k \geq 8$ . The cluster assignments for each object, out of the 1,000 iterations, are selected by finding the iteration number that is



closest to the mean within-cluster total sum of squares of that  $k$  value (shown by the blue line in Supplementary Fig. 1).

#### **Data Availability**

The datasets analysed for the current project are available as Supplementary Material. Some data were obtained from GeoROC [19,32,51]; these data are clearly marked in the datafile.

The data is freely available on FigShare at <https://doi.org/10.6084/m9.figshare.28769105> (ref 83)

#### **Code Availability**

The input data, code and output within this study is openly available and can be found at <https://github.com/ygraigarw/AfarPlume.git> (ref. 84)

#### **Methods-only References**

[51] Watts, E. J., Gernon, T. M., Taylor, R. N., Keir, D., & Pagli, C. (2023). Magmatic evolution during proto-oceanic rifting at Alu, Dalafilla and Borale Volcanoes (Afar) determined by trace element and Sr-Nd-Pb isotope geochemistry. *Lithos*, 456, 107311. <https://doi.org/10.1016/j.lithos.2023.107311>

[52] Watts, E. J., Gernon, T. M., Taylor, R. N., Keir, D., Siegburg, M., Jarman, J., ... & Gioncada, A. (2020). Evolution of the Alu-Dalafilla and Borale volcanoes, Afar, Ethiopia. *Journal of Volcanology and Geothermal Research*, 408, 107094. <https://doi.org/10.1016/j.jvolgeores.2020.107094>

[53] Rees, R., Gernon, T. M., Keir, D., Taylor, R. N., & Pagli, C. (2023). The spatial and volcanic evolution of Ayelu, Abida and Yangudi volcanoes in the Northern Main Ethiopian Rift–Southern Afar, Ethiopia. *Journal of Volcanology and Geothermal Research*, 440, 107846. <https://doi.org/10.1016/j.jvolgeores.2023.107846>

- 819 [54] Barberi, F., & Varet, J. (1970). The Erta Ale volcanic range (Danakil depression,  
820 northern afar, ethiopia). *Bulletin Volcanologique*, 34, 848-917.  
821 <https://doi.org/10.1007/BF02596805>
- 822 [55] Siegburg, M. (2019). Evolution of faulting and magmatism during volcanic rifting in the  
823 Ethiopian Rift: A case study of the Boset-Bericha Volcanic Complex (Doctoral dissertation,  
824 University of Southampton).
- 825 [56] Siegburg, M., Gernon, T. M., Bull, J. M., Keir, D., Barfod, D. N., Taylor, R. N., ... &  
826 Ayele, A. (2018). Geological evolution of the Boset-Bericha volcanic complex, Main  
827 Ethiopian Rift:  $^{40}\text{Ar}/^{39}\text{Ar}$  evidence for episodic Pleistocene to Holocene volcanism. *Journal of*  
828 *Volcanology and Geothermal Research*, 351, 115-133.  
829 <https://doi.org/10.1016/j.jvolgeores.2017.12.014>
- 830 [57] Siegburg, M., Gernon, T. M., Keir, D., Bull, J. M., Taylor, R. N., Watts, E. J., ... &  
831 Gebru, E. F. (2023). Temporal clustering of fissural eruption across multiple segments within  
832 the Ethiopian Rift. *Frontiers in Earth Science*, 11, 1169635.  
833 <https://doi.org/10.3389/feart.2023.1169635>
- 834 [58] Kamber, B. S., & Gladu, A. H. (2009). Comparison of Pb purification by anion-  
835 exchange resin methods and assessment of long-term reproducibility of Th/U/Pb ratio  
836 measurements by quadrupole ICP-MS. *Geostandards and Geoanalytical Research*, 33(2),  
837 169-181. <https://doi.org/10.1111/J.1751-908X.2009.00911.X>
- 838 [59] Taylor, R. N., Ishizuka, O., Michalik, A., Milton, J. A., & Croudace, I. W. (2015).  
839 Evaluating the precision of Pb isotope measurement by mass spectrometry. *Journal of*  
840 *Analytical Atomic Spectrometry*, 30(1), 198-213. <https://doi.org/10.1039/c4ja00279b>
- 841 [60] Pin, C., Briot, D., Bassin, C., & Poitrasson, F. (1994). Concomitant separation of  
842 strontium and samarium-neodymium for isotopic analysis in silicate samples, based on

specific extraction chromatography. *Analytica Chimica Acta*, 298(2), 209-217.

[https://doi.org/10.1016/0003-2670\(94\)00274-6](https://doi.org/10.1016/0003-2670(94)00274-6)

[61] Thirlwall, M. F. (1991). Long-term reproducibility of multicollector Sr and Nd isotope ratio analysis. *Chemical Geology: Isotope Geoscience section*, 94(2), 85-104.

[https://doi.org/10.1016/0168-9622\(91\)90002-E](https://doi.org/10.1016/0168-9622(91)90002-E)

[62] Pin, C., & Zalduegui, J. S. (1997). Sequential separation of light rare-earth elements, thorium, and uranium by miniaturized extraction chromatography: application to isotopic analyses of silicate rocks. *Analytica Chimica Acta*, 339(1-2), 79-89.

[https://doi.org/10.1016/S0003-2670\(96\)00499-0](https://doi.org/10.1016/S0003-2670(96)00499-0)

[63] Vance, D., & Thirlwall, M. (2002). An assessment of mass discrimination in MC-ICPMS using Nd isotopes. *Chemical Geology*, 185(3-4), 227-240.

[https://doi.org/10.1016/S0009-2541\(01\)00402-8](https://doi.org/10.1016/S0009-2541(01)00402-8)

[64] Tanaka, T., Togashi, S., Kamioka, H., Amakawa, H., Kagami, H., Hamamoto, T., ... & Dragusanu, C. (2000). JNdi-1: a neodymium isotopic reference in consistency with LaJolla neodymium. *Chemical Geology*, 168(3-4), 279-281. [https://doi.org/10.1016/S0009-](https://doi.org/10.1016/S0009-2541(00)00198-4)

[2541\(00\)00198-4](https://doi.org/10.1016/S0009-2541(00)00198-4)

[65] Hammond, J. O., Kendall, J. M., Stuart, G. W., Keir, D., Ebinger, C., Ayele, A., & Belachew, M. (2011). The nature of the crust beneath the Afar triple junction: Evidence from receiver functions. *Geochemistry, Geophysics, Geosystems*, 12(12).

<https://doi.org/10.1029/2011GC003738>

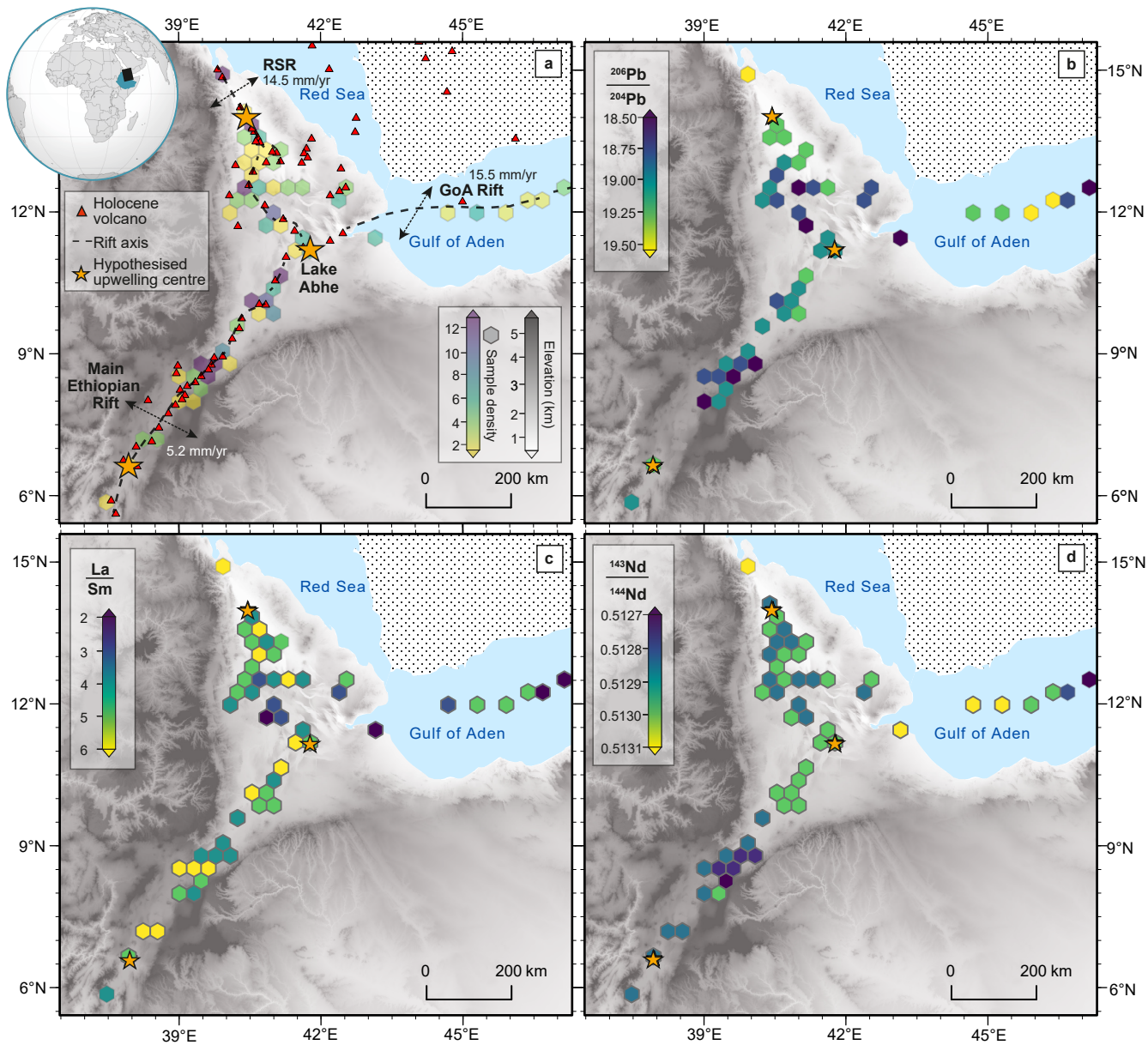
[66] Ayele, A., Stuart, G., & Kendall, J. M. (2004). Insights into rifting from shear wave splitting and receiver functions: An example from Ethiopia. *Geophysical Journal International*, 157(1), 354-362. <https://doi.org/10.1111/j.1365-246X.2004.02206.x>

<https://doi.org/10.1111/j.1365-246X.2004.02206.x>

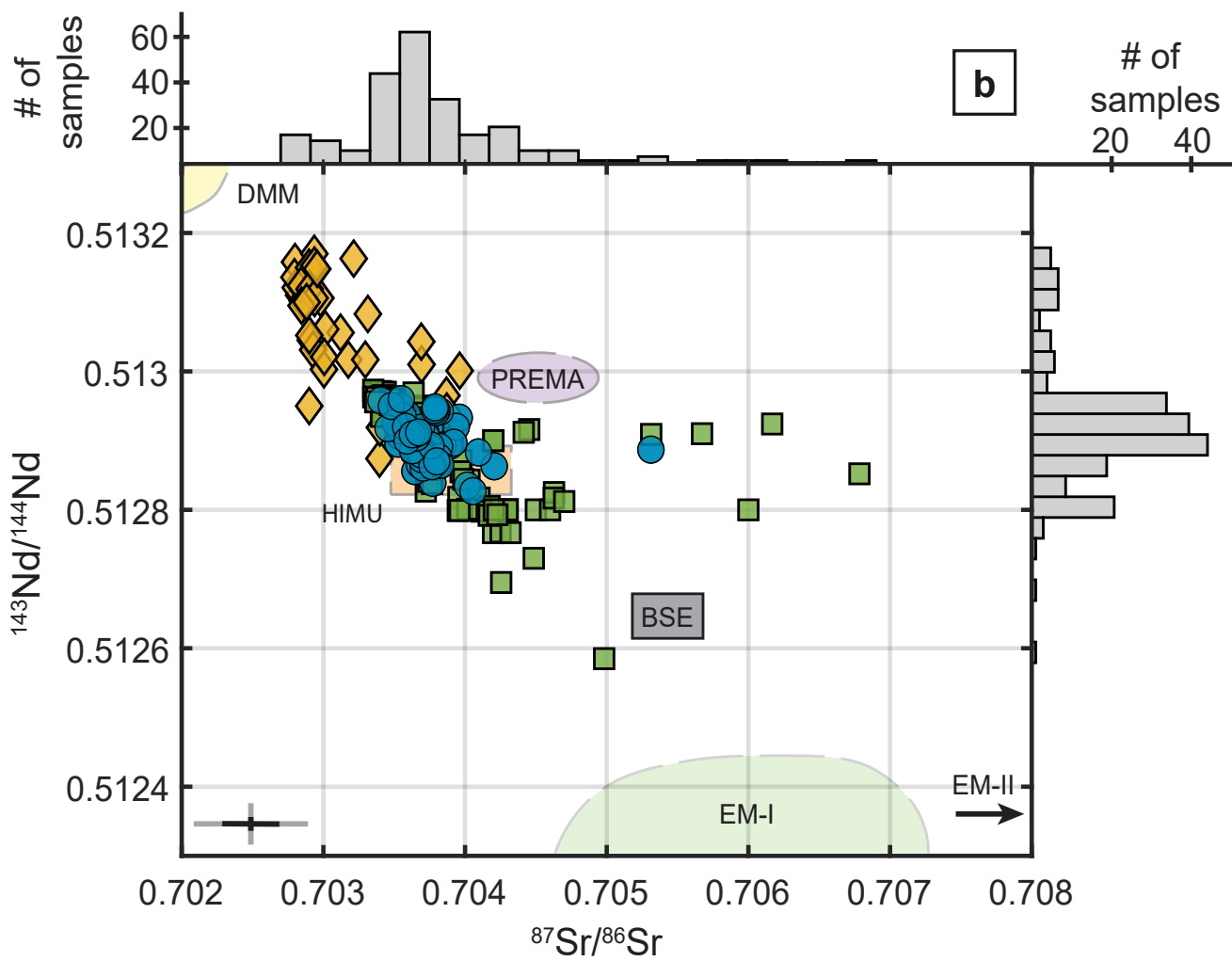
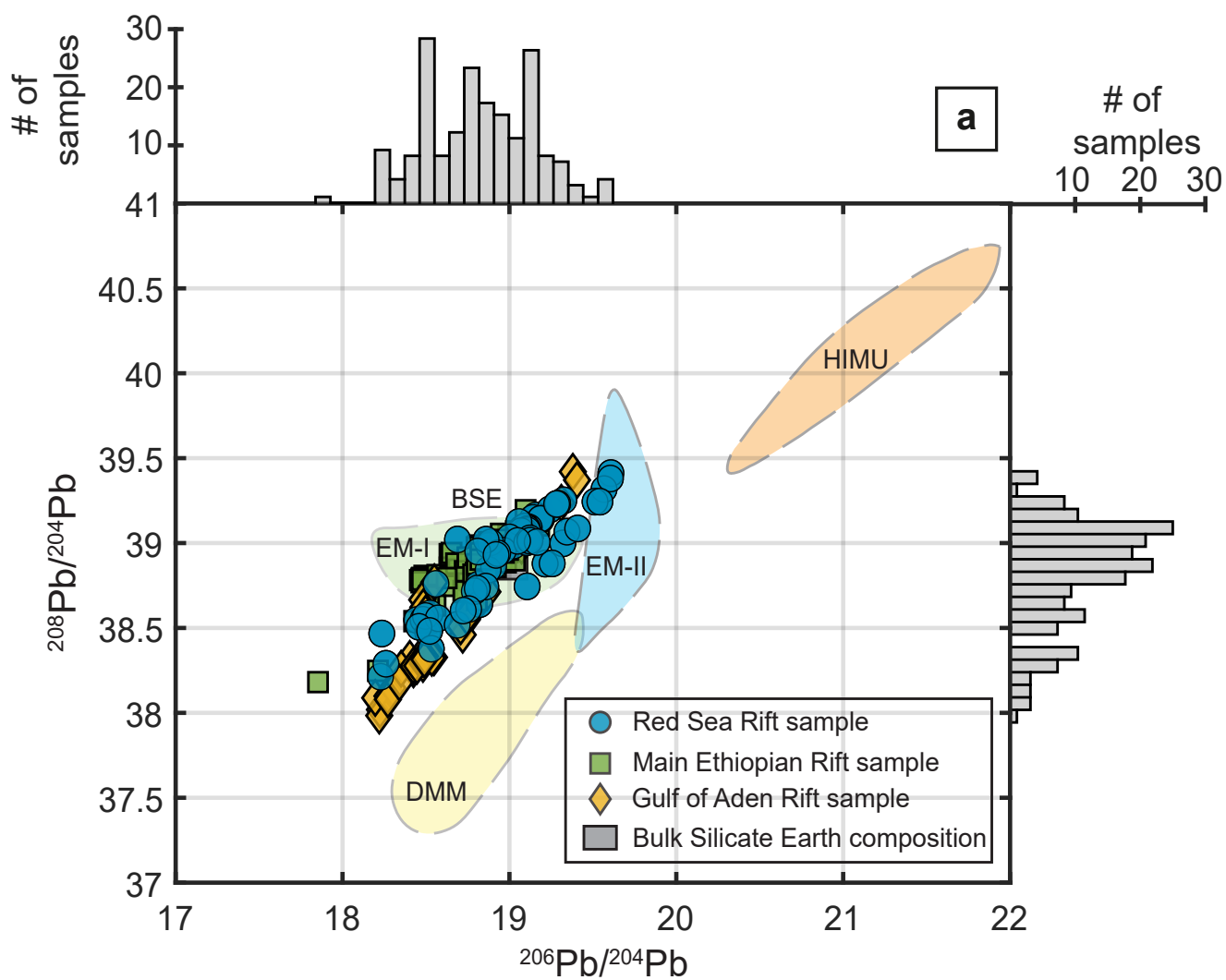
- 866 [67] Dugda, M. T., Nyblade, A. A., Julia, J., Langston, C. A., Ammon, C. J., & Simiyu, S.  
 867 (2005). Crustal structure in Ethiopia and Kenya from receiver function analysis: Implications  
 868 for rift development in eastern Africa. *Journal of Geophysical Research: Solid Earth*,  
 869 110(B1). <https://doi.org/10.1029/2004JB003065>
- 870 [68] Ogden, C. S., Bastow, I. D., Gilligan, A., & Rondenay, S. (2019). A reappraisal of the  
 871 H- $\kappa$  stacking technique: implications for global crustal structure. *Geophysical Journal*  
 872 *International*, 219(3), 1491-1513. <https://doi.org/10.1093/gji/ggz364>
- 873 [69] Stuart, G. W., Bastow, I. D., & Ebinger, C. J. (2006). Crustal structure of the northern  
 874 Main Ethiopian Rift from receiver function studies. *Geological Society, London, Special*  
 875 *Publications*, 259(1), 253-267. <https://doi.org/10.1144/GSL.SP.2006.259.01.20>
- 876 [70] Maguire, P. K. H., Keller, G. R., Klemperer, S. L., Mackenzie, G. D., Keranen, K.,  
 877 Harder, S., ... & Amha, M. (2006). Crustal structure of the northern Main Ethiopian Rift from  
 878 the EAGLE controlled-source survey; a snapshot of incipient lithospheric break-up.  
 879 *Geological Society, London, Special Publications*, 259(1), 269-292.  
 880 <https://doi.org/10.1144/GSL.SP.2006.259.01.21>
- 881 [71] Keranen, K. M., Klemperer, S. L., Julia, J., Lawrence, J. F., & Nyblade, A. A. (2009).  
 882 Low lower crustal velocity across Ethiopia: Is the Main Ethiopian Rift a narrow rift in a hot  
 883 craton?. *Geochemistry, Geophysics, Geosystems*, 10(5).  
 884 <https://doi.org/10.1029/2008GC002293>
- 885 [72] Eilers, P. H., & Marx, B. D. (1996). Flexible smoothing with B-splines and penalties.  
 886 *Statistical science*, 11(2), 89-121. <https://doi.org/10.1214/ss/1038425655>
- 887 [73] Eilers, P. H., & Marx, B. D. (2010). *Splines, knots, and penalties*. Wiley  
 888 *Interdisciplinary Reviews: Computational Statistics*, 2(6), 637-653.  
 889 <https://doi.org/10.1002/wics.125>

- 890 [74] De Boor, C., (1978). A practical guide to splines Vol. 27 Springer-verlag. New York.  
 891 <https://doi.org/10.1007/978-1-4612-6333-3>
- 892 [75] Jones, M., Randell, D., Ewans, K., & Jonathan, P. (2016). Statistics of extreme ocean  
 893 environments: Non-stationary inference for directionality and other covariate effects. Ocean  
 894 Engineering, 119, 30-46. <https://doi.org/10.1016/j.oceaneng.2016.04.010>
- 895 [76] Arthur, D., & Vassilvitskii, S. (2007). k-means++: The advantages of careful seeding. In  
 896 Soda (Vol. 7, pp. 1027-1035).<https://doi.org/10.5555/1283383>
- 897 [77] Stracke, A., Hofmann, A. W., & Hart, S. R. (2005). FOZO, HIMU, and the rest of the  
 898 mantle zoo. Geochemistry, Geophysics, Geosystems, 6(5).  
 899 <https://doi.org/10.1029/2004GC000824>
- 900 [78] McDonough, W. F., & Sun, S. S. (1995). The composition of the Earth. Chemical  
 901 Geology, 120(3-4), 223-253. [https://doi.org/10.1016/0009-2541\(94\)00140-4](https://doi.org/10.1016/0009-2541(94)00140-4)
- 902 [79] Zindler, A., & Hart, S. (1986). Chemical geodynamics. IN: Annual review of earth and  
 903 planetary sciences. Volume 14 (A87-13190 03-46). Palo Alto, CA, Annual Reviews, Inc.,  
 904 1986, p. 493-571., 14, 493-571. <https://doi.org/10.1146/annurev.ea.14.050186.002425>
- 905 [80] Rollinson, H. R., Rollinson, H., & Pease, V. (2021). Using geochemical data: to  
 906 understand geological processes. Cambridge University Press.  
 907 <https://doi.org/10.1017/9781108777834>
- 908 [81] Jochum, K. P., Willbold, M., Raczek, I., Stoll, B., & Herwig, K. (2005). Chemical  
 909 Characterisation of the USGS Reference Glasses GSA-1G, GSC-1G, GSD-1G, GSE-1G,  
 910 BCR-2G, BHVO-2G and BIR-1G Using EPMA, ID-TIMS, ID-ICP-MS and LA-ICP-MS.  
 911 Geostandards and Geoanalytical Research, 29(3), 285-302. [https://doi.org/10.1111/j.1751-](https://doi.org/10.1111/j.1751-908X.2005.tb00901.x)  
 912 [908X.2005.tb00901.x](https://doi.org/10.1111/j.1751-908X.2005.tb00901.x)

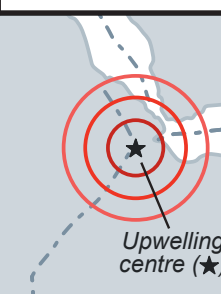
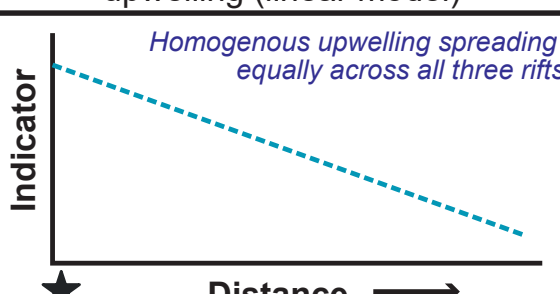
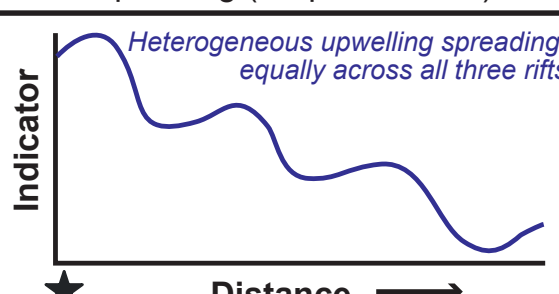
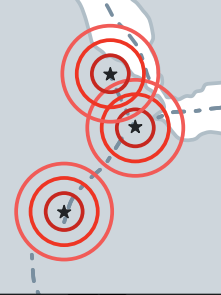
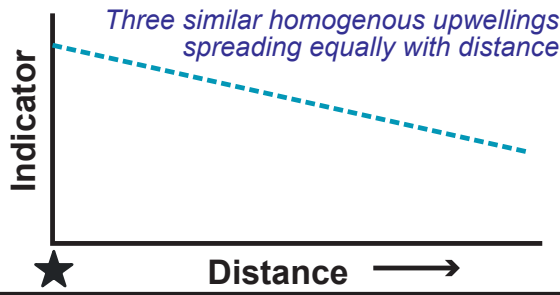
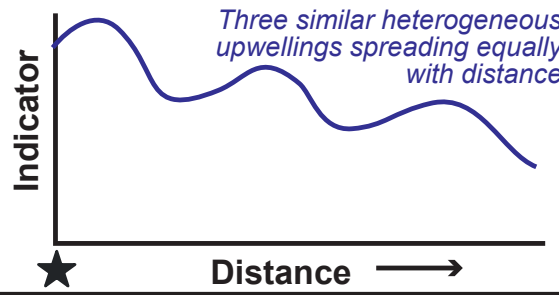
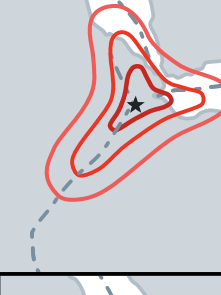
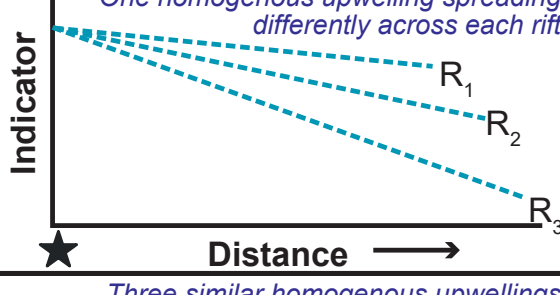
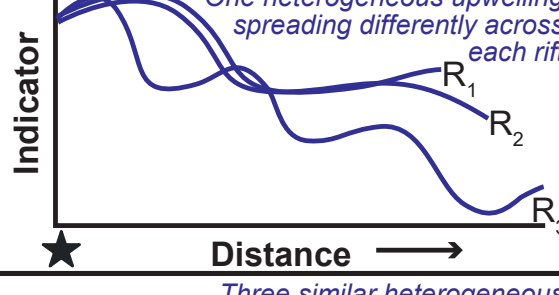

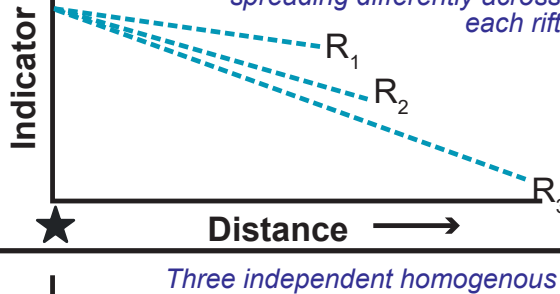
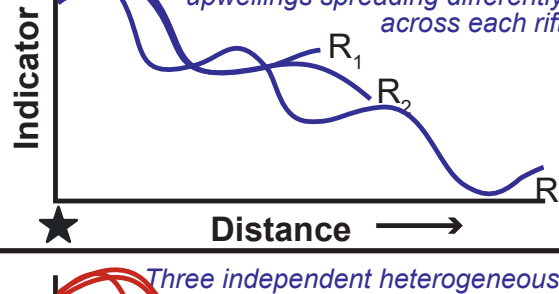
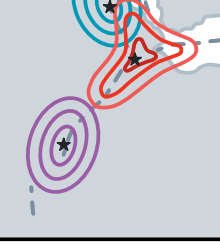
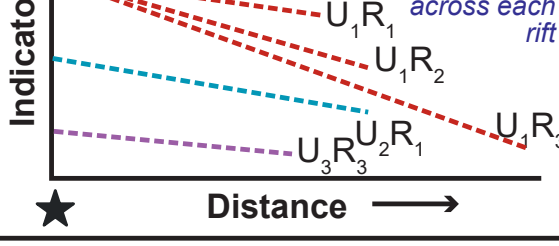
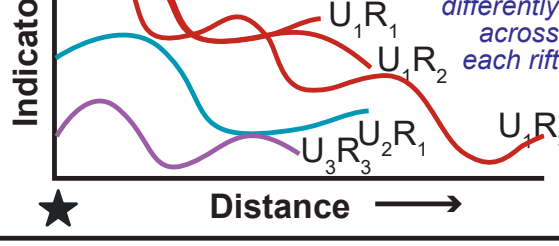
- 913 [82] Hart, S. R. (1988). Heterogeneous mantle domains: signatures, genesis and mixing  
 914 chronologies. *Earth and Planetary Science Letters*, 90(3), 273-296.  
 915 [https://doi.org/10.1016/0012-821X\(88\)90131-8](https://doi.org/10.1016/0012-821X(88)90131-8)
- 916 [83] Watts et al.. (2025). Dataset for Mantle upwelling at Afar triple junction shaped by  
 917 overriding plate dynamics. FigShare <https://doi.org/10.6084/m9.figshare.28769105>
- 918 [84] Watts et al.. (2025). MATLAB software for Mantle upwelling at Afar triple junction  
 919 shaped by overriding plate dynamics. GitHub <https://github.com/ygraigarw/AfarPlume.git>

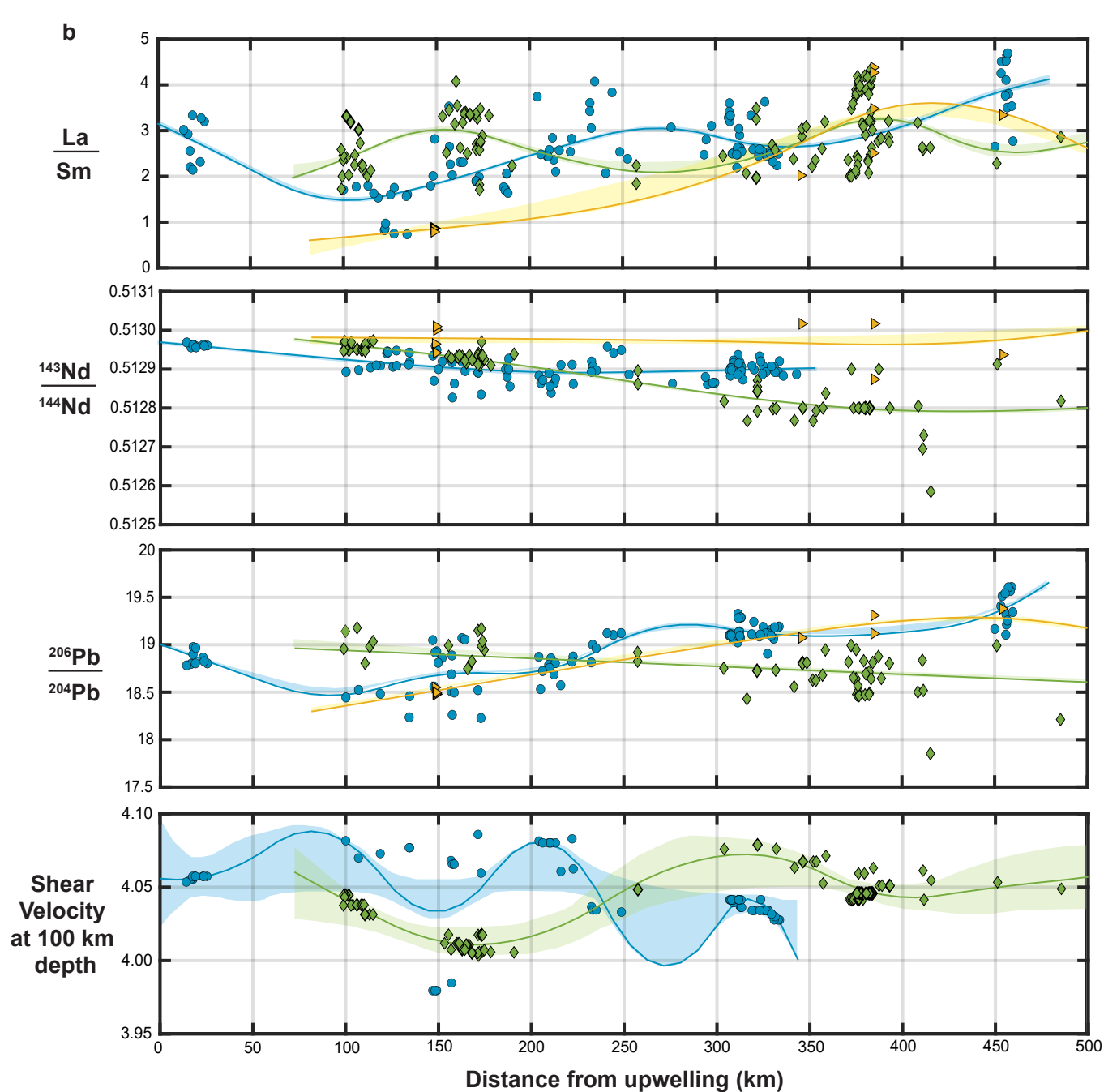
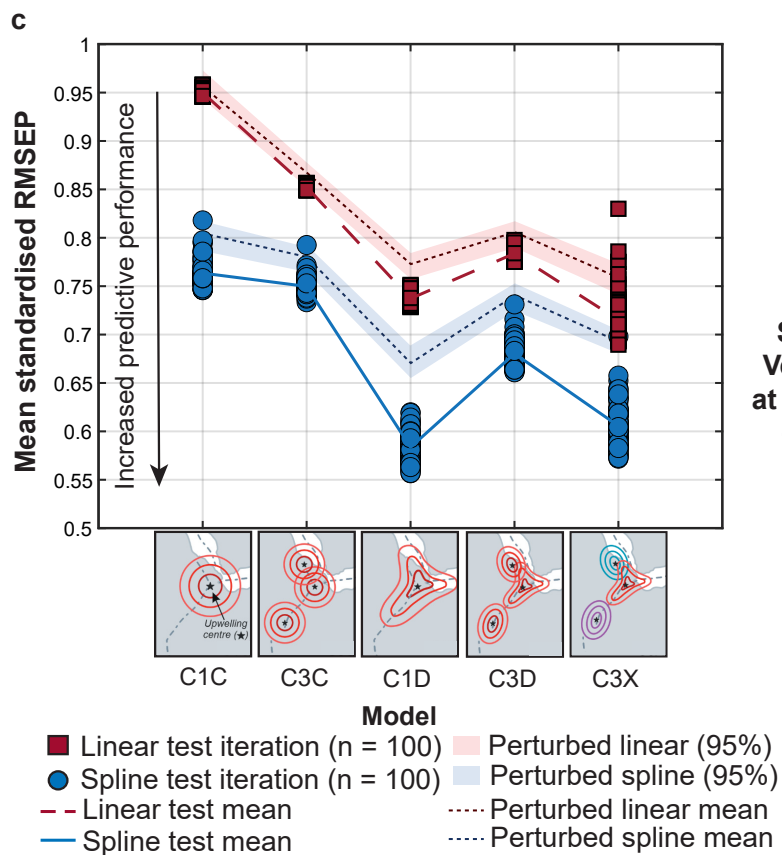
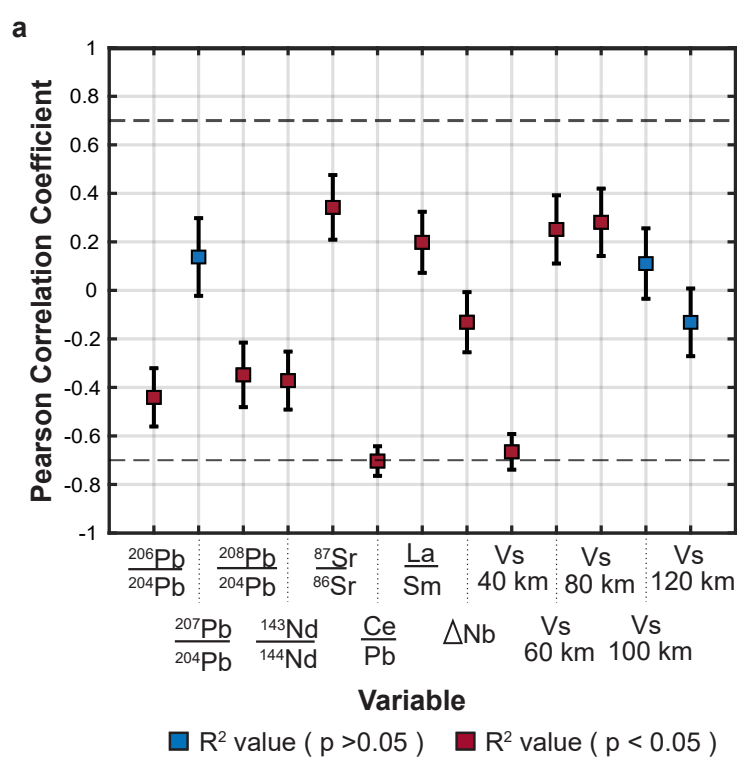


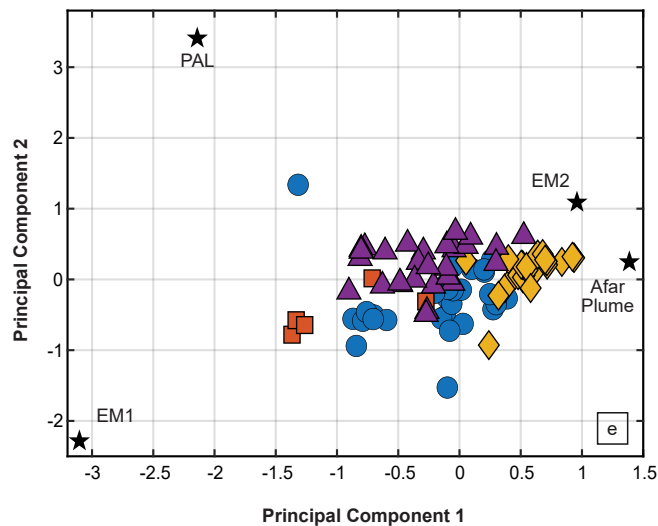
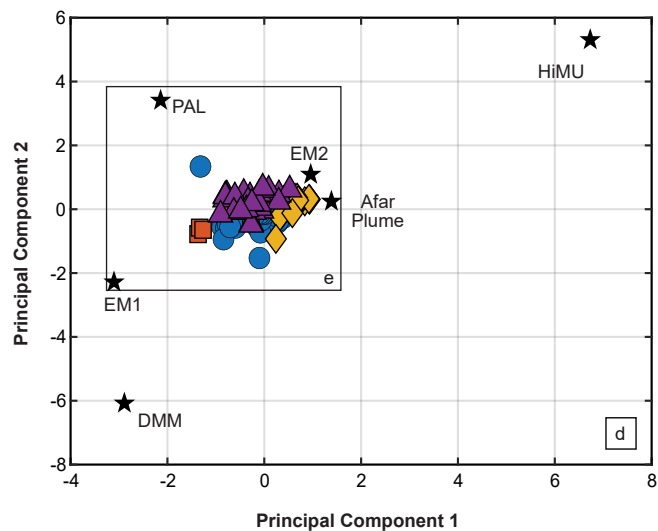
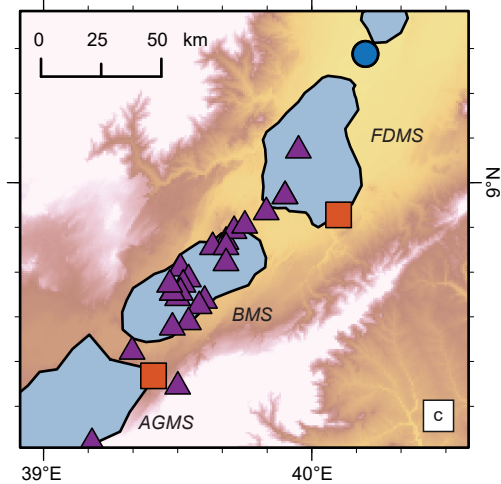
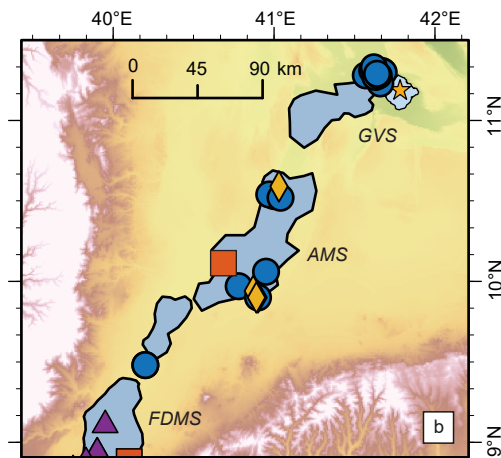
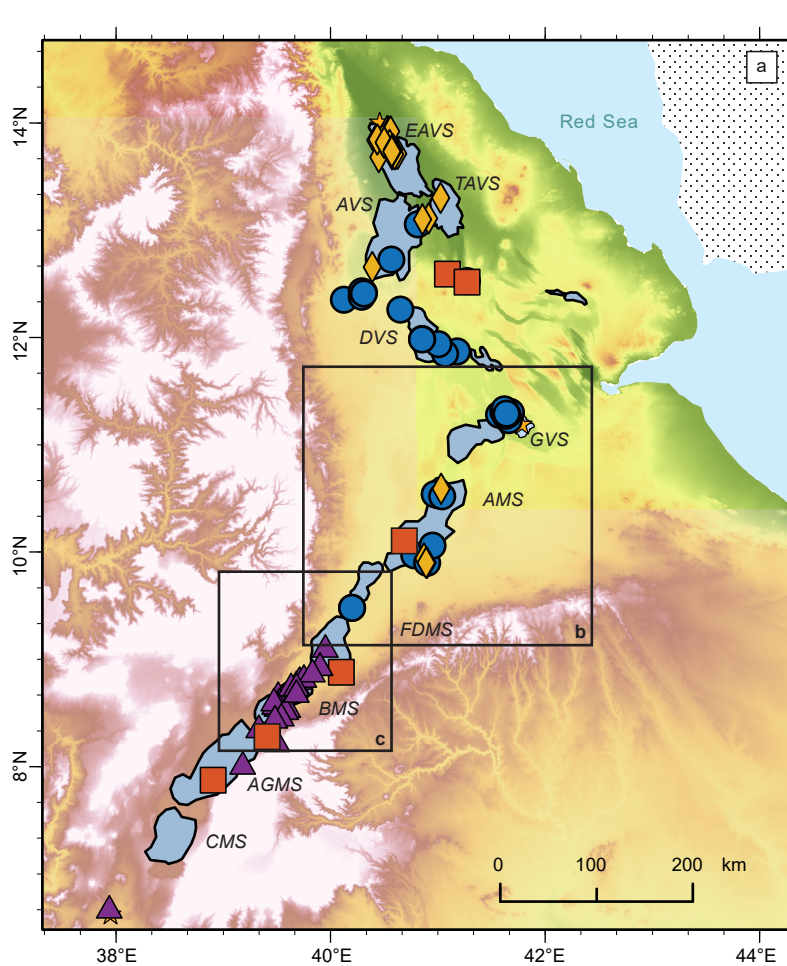




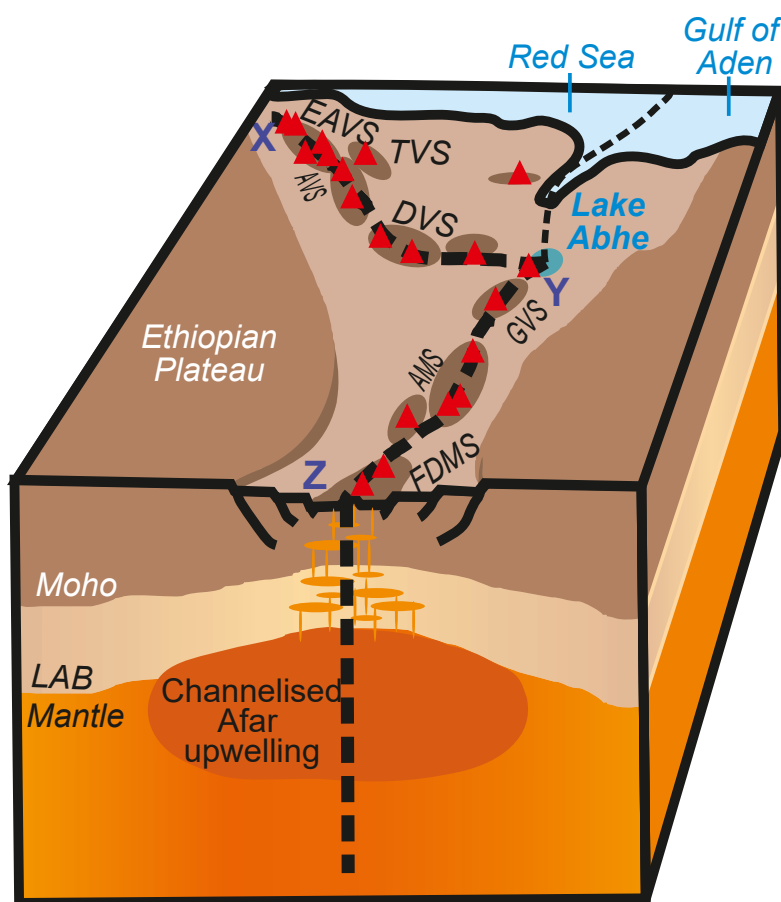


Model name & description	Model sketch	Expected plot for homogenous upwelling (linear model)	Expected plot for heterogeneous upwelling (B-spline model)
<b>C1C</b>  (1 upwelling centre, concentric spreading)			
<b>C3C</b>  (3 identical upwelling centres, concentric spreading)			
<b>C1D</b>  (1 upwelling centre, different spreading in each rift)			
<b>C3D</b>  (3 identical upwelling centres, different spreading in each rift)			
<b>C3X</b>  (3 different upwelling centres, different spreading in each rift)			



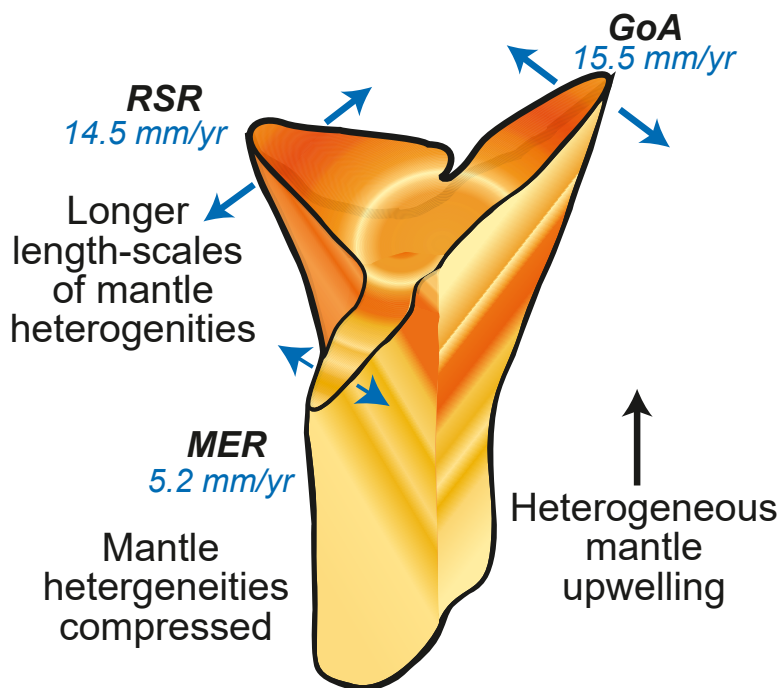


a

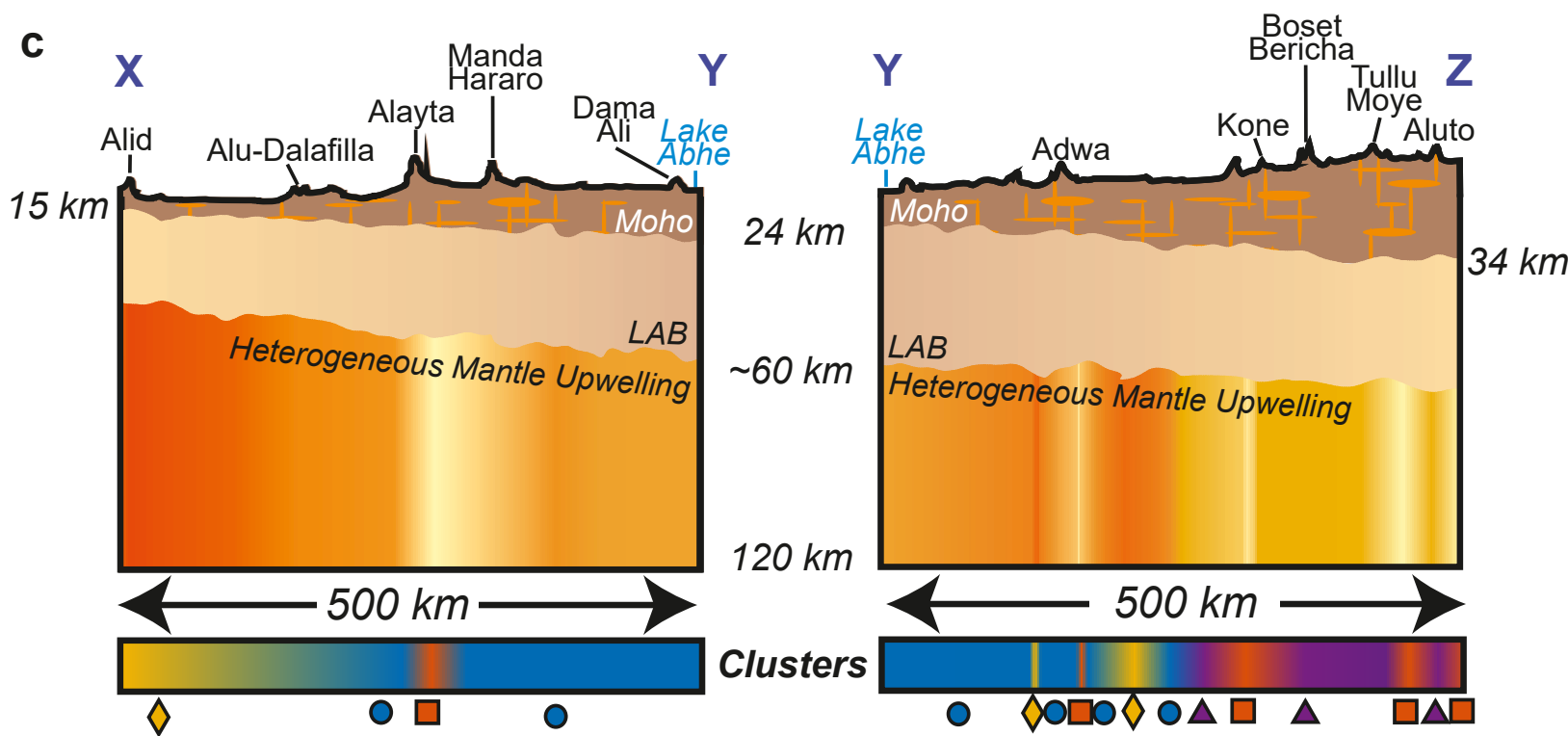


b

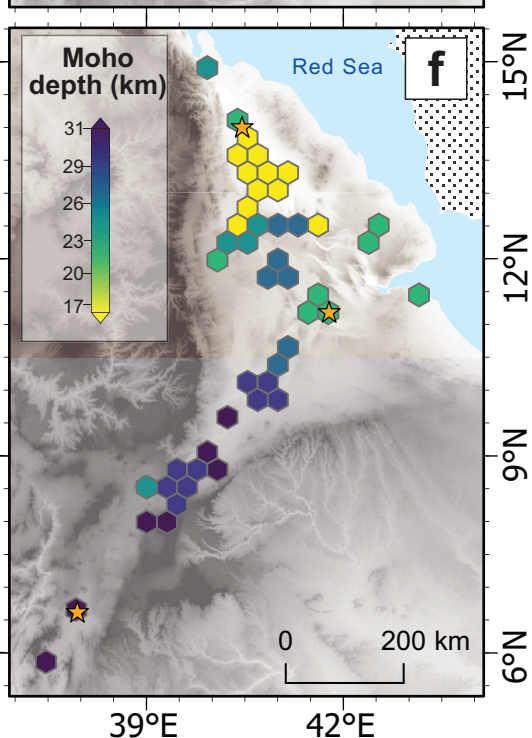
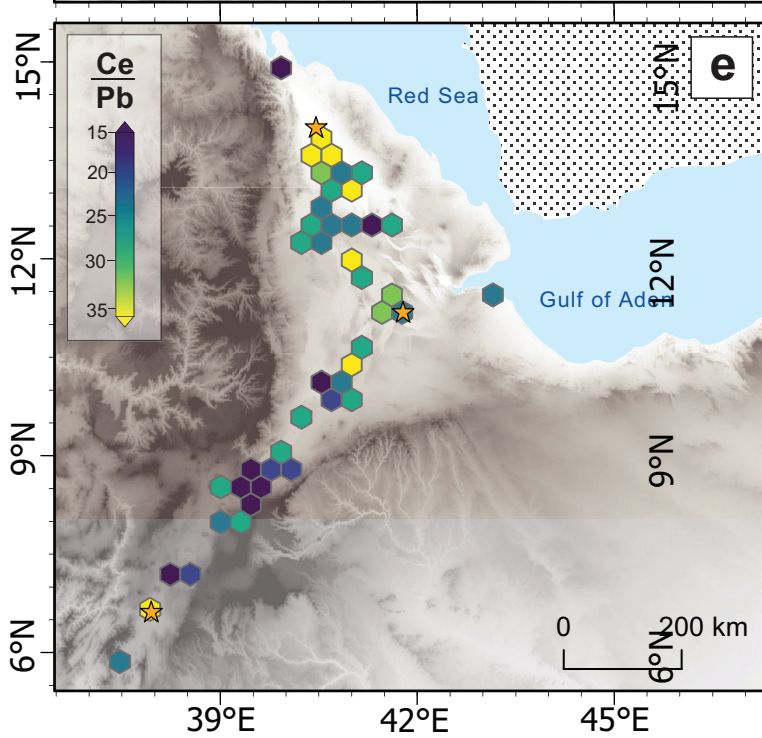
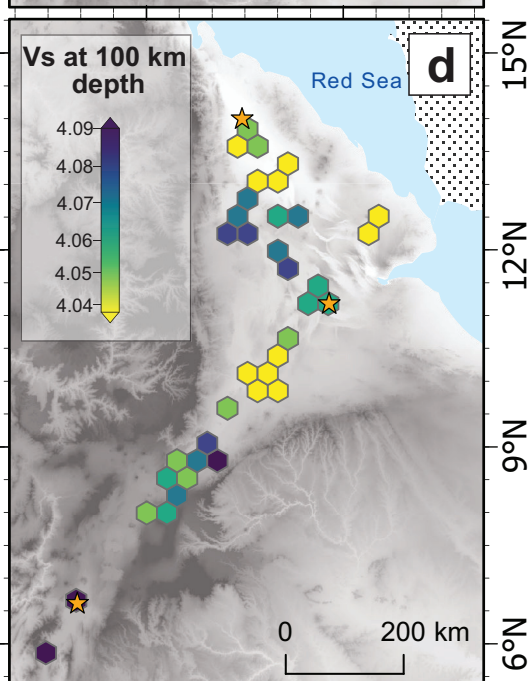
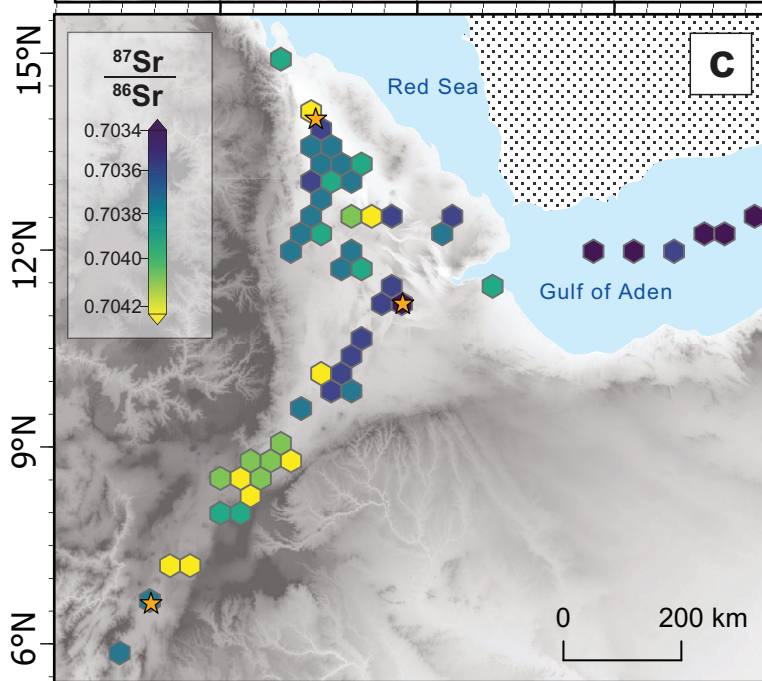
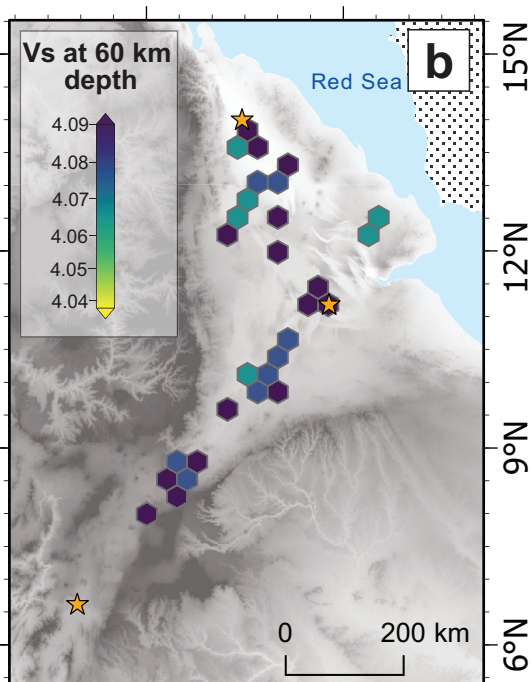
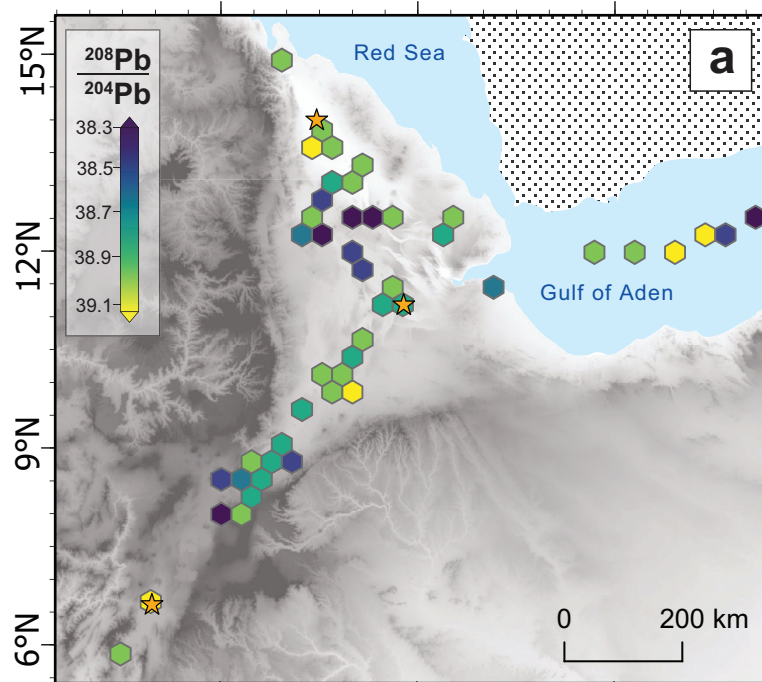
### Schematic of Afar upwelling

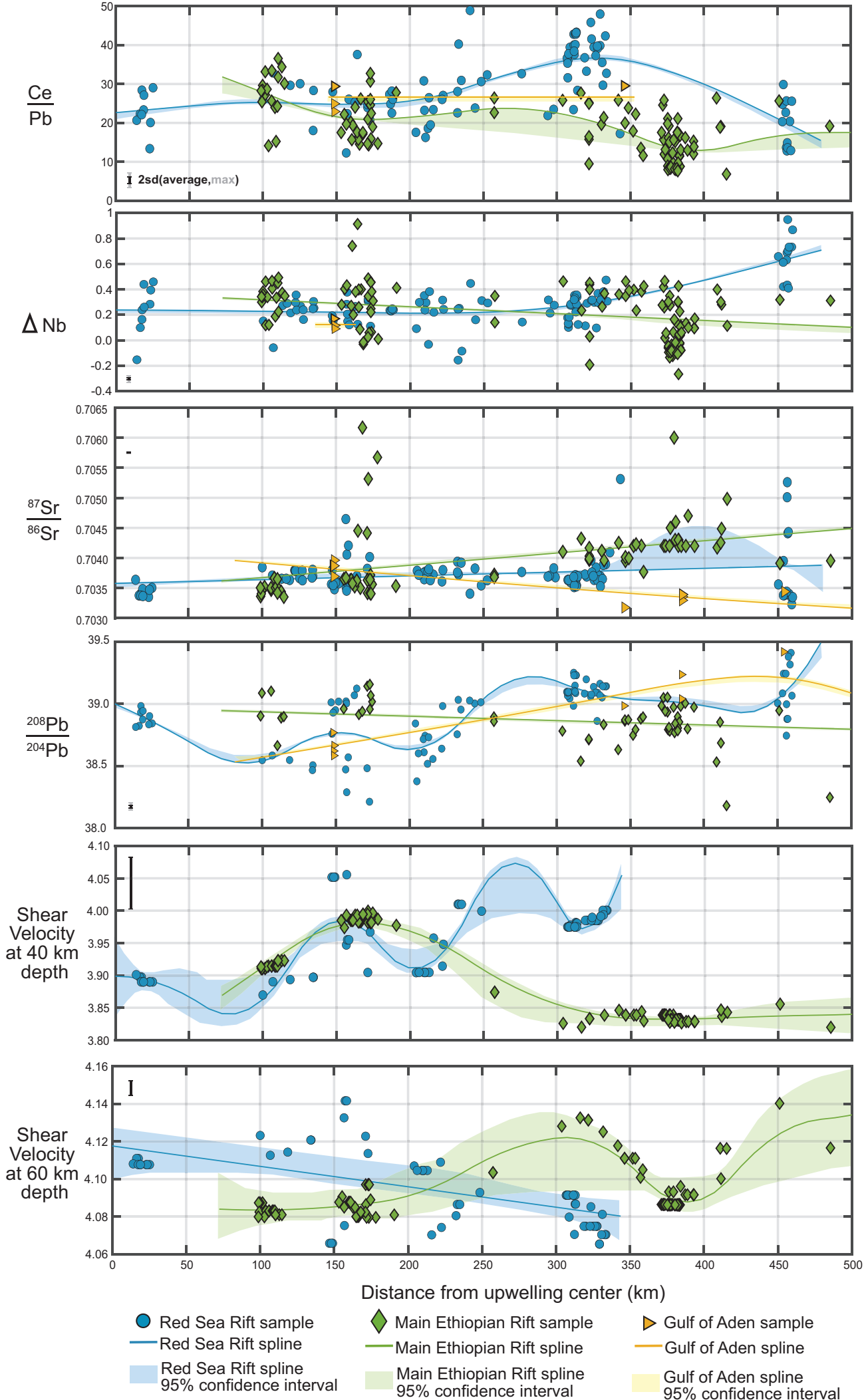


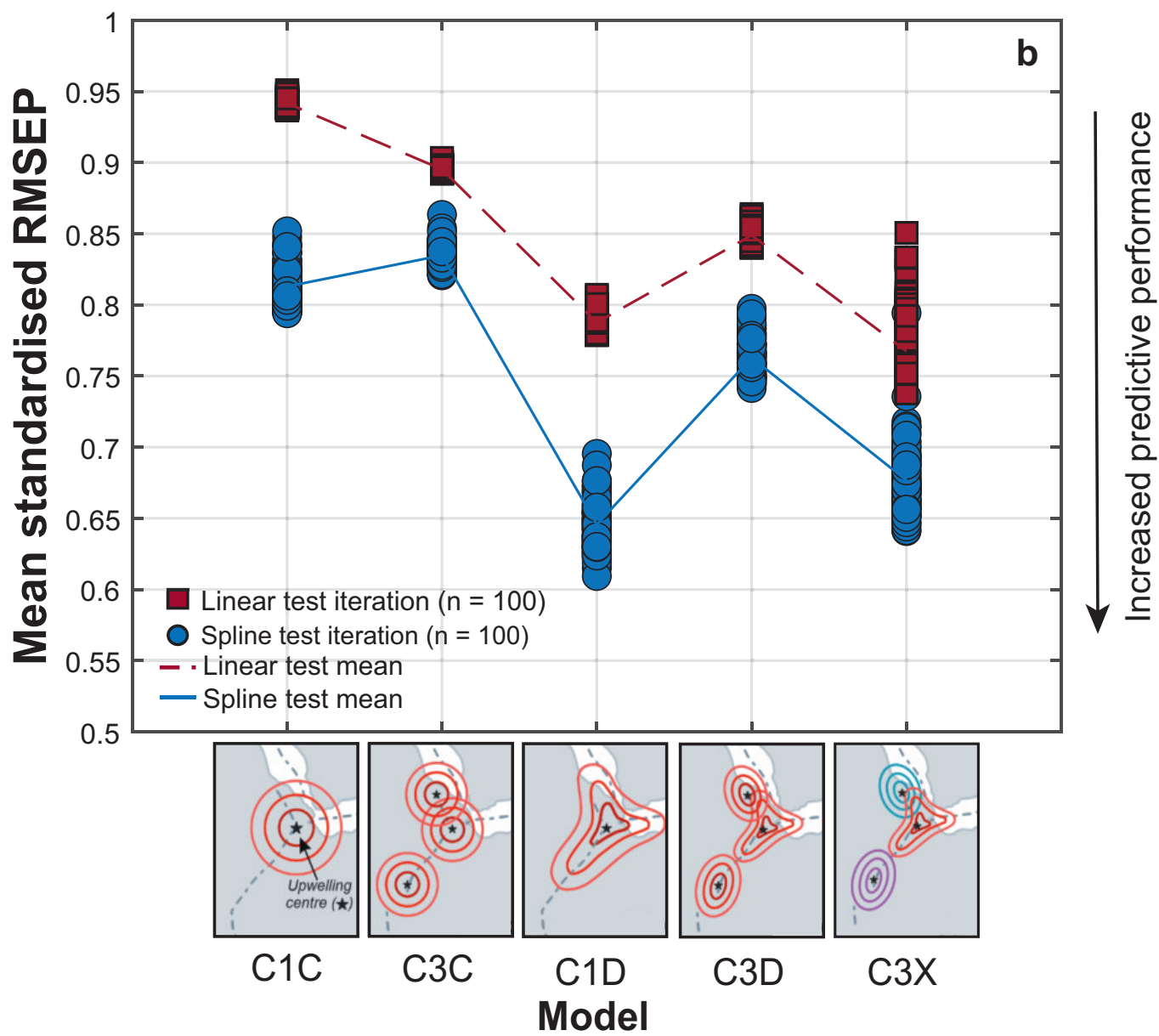
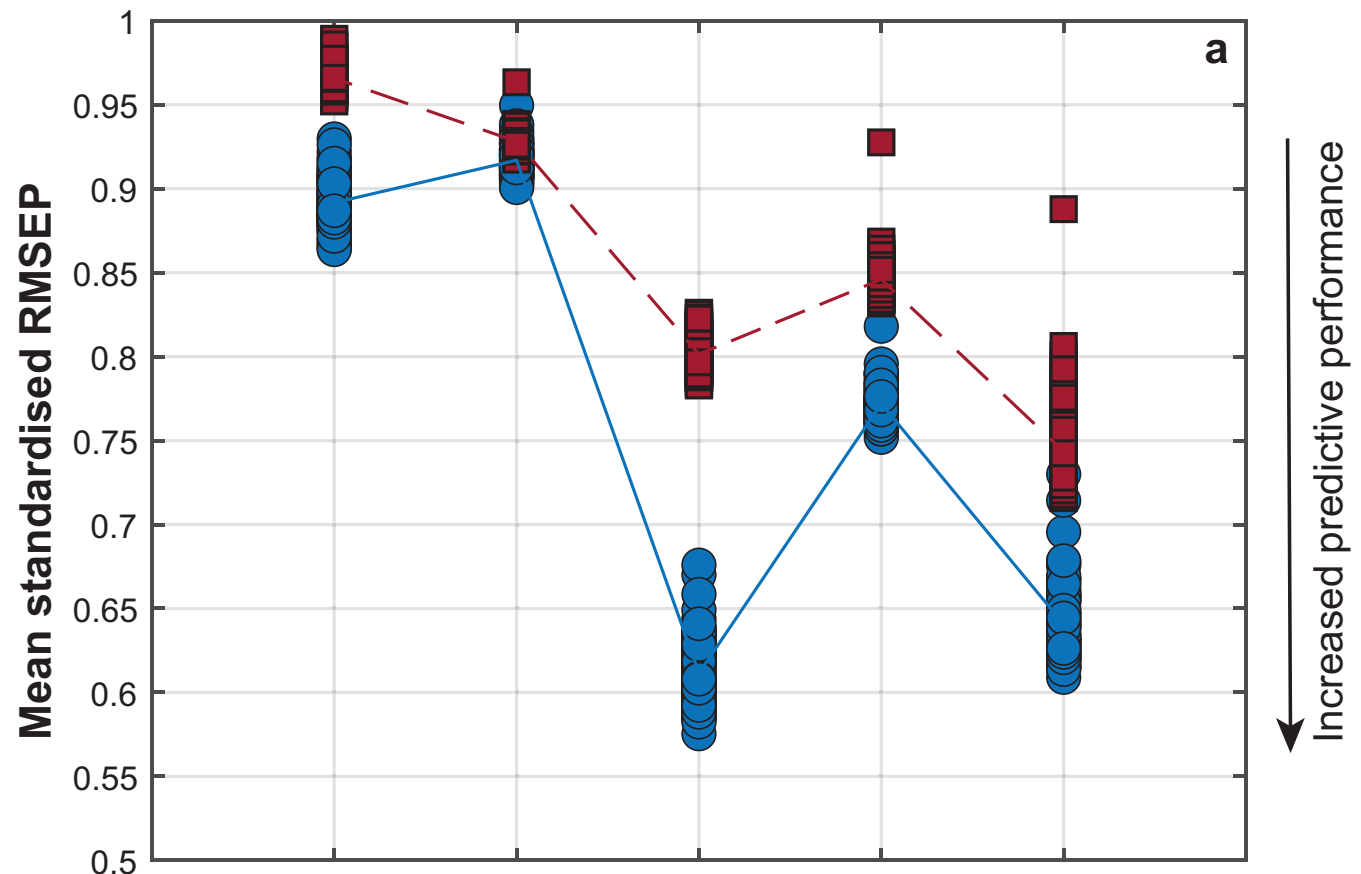
c













Variable (s)	Observed Range	Details
$^{206}\text{Pb}/^{204}\text{Pb}$	17.853 to 19.608	$^{206}\text{Pb}/^{204}\text{Pb} > 20$ is linked to HIMU, $^{206}\text{Pb}/^{204}\text{Pb}$ ranging from 19.2 to 20.5 indicates a mantle upwelling source (C, FOZO) [77] and $^{206}\text{Pb}/^{204}\text{Pb} < 17.8$ can be related to a depleted mantle component [78, 79].
$^{207}\text{Pb}/^{204}\text{Pb}$	15.448 to 15.697	$^{207}\text{Pb}/^{204}\text{Pb} < 15.5$ is related to a depleted mantle component [77], $^{207}\text{Pb}/^{204}\text{Pb} > 15.65$ is linked to the HiMU component and $^{207}\text{Pb}/^{204}\text{Pb} \sim 15.6$ indicates a mantle upwelling source (C, FOZO). A $^{207}\text{Pb}/^{204}\text{Pb} > 15.75$ is linked to crustal values [27, 41].
$^{208}\text{Pb}/^{204}\text{Pb}$	37.984 to 39.420	$^{208}\text{Pb}/^{204}\text{Pb} < 38$ is related to a depleted mantle component [77], $^{208}\text{Pb}/^{204}\text{Pb} > 39.5$ is linked to the HiMU component and $^{208}\text{Pb}/^{204}\text{Pb}$ 39.2 to 39.5 indicates a mantle upwelling source (C, FOZO). A $^{208}\text{Pb}/^{204}\text{Pb} > 39.7$ is linked to crustal values [27, 41].
$^{143}\text{Nd}/^{144}\text{Nd}$	0.51259 to 0.51317	A low $^{143}\text{Nd}/^{144}\text{Nd}$ ( $< 0.5121$ ) indicates continental crust or Pan African Lithosphere. $^{143}\text{Nd}/^{144}\text{Nd}$ values $\sim 0.51285$ indicates a HIMU or upwelling related mantle source. Higher $^{143}\text{Nd}/^{144}\text{Nd}$ values ( $> 0.5131$ ) indicate a depleted mantle source (i.e., DMM) [27, 78-80].
$^{87}\text{Sr}/^{86}\text{Sr}$	0.70279 to 0.70678	A low $^{87}\text{Sr}/^{86}\text{Sr}$ (0.7040-0.7045) indicates a mantle component that is either depleted (DMM) or a deeper mantle upwelling (HIMU, C). A higher $^{87}\text{Sr}/^{86}\text{Sr}$ ( $< 0.705$ ) indicates the potential influence from continental crust [27, 78-80].
Ce/Pb	6.84 to 48.92	A Ce/Pb $> 30$ is commonly attributed to a recycled mantle source that has been depleted in fluid mobile elements (i.e., Pb, Ba, Sr, K) during subduction, therefore resulting in high fluid-immobile-element to fluid-mobile-element ratios (i.e., Ce/Pb). Typical mantle has a Ce/Pb value of $25 \pm 5$ and crust a value of $\sim 4$ [38].
La/Sm	0.4 to 4.7	(La/Sm) $> 1$ indicates LREE enrichment fractionation (e.g., alkali basalts or upwelling), and (La/Sm) $< 1$ indicates LREE depleted (mid-ocean ridge). In general, the higher the La/Sm the lower the melt fraction [23]
$\Delta\text{Nb}$	-0.26 to 0.95	Differentiates between a depleted mantle ( $\Delta\text{Nb} < 0$ ) and a mantle upwelling ( $\Delta\text{Nb} > 0$ ) [6]. $\Delta\text{Nb} = 1.74 + \log \frac{N_b}{Z_r} - 1.92 \log \frac{Z_r}{N_b}$
Vs @ 40 km	3.81 to 4.06	Shear wave velocities can be sensitive to temperature, grainsize and the presence of fluids. A reduction in Vs can indicate a change in mantle composition or an increased proportion of melt to hydrothermal fluid [31]. Here, we used the velocities from 40 km to 120 km depth.
Vs @ 60 km	4.06 to 4.18	
Vs @ 80 km	4.00 to 4.16	
Vs @ 100 km	3.97 to 4.10	
Vs @ 120 km	4.03 to 4.10	
Moho depth	16-30 km	Depth to the Mohorovičić Discontinuity.



Model Name	Summary	Description
C1C	1 upwelling centre, concentric spreading	A singular upwelling centred at Lake Abhe (11.192 °N, 41.784 °E) with each rift (i.e., Red Sea Rift, Gulf of Aden rift and Main Ethiopian Rift) behaving the same (not independently), based on the theory of ref.[23]. This model fits a single line using all the data points from each rift. A linear model is used when assuming the upwelling is homogenous, and a spline is used to allow for heterogeneities in the upwelling.
C3C	3 identical upwelling centres, concentric spreading	Three upwellings centred at Lake Abhe (11.192 °N, 41.784 °E), and two other points across the region (14.008 °N, 40.458 °E and 6.626 °N, 37.948 °E); this model is based on the locations of previously proposed small-scale upwelling locations through numerical modelling [34]. Assumes each rift behaves the same (not independent of each other) and the upwellings are of the same composition.
C1D	1 upwelling centre, different spreading in each rift.	A singular upwelling centred at Lake Abhe (11.192 °N, 41.784 °E) with each rift behaving independently. This model fits three lines (i.e., one for each rift) across all data points for the corresponding rift.
C3D	3 identical upwelling centres, different spreading in each rift.	Three small-scale upwellings centred at Lake Abhe (11.192 °N, 41.784 °E), and two other points across the region (14.008 °N, 40.458 °E and 6.626 °N, 37.948 °E) with each rift acting independently. This model assumes that each upwelling is compositionally the same and fits three lines (i.e., one for each rift) across all data points for the corresponding rift.
C3X	3 different upwelling centres, different spreading in each rift.	Three small-scale upwellings centred at Lake Abhe (11.192 °N, 41.784 °E), and two other points across the region (14.008 °N, 40.458 °E and 6.626 °N, 37.948 °E) with each rift and upwelling acting independently. This model plots five lines.

End Member	Afar Plume	Depleted Mantle	Pan African Lithosphere	HiMU	EMI	EMII
$^{206}\text{Pb}/^{204}\text{Pb}$	19.5	17.5	17.85	22	17.4	19.3
$^{207}\text{Pb}/^{204}\text{Pb}$	15.6	15.3	15.75	15.84	15.48	15.64
$^{208}\text{Pb}/^{204}\text{Pb}$	39.2	36.6	39.75	40.75	39.0	39.75
$^{87}\text{Sr}/^{86}\text{Sr}$	0.512875	0.51335	0.5121	0.51285	0.51235	0.51235
$^{143}\text{Nd}/^{144}\text{Nd}$	0.7035	0.7022	0.7075	0.7025	0.7055	0.709
References	[41, 51]	[41, 51]	[41, 51]	[82]	[82]	[82]